InAsSb barrier heterostructures for infrared optoelectronics

A Dissertation Presented

by

Jinghe Liu

to

The Graduate School

in Partial Fulfillment of the

Requirements

for the Degree of

Doctor of Philosophy

in

Electrical Engineering

Stony Brook University

August 2021

Stony Brook University

The Graduate School

Jinghe Liu

We, the dissertation committee for the above candidate for the

Doctor of Philosophy degree, hereby recommend

acceptance of this dissertation.

Dmitri Donetski – Dissertation Advisor
Associate Professor, Department of Electrical & Computer Engineering

Ridha Kamoua - Chairperson of Defense
Associate Professor, Department of Electrical & Computer Engineering

Leon Shterengas
Professor, Department of Electrical & Computer Engineering

Sergey Suchalkin
Assistant Professor, Department of Electrical & Computer Engineering

David Hwang
Associate Professor, Department of Mechanical Engineering

This dissertation is accepted by the Graduate School

Eric Wertheimer

Dean of the Graduate School

Abstract of the Dissertation

InAsSb barrier heterostructures for infrared optoelectronics

by

Jinghe Liu

Doctor of Philosophy

in

Electrical Engineering

Stony Brook University

2021

InAsSb is a promising material for mid-wave to long-wave infrared optoelectronics. It has the lowest energy band gap among all III-V compounds. Development of Ga(Al)InSb/InAsSb/AlInGaAsSb barrier heterostructure has been studied for more than 10 years. This barrier heterostructure can effectively separate electrons and holes for unipolar carrier transport. Separation of two narrow bandgap regions by the wide bandgap barrier can reduce the generation-recombination current in the absorber, resulting in an Auger-limited dark current with the prospect of high temperature operation. Recent progress in this dissertation addresses the achievement of operation at the wavelength of 10 μm in barrier structures using strained layer superlattices (SLS), as well as the operation at 5-10 μm using bulk $InAs_{1-x}Sb_x$ with Sb composition in the range of 9% to 40%. The InAsSb barrier heterostructures have been demonstrated in photodetectors, beam steering devices and arrays with integrated multiplexing.

In the design of barrier heterostructure for long-wave infrared detection, the type-II strained layer superlattices and bulk InAsSb as absorbers were proposed. Both have the energy

band gap of λ = 10 μm. For SLS absorbers, a 4.3-nm short-period $InAsSb_{0.3}/InAsSb_{0.55}$ and a 10.9-nm long-period $InAs/InAsSb_{0.36}$ were modeled by 8-band $k \cdot p$ method. The quantum efficiency (QE), minority hole lifetime and vertical hole mobility were studied in the long-wave infrared nBn photodetector. The short-period SLS structure (SP) grown metamorphically demonstrated at least 2 times greater vertical hole mobility than that in long-period structure (LP) grown pseudomorphically at the temperature range of 77-150 K. The metamorphic growth was achieved by introducing linear graded buffer on top of GaSb substrate enabled greater average Sb composition and less strain in SLS thin layers compared to that grown pseudomorphically. Moreover, the minority hole lifetime of 555 ns was measured in SP structure at 77 K, which is a factor 2.5 times greater than the best minority hole lifetime reported previously for InAsSb grown on metamorphic buffers. Both greater vertical hole mobilities and longer lifetimes resulted in a 1.5 times greater quantum efficiency (QE) in SP structure at 77 K, increasing from 40 % to 63 %. Impact of valence band alignment and barrier doping on device performance were explored in bulk $InAs_{0.6}Sb_{0.4}$ absorbers by varying the barrier composition, absorber doping concentration and contact doping concentration. We summarized all the historically available data of InAsSb nBn photodetectors in our group. Then their performance was compared with that of state-of-the-art HgCdTe photodetectors under Rule07. Simulation results also indicated a new recommended valence band bowing parameter of 0.4 eV in InAsSb based on the energy band gap bowing of 0.87 eV.

Free-space beam intensity modulation was realized in the nBp heterostructure with the modulation depth of 8-9 % based on single-pass transmission. The idea was demonstrated with a $InAsSb_{0.42}$ and a Type-2 SLS $InAsSb_{0.35}/InAsSb_{0.65}$ active region in the barrier heterostructures. The data of modulation depths were in good agreement with the transmittance modeling results

in both cases. The estimated quasi Fermi level rise was 20 meV and the electrically injected excess carrier concentration above Ec was (1-2) $x10^{16}$ cm^{-3} according to the measured modulation of transmission spectra. The dependences of the excess carrier concentration on injected current were used in the fitting of the temperature-dependent Auger coefficients for the recombination process involving two electrons and heavy hole with energy transfer to another electron (CHCC). Significant refractive index changes of 0.05-0.06 were derived by manipulating the fundamental absorption edge based on Kramers-Kronig relations. This number is orders of magnitude greater than the change of refractive index which can be realized in high electric field in conventional EO materials. An insight on the application of beam steering device was discussed, including optical phased arrays and grating couplers. A vertical steering angle of 4.5° by modulation of the refractive index at the outcoupled angle of 45° was demonstrated in the grating coupler by simulation.

The arrays of optical modulators for laser beam intensity modulation with high spatial resolution (beam shaping) have been proposed. To mitigate the large number of contacts in the addressable array of optical modulators, an integrated double barrier heterostructure for current multiplexing was proposed using $InAs_{0.91}Sb_{0.09}$ with a lattice matched growth on GaSb substrate. The double barrier heterostructure incorporated the control gate layer capable to control the injection current in a pixel of the selected row and column of the 2D array of the modulators with high current gain and high on/off current ratio. The current gain of 2,580, the control current of 10^{-6} A and the on/off current ratio of 5,600 were simultaneously achieved at T = 200 K. The active region current density of $J_a = 1.66x10^3$ A/cm^2 was demonstrated. The modeling showed that of the double barrier heterostructure is capable of current addressing in the arrays with 1,000x1,000 pixels.

A R&D project is underway at Brookhaven National Laboratory and Stony Brook University to demonstrate the first soft X-ray beam position monitor (SXBPM) based on GaAs photodiode array technology. The SXBPMs should provide micron-scale positional resolution, operate in ultrahigh vacuum and place in the beam halo to preserve beam coherence. Photodiode arrays with a shallow pn junction have been designed and extensively simulated. The first detector array prototypes with up to 64 pixels have been fabricated and characterized with Ar-ion laser. Eight arrays have been packaged in ceramic and shipped to BNL to be tested in soft X-ray beam at CSX end-station. Due to the geometrical constraints from the upstream of the SXBPM location, the detectors installed on the movable arms must be placed inside the FOE fixed mask but outside the slit aperture. Beside the traditional difference-over-sum method, new algorithms for beam position calculation are under development to take full advantage of extended multi-pixel arrays.

Table of Contents

List of Figures

Chapter 1

Chapter 2

Chapter 3

Chapter 4

Chapter 5

Appendix I

Appendix III

List of Tables

Chapter 2

Chapter 3

Chapter 4

Chapter 5

Acknowledgments

I want to show my gratitude to people who have guided me and helped me during the PhD study.

First, I want to show my deep appreciation to my advisor Prof. Dmitri Donetski, for his constant encouragement and guidance in these 6 years. Thank you for instructing me with patience in the projects and share your wisdom in research and in life. It is my great pleasure to study with you.

Next, I would like to show appreciation to those have supervised and instructed me in the project, Prof. Anatoly Frenkel and Dr. Boris Podobedov. Thank Prof. Frenkel for praising my research work for the first time in my PhD early stage and raising my courage to continue the career path. Thank Dr. Podobedov for instructing me and leading me to a new research field, as well as encouraging me by saying “You can do better than that!”.

I also want to show my profound gratitude to all the professors and team members of Optoelectronics Group, Prof. Gregory Belenky, Prof. Leon Shterengas, Prof. Sergey Suchalkin, Dr. Gela Kipshidze, as well as former members Dr. Takashi Hosoda, and Dr. Jiang Jiang.

Last but not least, to my loving, supportive parents and my boyfriend Lingjie Zhang: Your priceless mental support and accompany in everyday life encourage me to pass through this important period in my entire life.

Publications

1. **J. Liu**, K. Kucharczyk, R. Lutchman et al. GaAs detector array for soft X-ray beam position monitoring in storage ring light sources, CLEO2021: AM4Q.2

2. **J. Liu**, K. Kucharczyk, D. Donetsky et al. Infrared beam steering device based on InAsSb/(Al)GaInSb heterostructure, CLEO2021: JTu3A.51

3. **J. Liu**, K. Kucharczyk, R. Lutchman et al. Progress towards Soft X-ray Beam Position Monitor development, Proc in IPAC'21: MOPAB121

4. C. Eng, D. Donetsky, S. Hulbert, **J. Liu** et al. Mechanical design of a soft X-ray beam position monitor for the coherent soft X-ray scattering beamline, accepted by MEDSI 2020

5. **J. Liu**, D. Donetsky, H. Jiang, et al. Electrical modulation of the LWIR absorption and refractive index in InAsSb-based strained layer superlattice heterostructures. J. Appl. Phys., 2020, 128(8): 083101.

6. D. Donetsky, **J. Liu**, G. et al. InAsSb-based heterostructures for infrared light modulation, Appl. Phys. Lett, 2019, 115(8): 081102

7. S. Svensson, W. Sarney, W. Beck, **J. Liu**, et al. P-doping with Beryllium of long-wavelength InAsSb, Semicond. Sci. Technol., 35(12), 125001.

8. W. Sarney, S. Svesson, A. Leff, D. Donetsky, **J. Liu**, et al. Influence of strain on the InAs1–xSbx composition. JVST B, Nanotechnology and Microelectronics: Materials, Processing, Measurement, and Phenomena, 2020, 38(3): 032206.

9. H. Singh, D. Donetsky, **J. Liu**, et al. Investigation of periodically driven systems by x-ray absorption spectroscopy using asynchronous data collection mode. Rev. Sci. Instrum., 2018, 89(4): 04511

10. *(pending)* **J. Liu**, D. Donetsky, Z. Zhang, et al. Impact of valence band offset and doping on barrier photodetectors in high-temperature operation, in submitting to J. Eletron. Mater.

11. *(pending)* **J. Liu**, D. Donetsky, K. Kucharczyk et al. Short-period InAsSb-based Strained Layer Superlattices with high vertical hole mobility and high quantum efficiency for long-wave infrared detection, in submitting to Appl. Phys. Lett.

Chapter 1 Background: a comparison of existing III-V and II-VI semiconductor compound absorbers for LWIR detectors

1.1 Overview of barrier heterostructures

The barrier heterostructure was first proposed by Anthony White in 1983 as a high impedance photoconductor [1]. The barrier is blocking the transport of majority carriers (e.g. electrons) and does not impede the transport of minority carriers (e.g. holes). It can be considered as a photoresistor with unipolar type of conductivity. The separation of excess carriers occurs with the help of the barrier. Therefore, the energy barrier created by the depletion region of pn junction diode is not needed. By using the barrier, one can realize the excess carrier separation without doping. The barrier heterostructure was patented and a detailed classification of various type of barrier heterostructures operating as a depletion-less photodiode was made by Philip Klipstein in 2003 [2]. The nBn device was first demonstrated experimentally using InAs n-layers and AlAsSb barrier by Maimon and Wicks in 2006 [3], where it worked as a unipolar photodetector with 5.2 μm cutoff wavelength. In InAs diodes, the surface inversion layer creates a shunt to the high impedance of the bulk part of pn junction and hence, high dark current due to surface current. The surface current was due to thermal generation of carriers in the depletion region. The barrier created a break in the surface layer and resulted in blocking thermal generation current path and a reduction of the G-R component of dark current dominating at low temperatures by orders of magnitudes. Klipstein also stated such structure as “XBn”/”XBp” or “CBn”/”CBp” if different materials are applied to each narrow bandgap region [4].

The barrier heterostructure is composed of two narrow bandgap layers and one barrier sandwiched in between. One of the narrow bandgap layers functions as the photon absorbing

layer, and its thickness should be corresponding to the dispersive absorption depth. The other narrow bandgap layer is used as the contact layer for collecting electrons or holes by carrier recombination.

The energy band gap in the absorbing layer should be corresponding to the operating wavelength of the detector. For the operation at mid-wave to long-wave infrared, InAsSb bulk [5–7] and InAs/GaSb type-II superalttices [8–11], and InAsSb-based type-II superlattices [12–16] are commonly suggested as the absorbing layer and the contact.

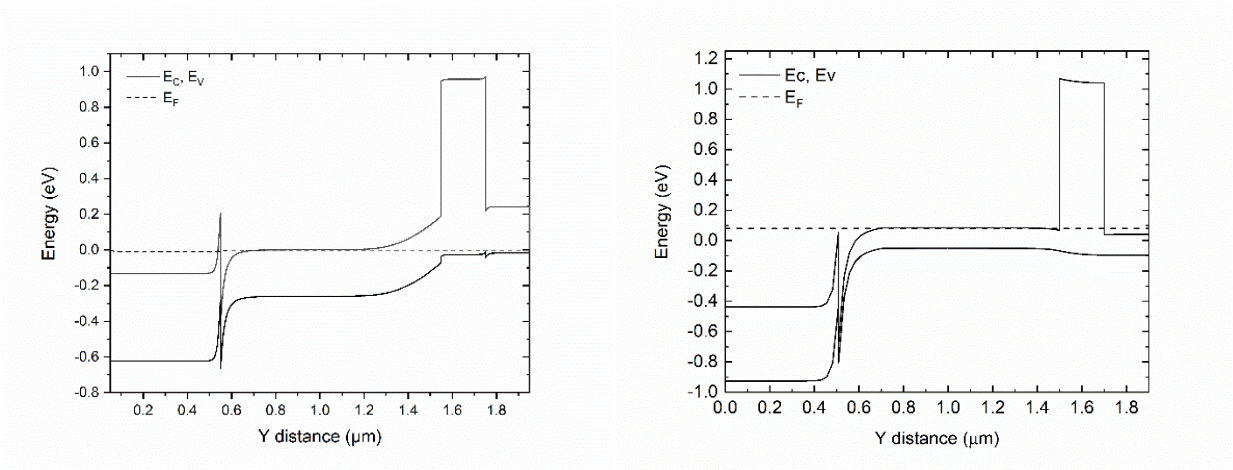

Figure 1- 1. Examples of the band diagram in (a) nBp structure and (b) nBn structure. Solid lines denote conduction band and valence band. Dashed lines denote Fermi level under equilibrium.

One of the advantages of using the barrier heterostructures is that ideally there is no depletion region existing in either of the narrow bandgap regions. By contacting the narrow bandgap region with the wide bandgap barrier, electrons will be re-distributed near the interface in the narrow bandgap layers, while the barrier is fully depleted. This can greatly suppress the generation-recombination (G-R) current initiated through the defect center which are responsible for Shockley-Reed-Hall recombination. Therefore, the G-R component of dark current can be suppressed and the dark current will be limited by diffusion current. In the narrow energy gap, the diffusion current is defined by the thermal generation of excess carriers from valence band to

conduction band. In equilibrium the thermal generation rate is equal to the recombination rate which is mainly attributed to Auger recombination. The Arrhenius plot in Ref. [4] also suggested a diffusion-limited dark current above the "cross-over" temperature in the barrier heterostructures, which means the barrier heterostructure devices exhibit greater sensitivity at the same temperature compared to that of the standard p-n diodes at low-temperature regime.

From the device design point of view, the barrier heterostructures are more complicated than homojunction pn diodes. The common issues in nBn devices include but not limit to: the valence band edge mismatch between the barrier and the absorber; the unknown doping in the barrier which results in a barrier blocking hole transport; strain balance in SLS absorbers and a lattice constant mismatch between absorber and barrier layers which can create a residual strain and defects due to uncontrollable strain relaxation. The valence band energy edge mismatch occurred at the barrier-absorber interface results in an impediment of hole transport from the absorber towards the contact, or conversely a band-to-band tunneling near the interface. The selection of compositions of compound materials as the absorber and the barrier requires the knowledge of the band potentials as well as the bowing parameter in the semiconductor compound alloys introduced by mixing two binary materials. A good reference for the former would be Ref. [17], and the latter is frequently lack of record and under investigation. On the other hand, choosing superlattice-based absorber introduces extra difficulty for the prediction of the valence band position and the heavy-hole miniband width.

The intentional doping in the barrier to compensate the background carrier concentration is tricky due to the unknown conductivity type and carrier concentration in the undoped barriers. N-type barrier leads to the formation of a potential bump in the valence band. The holes generated in the absorber do not have sufficient thermal energy to overcome such thick and high

potential barrier. The carriers are only capable of overcoming a potential barrier within $3k_BT$. Moreover, introducing moderate amount of acceptor dopants during growth can flatten the potential bump. But over-compensation of p-type dopant results in higher dark current due to the extended depletion region (Figure 1-1 (a)) at the barrier-absorber interface [7].

For the epitaxial growth on the commercially available substrate, the strain mismatch between the barrier heterostructure and the substrate needs to be resolved. A buffer can be used to accommodate the strain mismatch. However, growing thick absorber (> 2 μm) is still challenging and probably end up with defective absorbing layers.

1.2 Narrow band gap absorbers for infrared optoelectronics

Development of infrared (IR) optoelectronics is in demand in civilian and military applications. Although considerable portion of the infrared transmission spectrum is of little use due to the absorption of atmospheric gases, mid-wave infrared (3 – 5 μm) and long-wave infrared (8 – 14 μm) atmospheric windows can provide near 100% transmission, making them unique in the application of infrared imaging, night vision, LiDAR and remote sensing.

InAsSb as a ternary alloy has the smallest energy band gap among all III-V compounds. By growing unrelaxed unstrained InAs1-xSbx alloys, the low energy band gap of 85 meV at T = 77 K was achieved with a 60 % Sb [6]. Compared to mercury cadmium telluride (HgCdTe), a type of II-VI compound dominating the infrared photodetector market, InAsSb has the advantages of growth uniformity, compatibility with robust III-V manufacturing technology and a lower substrate cost. However, the performance of InAsSb-based photodetectors has not transcended [18] those state-of-the-art devices made of HgCdTe [19,20]. Some of the material (including optical and electrical) properties in InAsSb-based bulk and superlattices are still

unclear. Particularly, researchers nowadays are extensively studying the carrier transport properties in type-II InAsSb superlattices in order to establish the theoretical framework and understand how these properties impact the device performance [21–23]. Commonly used materials as narrow band-gap absorbers for infrared detection include HgCdTe, InSb, InAsSb, InAs/GaSb superlattices, InAs/InAsSb superlattices. Except for InAsSb, all above materials can be grown on CdZnTe, InSb and GaSb substrates pseudomorphically. InAs1-xSbx with a 9 % Sb can be grown lattice-matched to GaSb substrate. For extension of the response to the long wave infrared (LWIR) wavelength range, an increase of Sb composition is required to narrower the energy band gaps. Meanwhile, keeping a low residual strain of the epilayer grown on the substrate is essential to grow thick epitaxial layers for a more complete photon absorption. One solution to reach narrow energy gaps is to grow type-II strained-layer superlattices (SLS) with InAs/Ga(In)Sb and InAs/InAsSb cells on GaSb substrates. The requirement of strain balance with growth on GaSb substrate limits the windows of acceptable cell parameters for responsivity in LWIR range. Another solution is to grow either bulk InAsSb or InAsSb-based SLS absorners with a lattice constant greater than that of GaSb. To obtain a low dislocation density in the absorber this solution requires development of a metamorphic GAInSb or AlInSb buffer layer between GaSb and the absorber to accommodate the lattice constant mismatch. Currently, compositionally step-graded buffer [24] and linearly-graded buffer [25] have been reported. Optoelectronics Group has been studied linearly-graded buffer since 2011 [25] and demonstrated the first metamorphic growth of unrelaxed unstrained epitaxial $InAs_{1-x}Sb_x$ layer by solid-source molecular beam epitaxy (MBE) without Cu-Pt ordering. Photoluminescence under the excitation of excess carriers in heterostructures with carrier confinement was investigated in unstrained unrelaxed InAsSb alloys. The alloys were grown on metamorphic GaInSb buffers on GaSb

substrate. The Sb composition of InAsSb is ranging from 20 % to 65 % in the temperature range from 10 K to 200 K [6,26].

HgCdTe alloys are notable for long carrier lifetime, high electron mobility and flexibility of tuning band gap with Hg composition. However, growing uniform narrow gap HgCdTe over large area is challenging due to the high vapor pressure required by liquid metal mercury [27]. Regardless of the high costs and difficulties in growing and manufacturing, HgCdTe alloys provide unprecedented degree of design freedom with the extension of the responsivity toward longer wavelengths, realization of high quantum efficiency and low noise in both photoconductive and photovoltaic modes [27].

The main competitors of HgCdTe raise quickly nowadays. InAsSb and type-II superlattices have gained tremendous attention in the development of next-generation LWIR photodetectors. Binary InSb and InAs have notably high electron mobility [28], and their spectral responses are in mid-wave infrared range.

The advanced growth technology prevails the usage of low-dimension structures. The electronic band structure can be calculated by 8-band $\boldsymbol{k} \cdot \boldsymbol{p}$ method, tight-binding method, and nearly free electron model, etc. 8-band $\boldsymbol{k} \cdot \boldsymbol{p}$ method is a semi-empirical approximation using the perturbation theory with Bloch's theorem. Bloch's theorem describes periodic wavefunction in crystalline solid. 8 bands refer to the ground-state conduction band (C1), heavy-hole (HH), light-hole (LH) and spin-orbit band (SO), and each has 2-fold spin degeneracy. The simulation can be done in commercially available software such as Nextnano3 [29]. Figure 1 shows two examples of type-II superlattices simulated for InAs/InGaSb and InAs/InAsSb. Two structures have the estimated energy band gaps of 126 meV and 128 meV at gamma point at 0 K, respectively. It can be seen that a longer period is required in InAs/InAsSb to achieve the same cut-off wavelength.

One reason is that the absolute energy of valence band in GaSb is positioned higher than that of InAsSb. The other is attributed to a relatively higher compressive strain in InAsSb [30]. For strain-balancing purpose, a thicker InAs tensile-strain layer is needed to compensate the compressive strain in InAsSb layer. Thicker superlattice periods result in heavier hole effective masses and reduced hole mobilities in out-of-plane (vertical) transport.

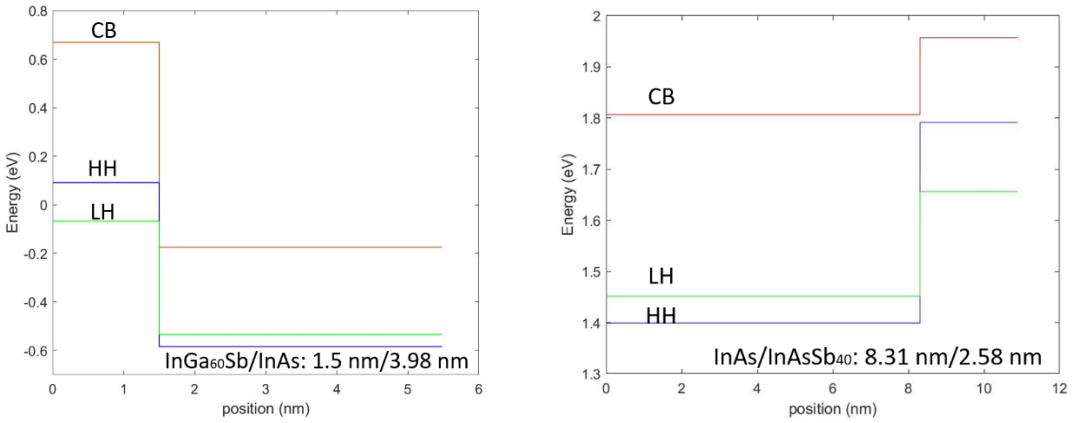

Figure 1- 2. band diagram of type-II superlattices for InAs/InGaSb (left) and InAs/InAsSb (right).

Nevertheless, Ga-free structures exhibit noticeably longer minority carrier lifetimes compared to SLS based on InAs/Ga(In)Sb grown on GaSb. For example, mid-wave IR InAs/GaSb type-II superlattices (T2SL) had an estimated carrier lifetime of 80 ns [8], while several mid-wave IR InAs/InAsSb T2SL structures demonstrated carrier lifetimes in the range of a few μs [23,31].

1.3 Applications in infrared optoelectronics

The main application of the barrier heterostructures is in unipolar photodetectors for MWIR and LWIR ranges. The nBn photodetector is commonly used as shown in Figure 1-1 (b). On applying negative bias to the contact, the holes generated by photon absorption diffuse to the barrier, drift through the barrier layer under the electric field, and recombines with electrons in

the contact layer. Meanwhile, the electron transport is blocked by the wide bandgap barrier. Despite the relatively small mobility, minority holes are selected as the transport carrier due to the naturally n-type barrier, where the surface leakage current is effectively reduced by the n-type barrier. For the application requiring multispectral capability, a dual-color barrier structure is available if layers with different bandgaps are used on each side of the barrier layer [32,33]. Two-color operation can be realized by changing the bias direction applied to the substrate and the contact. Besides the regular type-II superlattices, the exotic M-shape [34], N-shape [35], W-shape [36] superlattice absorbers and barriers were also demonstrated in the barrier photodetector.

Another application that will be illustrated in this dissertation is the beam intensity modulation [5,37] in Chapter 3. An nBp structure was used in this case for the carrier injection and confinement of holes and electrons from the contact side and the substrate side of the structure by applying a positive bias to the contact. The barrier was doped p-type to the level of 1x1017 cm-3 and the contact was doped to the level of 1x1018 cm-3 for hole injection. The modulation is realized by Burstein-Moss shift, a band-filling phenomenon of pushing the absorption edge of the active region to the higher energies. On top of that, beam steering can be realized based on the carrier-induced refractive index changes due to BM shift. Modeling of a double-barrier heterostructure in Chapter 4 also demonstrated the possibility of implementing integrated multiplexing arrays.

Chapter 2 InAsSb-based barrier heterostructures for photon detection

2.1 Introduction

InAsSb-based structures grown on metamorphic buffers with elevated lattice constant compared to that of GaSb , including type-II $InAs_{1-x}Sb_x/InAs_{1-y}Sb_y$ superlattices (T2SL) and bulk $InAs_{1-x}Sb_x$, broaden the windows of design parameters for further optimization of the performance of LWIR detectors with III-V compound absorbers. The Ga-free material system, such as $InAs(Sb_x)/InAsSb_y$ T2SLs, has an important advantage, i.e the minority hole lifetime is one magnitude greater than that with Ga-based materials, such as T2SLS of InAs/Ga(In)Sb grown on GaSb.

The important design advantage of III-V compound material systems is the seamless possibility to grow heterostructures with wide energy gap barriers. The barriers can effectively block the transport of majority carriers, either electrons in n-type absorbers or holes in p-type absorbers. Incorporation of the wide energy gap barrier with a low valence band offset blocks the electron component of current in n-type absorber, while the minority hole transport remains unimpeded by the barrier. Thus, the reduced depletion region in the narrow gap absorber of the barrier heterostructure can suppress the thermal generation of carriers, which is one of the major sources of dark current in the depletion region of the narrow gap absorber. While the barrier region is depleted, the thermally induced dark current in the wide bandgap barrier is insignificant.

A near zero valence band offset between the absorber and the barrier can be realized by tuning the composition of the layers comprising the heterostructure. A reduction of the dark current can be traded off for an increase of the detector operating temperature. A high operating

temperature (HOT) of the LWIR detectors becomes possible. High performance of InAs/$InAs_{1-x}Sb_x$ MWIR photodetectors was demonstrated at elevated temperatures compared to conventional InSb detectors operating only at temperatures of liquid nitrogen range [38].

Nowadays, the performance in photodetectors composed of T2SL as absorbers is approaching that in the state-of-the-art HgCdTe photodetectors in terms of operating temperature, dark current and cut-off wavelength stipulated under Rule07 [20,39,40]. Growth of superlattices can extend the cut-off wavelength compared to that of bulk material on the same lattice constant platform. For example, InAs/$InAsSb_{0.4}$ T2SL pseudomorphically grown on GaSb substrate can have a band gap in long-wave infrared (LWIR) range at 10 μm. For comparison, the bulk $InAsSb_{0.09}$ materials grown lattice matched to GaSb substrate has a cut-off wavelength of less than 5 μm at low temperatures. Although the vertical hole transport in InAs/InAsSb type-II superlattices (T2SL) is greatly suppressed by hole localization at the sites in InAsSb part of SLS cell as temperature decreases [31], the relatively long minority carrier lifetime results in a long enough hole diffusion length to provide the practically good responsivity of LWIR photodetectors. In the temperature range above 67 K, the out-of-plane hole transport in type-II SLS for LWIR range was reported to be dominant by hole tunneling [22].

Exploring the material parameters in InAsSb and type-II Ga-free SLS, such as minority carrier mobility and lifetime for better understanding of the material capabilities have attracted the attention of many research groups. Several recent works were concentrated on the study of vertical hole mobility in narrow-gap type-II InAs/InAsSb SLS for LWIR detectors. The data were varied tremendously from 1.6 cm^2/Vs to 80 cm^2/Vs at 77 K using different characterization methods [21–23], where Casias et al. evaluated the anisotropic carrier transport in InAs/$InAsSb_{0.35}$ by magnetotransport measurements and obtained a vertical hole mobility of 1.60

cm^2/Vs at 77 K; Olson et al. applied T2SL in a heterojunction bipolar transistor and extracted the hole mobility values from the common base-current gain. The hole mobility of 120 cm^2/Vs at 77 K was reported. Meanwhile, the theoretical simulation was also investigated using nonequilibrium Green's function to model type-II superlattices [41], and reported a hole mobility of 12 cm^2/Vs at 77 K.

In this chapter, the discussion will be focused on the determination of the vertical hole mobility and the minority hole lifetime from the transient photocurrent response of barrier (nBn) heterostructures with different designs. Two barrier heterostructures with type-II SLS absorbers were grown by MBE with the target energy gap in LWIR at the wavelengths of 10 μm.

2.2 Long-wave infrared photodetector based on InAsSb Type-II superlattice absorber

2.2.1 Modeling of T2SL absorber

Four nBn barrier heterostructure designs with different absorber and barrier compositions were proposed. The responsivity cut-off wavelength was targeted to be 9-10 μm at the liquid nitrogen temperature. Two absorber designs (No.1-2) were composed of InAs/$InAs_{1-x}Sb_x$. These superlattice structures were designed for the growth latticed matched (pseudomorphically) to GaSb substrate. The lattice constant of GaSb substrate is 6.09 Å and the average Sb composition in SLS for this lattice constant is 9.5 %. Sb composition of x = 40 % can be grown by MBE with a compressive strain of 2 %. An Sb composition of x > 50 % with a higher compressive strain were reported [42,43]. However, for this work, it was decided to keep the compressive strain below 2 % for growth reliability.

Table 2- 1. Summary of four designs of absorber in nBn photodetectors

No.	$InAs_{1-x}Sb_x$	$InAs_{1-y}Sb_y$	Lx (nm)	Ly (nm)	Eg (eV)	Miniband Ev (meV)
1	0	0.40	8.31	2.58	0.12	0
2	0.03	0.40	8.3	2.6	0.125	0.0001
3	0.30	0.55	3.3	1	0.136	27.5
4	0.25	0.55	2	1.1	0.138	63.6

Another two heterostructure designs (No.3-4) had the absorbers incorporating $InAs_{1-x}Sb_x/InAs_{1-y}Sb_y$ SLS grown on GaInSb metamorphic buffers with a lattice constant greater than that of GaSb. These superlattices had a higher average Sb composition compared to that with pseudomorphic growth on GaSb. In design No.3, the average Sb composition was estimated to be 36 %. Use of the elevated lattice constant made it possible to grow shorter periods of superlattices to enhance the vertical hole transport through the SLS barriers. The compositionally graded GaInSb metamorphic buffer between the substrate and the absorber was used to accommodate the lattice constant mismatch with a high-quality, low-defect-density absorber. The buffer was followed by an unstrained unrelaxed virtual substrate with a constant Sb composition. The virtual substrate had a 500-nm $Ga_{0.7}In_{0.3}Sb$ layer with the lattice constant of 6.20 Å.

The dispersion of energy bands in k-space was studied by 8-band $\boldsymbol{k} \cdot \boldsymbol{p}$ method. The simulation was done in Nextnano3 [29]. The SLS design details are summarized in Table 2-1. Miniband Ev represents the miniband width calculated as the valence band offset between k = 0

at Γ point and max k = $\frac{\pi}{L_x+L_y}$. This concept is similar to the energy dispersion in Brillouin Zone.

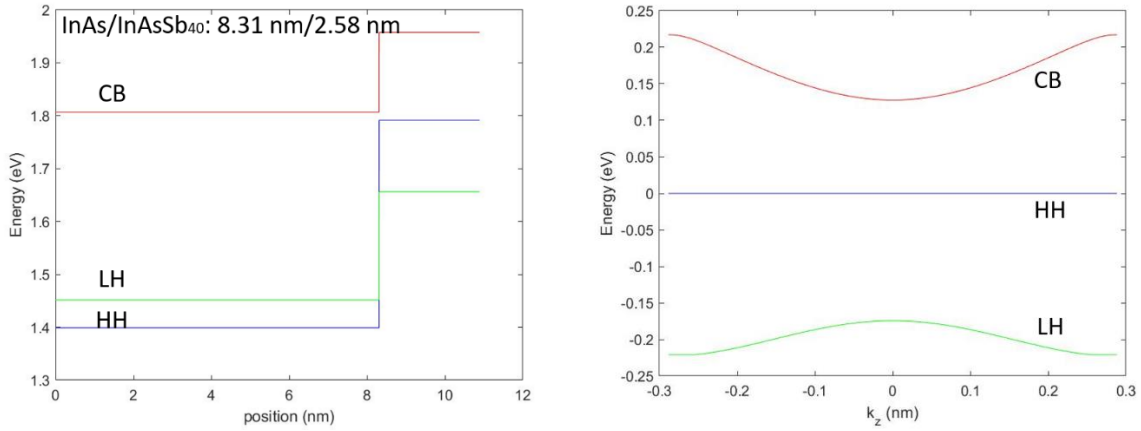

Figure 2- 1. The band diagram (left) and k-space energy dispersion (right) in long-period SL, the absorber is design No.1 in Table 2-1.

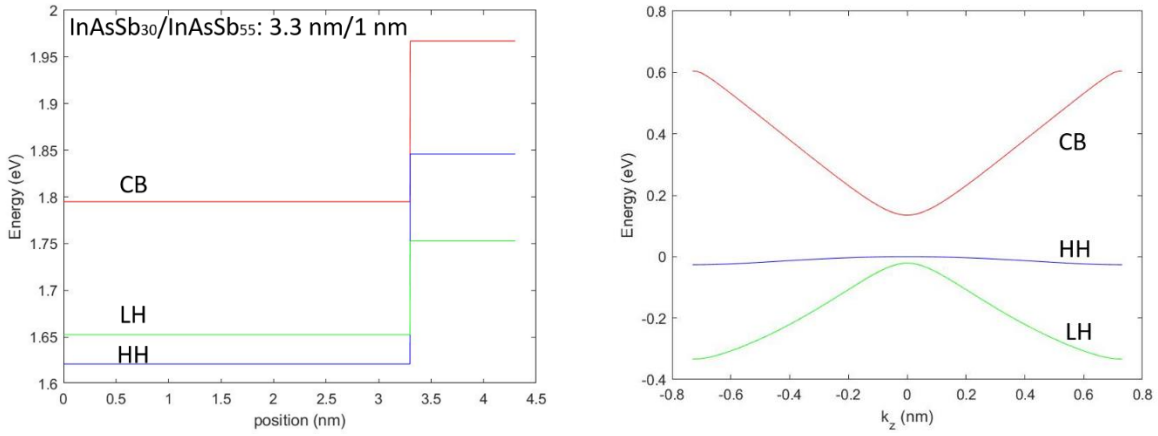

Figure 2- 2. The band diagram (left) and k-space energy dispersion (right) in short-period SL, the absorber is design No.3 in Table 2-1.

Below the designs No.2 and No.3 are referred to as long period and short-period SLS. Comparing short-period (SP) and long-period (LP) superlattice absorbers, use of $InAs_{1-x}Sb_x/InAs_{1-y}Sb_y$ structure reduced the period by 2.6 times while preserving the same energy band gap. The average Sb composition has a substantial impact on the energy band dispersion, especially on the width of heavy-hole (HH) miniband. The heavy-hole miniband increased significantly from 0 meV in the LP to 27.5 meV in the SP heterostructure which resulted in an

improvement of the vertical hole transport and the vertical hole mobility in the SP SLS compared to that in the LP SLS.

2.2.2 MBE growth, fabrication and material characterization

Four barrier heterostructures with wafer numbers D1638, D1631, D1642, D1644 were grown by Molecular Beam Epitaxy, with the absorbers described in Table 2-1. D1638 and D1631 had the same superlattice period, while they were grown with As and Sb background, respectively. D1638 was grown with growth interruption for stabilization of Sb flux in order to obtain sharper SLS interfaces. The latter characterization results are presented for D1638 and D1642, referred to as long-period (LP) and short-period (SP) SLS. The long-period SLS was composed of InAs/$InAsSb_{0.36}$ with 83 Å/26 Å layer thicknesses, whereas the 4.3-nm short-period SLS was composed of $InAsSb_{0.30}$/$InAsSb_{0.55}$ with the layer thicknesses of 33 Å/10 Å.

The nBn heterostructures consisted of a 2 μm thick unintentionally doped superlattice absorbers followed with a wide bandgap undoped bulk AlGaInSb barrier layer and a heavily Te-doped superlattice top contact of the same composition as the absorber. The background concentration was n-type with an electron concentration in the low 10^{15} cm^{-3} range [44]. The barrier layers were grown with a thickness of 0.3 μm and the compositions targeted to lattice matching to the SLS and a zero valence band offset with the absorbers. The barrier photodetector designs were targeted to have a diffusion-limited dark current due to minimal width of the depletion region in the absorbers. The barrier heterostructure design allows for reduction of the dark current due to generation-recombination in the depleted part of the absorber. Ideally, the absorber of barrier heterostructure has no electric field. Thus, no drift of carriers is involved, and the dark current is diffusion limited. With minimization of the depleted width of the absorber at

the interface with the barrier, the role of Shockley-Read-Hall recombination in the dark current was reduced [45].

The photodetectors with the long-period SLS were fabricated with 600 μm × 600 μm mesa sizes for the frontside side defined by wet etchig using a stop etcher of H_2O:H_2O_2:citric acid = 75 mL:25 mL:25 mL. The wafer was coated with 400-nm thick Si_3N_4 by PECVD, retaining a 560 μm × 560 μm open area in the center of the mesa for p-side Ti/Pt/Au metal deposition. The surrounding Si_3N_4 strip with a width of 20 μm allowed for the epilayer side (frontside) laser excitation by photons penetrated through the dielectric layer. The substrate side (backside) was deposited with Ni/Au/Ge/Ni/Au metal alloys followed by Ti/Pt/Au. The backside open windows obtained by metal liftoff were aligned center-to-center with the frontside metal contacts in a dimension of 400 μm × 400 μm. The fabrication of smaller backside window constrained the transport for holes to vertical direction only by eliminating lateral carrier spreading under backside laser excitation. The schematic cross-sections of the nBn detectors for study of the hole transport kinetics are shown in Figure 2-3a.

The processing of short-period SLS followed the same procedure except for the mesa sizes. A set of 50 μm, 100 μm and 200 μm mesas was defined for the frontside metal contacts and a common 600 μm × 600 μm was defined for substrate side open windows. A mixture of vertical and lateral diffusion occurred in SP structure under substrate-side laser excitation. The higher vertical hole mobilities allowed for the simple separation of vertical and lateral transport signals. It was clearly observed that the transient response composed of two sections with fast and slow constants.

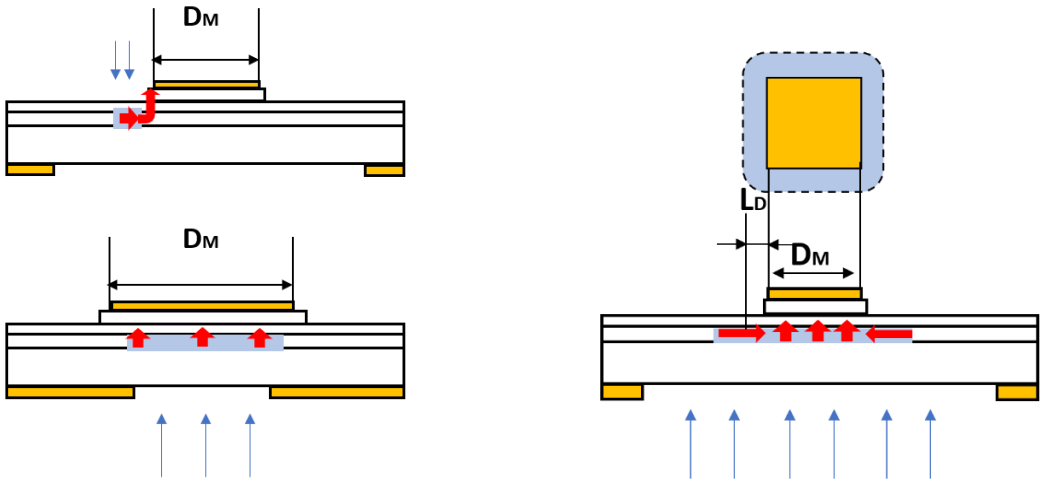

Figure 2- 3. Schematic of frontside and backside illumination in LP structure (left). It facilitates the separation of vertical diffusion from lateral carrier spreading by making smaller backside windows. A mixture of vertical and lateral transport occurred in SP structure (right). A higher vertical hole mobility allowed for the simple separation of these two signals by analyzing the fast and slow slopes of the transient response.

The structural characterization was performed by x-ray diffraction and bright field TEM as shown in Figures 2-4. No Cu-Pt ordering in SLS was observed. The bright field TEM showed the alternate superlattice growth with clear interface boundaries in both the long-period SLS absorber and short-period absorbers.

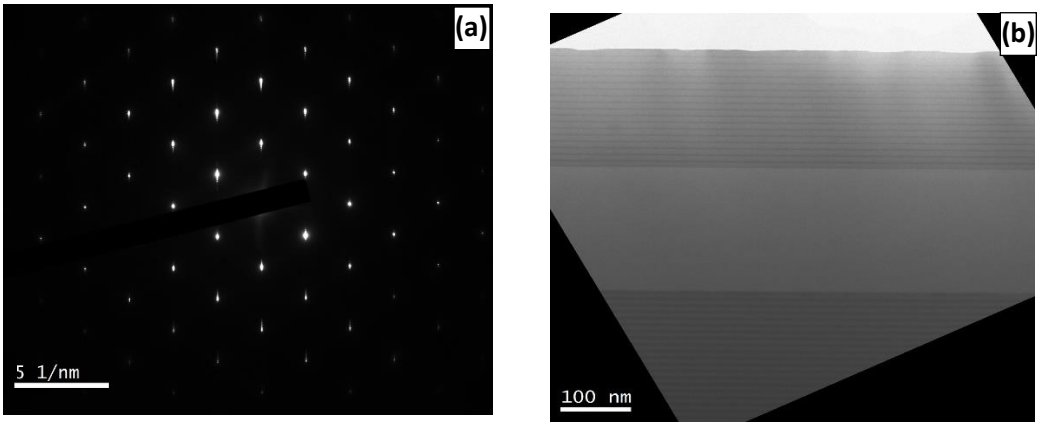

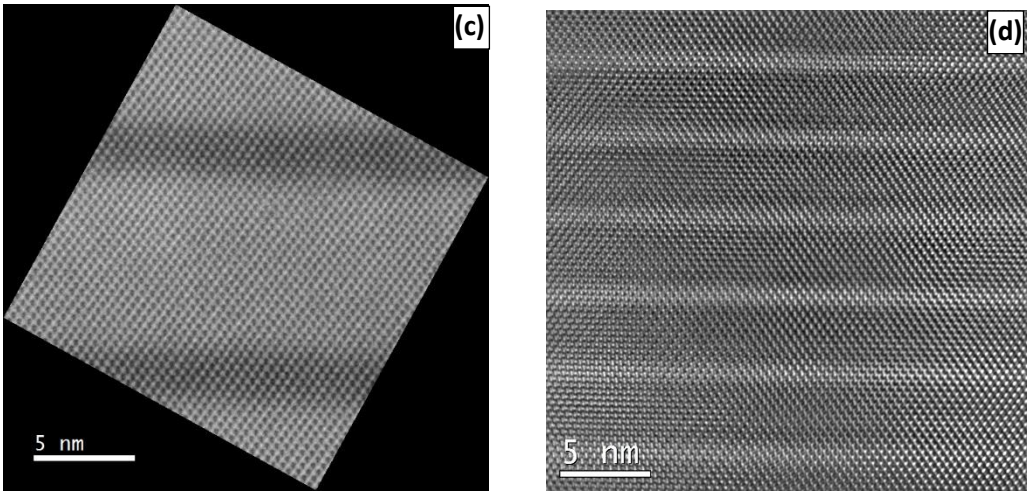

Figure 2- 4. (a) Electron diffraction shows no Cu-Pt ordering. (b) 100nm-scale nBn structure, both the absorber and the contact are composed of LP superlattices. (c) 5nm-scale zoom-in view of LP absorber. (d) 5nm-scale zoom-in view of SP absorber.

2.2.3 Electrical and optical characterization

In this subsection, the results of nBn characterization including I-V characteristics, photoluminescence (PL), transient response, and responsivity spectra are discussed.

I-V characteristics were measured in the cryostat with cooling down to the liquid nitrogen temperature. The magnitude of the dark current density in long-period SLS was in mA/cm^2, similar to that in undoped bulk InAsSb absorber. The slope of the temperature dependence of current density indicated an activation energy of 133 meV and a diffusion-limited behavior above 165 K.

I-V characteristics in short-period SLS was also measured. The dark current density was studied in the device with a mesa size of 50 μm at 77 K. The current was suppressed at low bias quickly rising after 0.45 V. This shape of the response vs bias was attributed to the valence band mismatch at the absorber-barrier interface and unintentional n-type background doping of the barrier layer which block the hole transport at low bias. The device was not fully turned on before 0.3 V, but it still had some of carriers “leak” through the barrier.

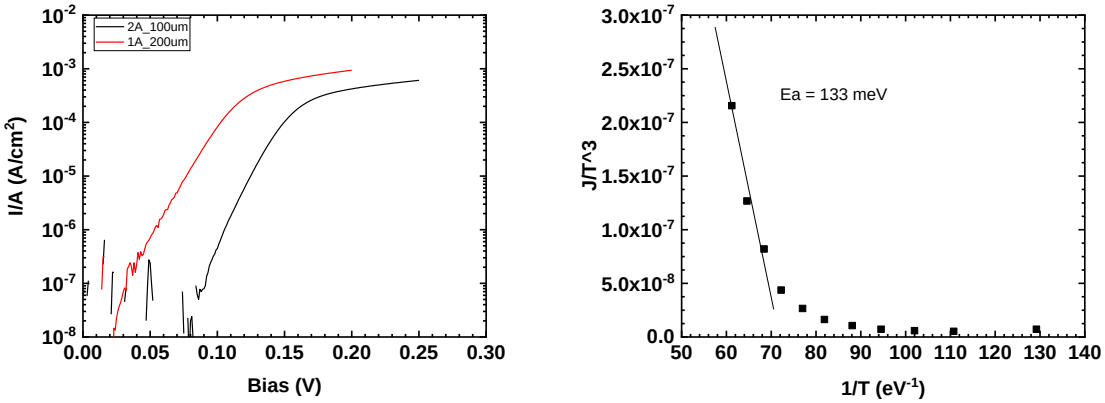

Figure 2- 5. (a) Current density as a function of bias at 77 K. Black and red curves show the I-V characteristics for the device with frontside mesa sizes of 200 nm and 100 nm, respectively. (b) Dark current density as a function of reciprocal temperature. The slope in the diffusion-limited regime above 165 K represents the activation energy. It usually indicates the energy band gap in undoped absorbers.

The dark current density was ten times greater than that in long-period SLS at the operating point, i.e. 0.01 A/cm^2. Although the valence band alignment was studied with the up-to-date valence band bowing parameter of 0.4, meantime there is no bowing in AlInGaSb barrier, a large turn-on bias was inferred to an obstacle for hole transport created by (1) no p-doping used to compensate the naturally n-type barrier or (2) insufficient bowing assumed for valence band. Figure 2-6(b) shows a non-diffusion-limited behavior throughout the temperature range.

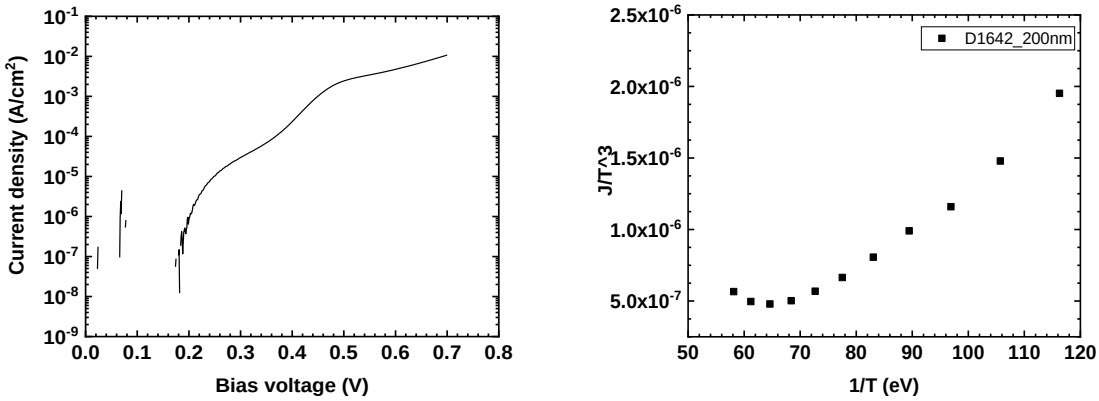

Figure 2- 6. (a) I-V characteristics for short-period SLS structure measurement at 77 K. (b) temperature dependence of dark current density. The diffusion-limited behavior was not observed in this short-period SLS.

The response as a function of bias was studied with a 3-μm laser, a lock-in amplifier and a transimpedance amplifier shown in Figure 2-7. For long period SLS heterostructure, the turn-on bias of 0.25 V was found. This value was better than most of the nBn structures measured in the past in our group [6,7,46], except for the one structure using quinary barrier for bulk $InAsSb_{0.40}$. On the other hand, a turn-on bias of 0.7 V was found for the short-period SLS heterostructure. The best data reported using Sb-based barrier was 0.42 V by Ding et al [7], where a p-type doping of 1e16 cm^{-3} was incorporated during MBE growth.

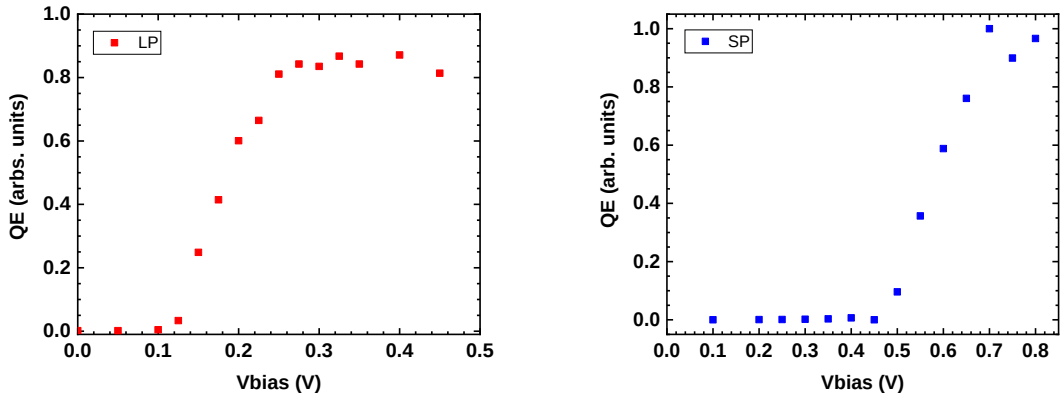

Figure 2- 7. Bias-dependent responses for the long-period (a) and the short-period SLS (b) heterostructures. The turn-on bias voltages were determined to be 0.25 V and 0.7 V, respectively.

In Ding's work, a major part of the large turn on voltage was resulted from the high doping of the contact layer of n = 1e18 cm^{-3}. In two heterostructures discussed in this section, the top contact doping was selected to be n = 1e17 cm^{-3}, which could justify the bias voltage of 0.2 V or less. Our modeling of I-V characteristics of nBn heterostructures with various valence band offsets (VBO) between the absorber and the barrier layers showed that, a 30-50 meV VBO cannot justify the bias voltages of 0.7 V range in the case of a moderate doping of the contact layer. It was concluded that, a p-type doping in the barrier at the level of 1e16 cm^{-3} is required to reduce the bending down of the potential profile in the vicinity of the barrier. The bending-down

potential (a bump) of the valence band blocked the hole transport, which resulted in a large turn-on bias of the device.

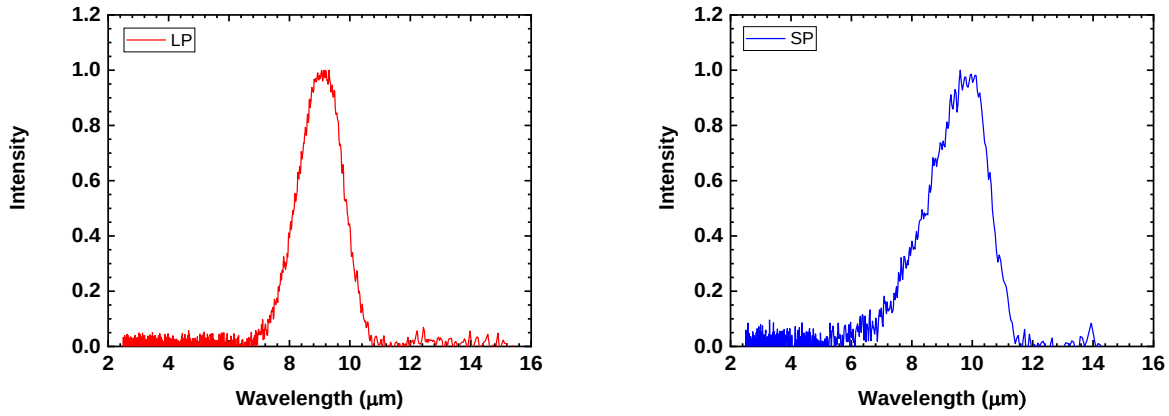

Figure 2- 8. Photoluminescence measurements at T = 77 K with excitation at the wavelength of 1.5 μm. The long-period SLS (a) showed a max intensity at 9.5 μm, and the short-period SLS (b) showed a max intensity at 10 μm.

The photoluminescence (PL) was measured for both SLS heterostructures with the excitation at the wavelength of 1.5 μm using a diode laser. The temperature dependences of PL for the wafer-level D1638 and D1642 were studied. Strong PL peaks were confirmed near 9 – 10 μm at low temperatures. The PL spectra at T = 14 K were fit with a Gaussian shape. The PL peaks were obtained at the wavelengths of 10.1 μm and 9.7 μm for the long-period and short-period SLS heterostructures, respectively.

The quantum efficiency (QE) spectra were measured by Nicolet FTIR with a KBr beam splitter and an internal globar with the heterostructure illumination from the substrate side. The calibration of QE spectra was done with the diode laser excitation at the wavelength of 2 μm. No anti-reflection coating was deposited to the nBn surface. The n-doped metamorphic buffer led to considerable reduction of photons absorbed in the absorber due to fundamental absorption. This reduction was calibrated out [47] and a peak quantum efficiency of 63 % was found in SP structure. The LP structure did not have absorbing buffer and it showed a max QE of 40 %. This

discrepancy was due to shorter minority hole lifetime and smaller hole mobility in LP structure. At long-wave infrared region, the response of both structures was significantly attenuated by free-carrier absorption in heavily doped GaSb substrate. The free carrier absorption was estimated to be 100 cm^{-1} at a 10 μm wavelength. The high QE in the short-wave infrared region confirmed that the majority of generated excess carriers reached the top metal contact. The QE spectra are presented in Figure 2-9.

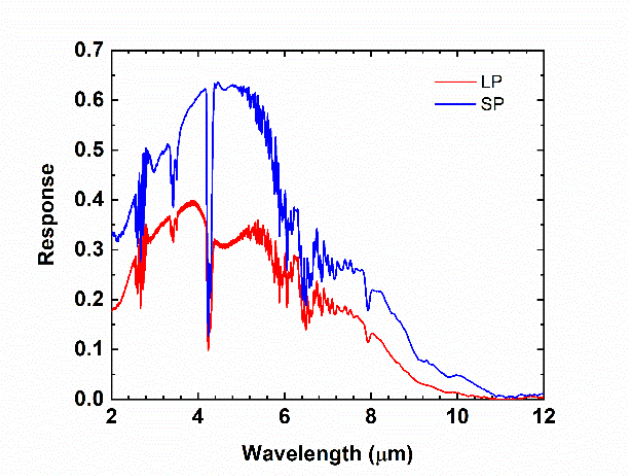

Figure 2- 9. Quantum efficiency spectra for LP and SP structures. Max quantum efficiencies of 40 % and 63 % were measured at 4-5 μm in LP and SP, respectively.

The carrier lifetime data were determined from the transient response to a pulsed 2-μm laser excitation with backside illumination. For comparison, the carrier lifetime was extracted from the response decay with the epi-side excitation with a 1064 nm Q-switched solid-state laser. The preamplifier was connected to the photodetector with 80 MHz bandwidth and 50 Ohm impedance. The system response of 2 ns was not influencing the determination of the transient response time of the nBn photodetectors. The carrier lifetime was obtained at the trailing edge of response after the end of the laser pulse. Reciprocal of the slope in log-linear scale is the transient time based on equation $\exp(-t/\tau)$.

In LP structure, the transient time was measured with a single slope from both frontside and backside illumination. The minority hole lifetime was obtained in the device with a frontside mesa of 100 μm and a backside window of 600 μm. The minority hole lifetime was measured to be 207 ns at 77 K. The transient time for extracting hole mobility was complete in the device with a frontside mesa of 600 μm and a backside window of 400 μm. A smaller backside window eliminated the disturbance from the lateral carrier transport. Temperature dependence of the transient response decay and the hole lifetime were illustrated in Figure 2-10. Due to the slow vertical hole transport tunneling through the long-period superlattices, the separation of vertical and lateral response was difficult in this structure.

In SP structure, the transient response comprised of the fast decay and slow decay sections. The fast decay was attributed to the vertical hole transport from the absorber to the top metal contact along the growth direction. It first behaved as a diffusion of holes in the absorber towards the absorber-barrier interface, then the electric field in the barrier could rapidly move the carriers towards the top contact layer as a drift current. The transit time caused by drift was negligible [46]. Therefore, we attributed the time constant of fast decay to the diffusion of carriers in the 2-μm-thick absorber.

The long decay was occurred because of the lateral hole diffusion. The long decay time constant due to the lateral hole diffusion was used to determine the minority hole lifetime. In the SP structure at 77K, the minority hole lifetime of 555 ns was measured. The excess carriers were collected within one diffusion length from the mesa contact edge. The intensity of fast decay is proportional to the area of metal contact D_M^2, while the intensity of slow decay is proportional to the peripheral area in one diffusion length determined by $4L_DD_M$. The intersection shown in Figure 2-9(b) should be the point where the intensity by fast decay D_M^2 had the same

contribution as that by slow decay $4L_DD_M$. If a set of devices with difference mesa sizes were measured, the x value of the intersection is exactly four times diffusion length. As we applied this method to analyze the temperature-dependent two-stage decay, the hole mobilities in the entire temperature range from 77 K to 150 K were obtained by $L_D = \sqrt{D\tau}$, where $D = \mu V_T$ is the diffusion coefficient and τ is the carrier lifetime.

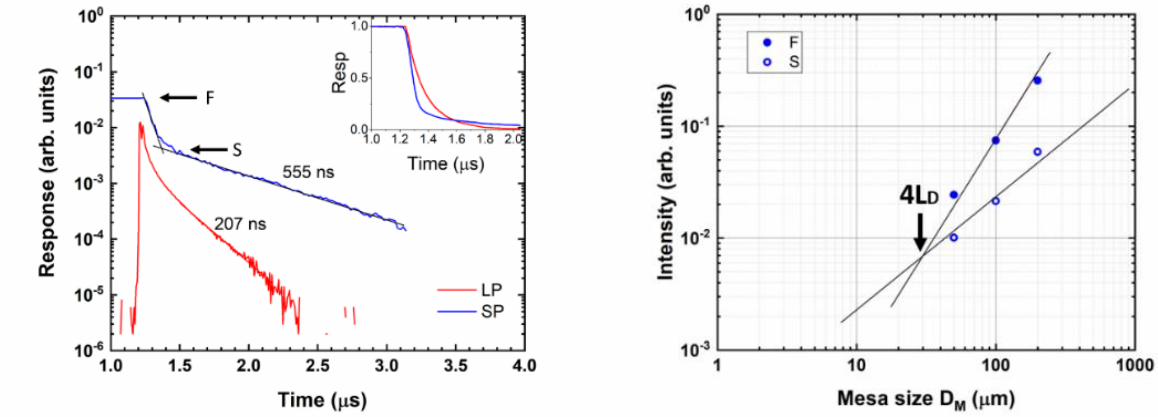

Figure 2- 10. Determination of minority hole lifetime and hole mobility from the transient response. (a) the lifetimes were measured to be 207 ns and 555 ns in LP and SP structures, respectively. Inset shows the same responses in linear scale. (b) Determination of the diffusion length was done by the fast and slow decay intersection.

From the transient response measurements, it was concluded that the minority hole lifetime and hole mobility were a factor of two greater in the SP SLS compared to those in the LP SLS. It indicated that a higher average Sb composition and shorter period of superlattices resulted in a better hole transport. A summary of the transient time constant due to vertical transport and the minority hole lifetime determined by fast-slow decay intersection method were illustrated in Figure 2-11.

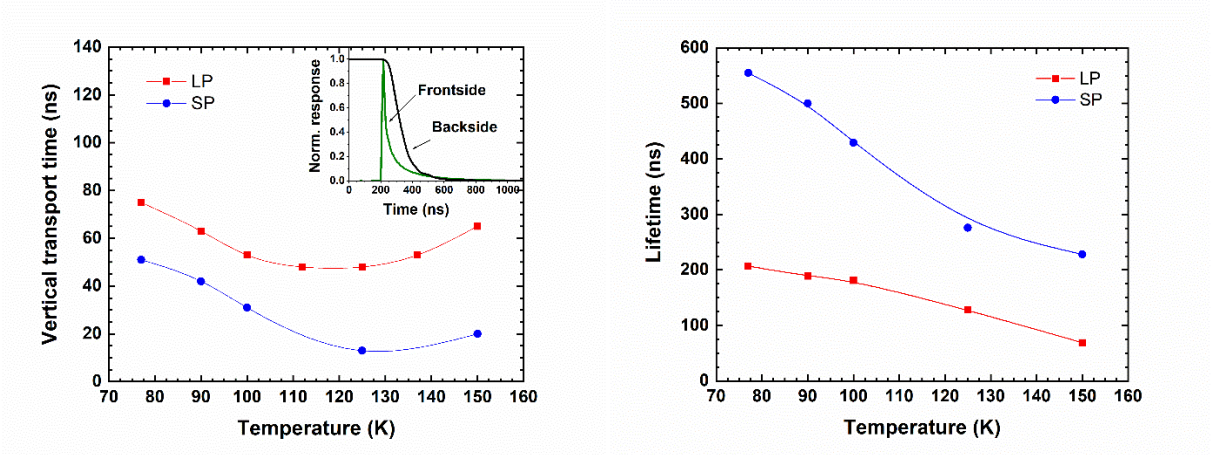

Figure 2- 11. (a) Temperature dependence of the transient time due to vertical hole transport. The inset shows the example the response illuminated from frontside and backside in LP structure. (b) Temperature dependence of the minority hole lifetime in LP and SP structures.

2.2.4 Analysis of temperature-dependent hole mobility

Apart from lateral hole mobility in SP structure, extraction of the temperature-dependent vertical hole mobility in two heterostructures were obtained by post-experiment modeling of the transient responses for various mobility and fitting of them to the experimental data. For modeling, COMSOL Multiphysics with the semiconductor module was used in the drift-diffusion approximation. The model accounted for a finite absorption coefficient of the 2-μm laser which resulted in the initial excess carrier distribution at the time of turning off the excitation laser. The complete nBn heterostructure with the virtual substrate, the absorber, the barrier and the contact layers was described. The model was using the unipolar hole transport. The operating bias was selected at the voltage where the dependence of the current on the bias reached saturation. The transient responses were modeled in a range of hole mobility for the experimentally determined lifetime at each temperature. Thus, the hole mobility was determined from the fit of the modeled and measured transient responses with the account for the experimental minority hole lifetime.

Independently from COMSOL modeling, the transient response of a photocurrent in a narrow gap absorber with an abrupt tune off of the excitation was determined analytically using the diffusion equation with a carrier recombination term and the appropriate boundary conditions. The solution is a Green's function expressed as an infinite sum as shown in Equation 2.1, [48]

$$p(x,t) = \frac{1}{w} e^{-t/\tau} \sum_{n=1}^{\infty} \int_0^{2w} f(\xi) sin\left(\frac{n\pi}{2w}\xi\right) d\xi \; sin\left(\frac{n\pi}{2w}x\right) exp\left(-D\left(\frac{n\pi}{2w}\right)^2 t\right) \quad n = 1,3,5 \ldots, \qquad (2.1)$$

where $p(x,t)$ is time-resolved hole concentration, w is the layer thickness of the absorber, τ is the minority hole lifetime. The integrand term $f(\xi)$ is the steady-state hole distribution at t = 0 as follows, [48–50]

$$f(x) = p(x,0) = A\, exp(\alpha x) + Bexp\left(\frac{x}{L}\right) + Cexp\left(-\frac{x}{L}\right), \qquad (2.2)$$

$$A = \frac{F_0(1-R)\alpha L^2 exp\,(-\alpha w)}{D(\alpha^2 L^2 - 1)}; \qquad B = \frac{-F_0(1-R)\alpha L^2 exp\,(-\alpha w)}{D(\alpha^2 L^2 - 1)}\left(\frac{exp\left(-\frac{w}{L}\right) + \alpha L exp(\alpha w)}{2cosh\left(\frac{w}{L}\right)}\right);$$

$$C = \frac{F_0(1-R)\alpha L^2 \exp(-\alpha w)}{D(\alpha^2 L^2 - 1)}\left(\frac{\alpha L exp(\alpha w) - exp\left(\frac{w}{L}\right)}{2cosh\left(\frac{w}{L}\right)}\right),$$

where the F_0 is the photon flux density from the laser excitation, R is the reflectance of the air-semiconductor interface; α is the absorption coefficient from similar superlattice design [51]; D and L are diffusion coefficient and diffusion length, respectively.

In the case of the undepleted absorber, the boundary conditions [50] were taken into account as Neumann boundary for the substrate-side window and Dirichlet boundary for the frontside contact where it sinks all the carriers. The time constant for the carriers swept out of the barrier layer due to high electric field is negligible [46]. Instead of a delta function representing a pulsed signal normally found in literatures, the initial condition should be a steady-state solution that describes the carrier distribution stabilized after a period of time exposed to the injected photons. Then the convolution of the initial distribution and the fundamental solution of the

diffusion equation should be used and depicted as the integral term in Equation 2.1. Details can be found in Appendix.I.

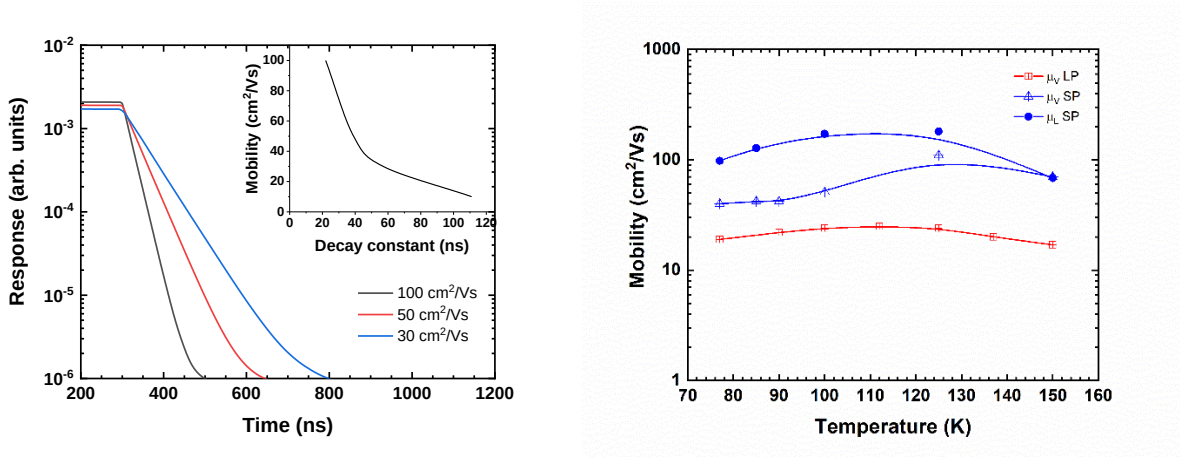

Figure 2- 12. (a) Hole mobility was obtained by modeling in COMSOL Multiphysics. The transient response with the initial steady-state solution was described under three different hole mobilities, i.e. 100, 50 and 30 cm2/Vs. Inset shows the hole mobility as a function of decay constant. (b) Temperature-dependent mobilities are illustrated for vertical transport in LP structure (red square), vertical transport in SP structure (blue triangle) and lateral transport in SP structure (blue circle).

Comparing the results of COMSOL modeling with Green's function, both showed the same trend, with at most 10 % discrepancy of hole mobilities at each temperature below 137 K where the hole lifetime data were measured. At the next experimental point of carrier lifetime, T = 150 K, considerable differences between results obtained with the COMSOL and analytical modeling approaches were observed: a three times greater mobility in the LP SLS heterostructure, and a 20 % greater mobility in the SP SLS heterostructure in COMSOL model compared to the analytical model. Most likely the COMSOL modeling considered other factors, such as concentration in each layer, temperature dependence of intrinsic concentration, a potential profile in the interface region between the absorber and the barrier, etc.

COMSOL modeling showed that variation of simulation parameters such as doping in the barrier layer in the range from undoped to n = 1e16 cm^{-3}, and the valence band offset between the absorber and the barrier layers from zero to 30 meV could lead to an increase of the decay

constant up to 20 ns. In contrast, Green's function simplified it to a diffusion process of an established carrier distribution in the absorber after turning off the excitation. Since the difference of the hole mobility obtained with COMSOL and analytical models was observed only at the highest measured temperature point of T = 150 K, it was concluded that involving the intrinsic carrier concentration in the absorber in COMSOL modeling played the major role in the discrepancy of hole mobility values obtained with two approaches. The analytical model for the InAsSb-based absorbers with the energy gaps of 0.13 eV was found to be adequate in the temperature range below ~130 K.

2.2.5 Conclusion

To summarize Section 2.2, a set of nBn heterostructures using Type-II superlattice absorbers were modelled, fabricated and characterized for study of the vertical and lateral transport in the barrier heterostructures with Ga-free SLS absorbers with two SLS periods. The T2SL energy band gaps and band dispersions in k-space were simulated in Nextnano3 by 8-band $k \cdot p$ method. Estimation of the energy band gaps were targeted at 9-10 μm at liquid nitrogen temperature. Four structures were grown by Molecular Beam Epitaxy including two pseudormorphic-grown structures on 6.09 Å platform and two metamorphic-grown structures on 6.20 Å platform. Then two of these heterostructure, labeled as long-period (LP) and short-period (SP) were extensively studied: a 4.3-nm short-period $InAsSb_{0.3}/InAsSb_{0.55}$ and a 10.9-nm long-period $InAs/InAsSb_{0.36}$. Photoluminescence demonstrated peak emission at 9-10 μm at 14-77 K. The turn-on biases were determined to be 0.25 V and 0.7 V in LP structure and SP structure, respectively. The difference in turn-on bias indicated a better valence band alignment in LP structure. Temperature dependence of the hole transport were explored by the transient response with a 2- μm pulsed laser diode and 1064-nm Q-switched solid-state laser. The minority lifetimes

were derived by fitting the transient response decay. The lifetime was found to be 207 ns in LP structure and 555 ns in SP structure at 77 K. By COMSOL modeling using drift-diffusion approximation, the vertical hole mobilities were 40-100 cm^2/Vs in SP structure and 20-25 cm^2/Vs in LP structure at temperatures from 77 K to 150 K. A factor of two greater hole mobility and minority hole lifetime led to an increase of quantum efficiency. However, it should be noted that for the absorber thickness of 2 μm, the increase of the hole diffusion length in the SP heterostructure compared to that in the LP heterostructure was not able to justify the difference in the QE of 40 % in the LP and 63 % in the SP heterostructures. The QE difference was attributed to hole delocalization and a better overlap of the electron and hole wavefunctions in the short-period superlattices compared to that in long-period superlattices.

2.3 Long-wave infrared photodetector based on bulk InAsSb absorber

2.3.1 Motivation

Achievement of background limited operation with InAsSb-based barrier heterostructures in LWIR range is a trending research topic. In the mid-wave infrared (MWIR) range, InAsSb-based compound barrier detectors showed background limited operation at much higher temperatures compared to that of InSb [38]. It was also shown theoretically that InAsSb-based detectors grown on GaSb substrates can have the performance comparable to those made of HgCdTe [52]. Two approaches to development of MWIR and LWIR detectors on GaSb substrates are being pursued: with unintentionally doped (n-type) InAs/InAsSb SLS absorbers and with p-doped GaInSb/InAs SLS absorbers both grown pseudomorphically on GaSb substrates. Both approached can provide sufficient collection of minority carriers due to long

enough diffusion length. The vertical hole mobility in n-type InAs/InAsSb SLS of 1-100 cm^2/Vs [22] and the minority hole lifetime up to 8 μs at T = 80 K were reported. In p-type Ga(In)Sb/InAs SLS, a relatively short electron lifetime (10-30 ns at T = 80 K) is compensated by high electron mobility in the scale of 10,000 cm^2/Vs at T = 80 K [53]. A decrease of hole mobility in InAs/InAsSb SLS at elevated temperatures was reported [21,54]. With both approaches the strain balancing implies a relatively large thickness of InAs section of SLS cells which results in hole localization, a reduced electron-hole wavefunction overlap and reduced absorption strength compared to bulk alloys. Bulk InAsSb alloys to cover the LWIR range up to 12 μm at low temperatures can be grown with large Sb composition on graded GaInSb and AlInSb metamorphic buffers. With the metamorphic growth, InAsSb alloys with the high absorption matching to that of MCT was demonstrated. Thus, with bulk InAsSb alloy absorbers the LWIR detectors with high QE can be realized. The direct measurements of the hole diffusion length of 9 μm and a 180 ns minority hole lifetime at T = 80 K in bulk InAsSb alloy absorbers with a 40 % Sb composition were reported. The Hall's data obtained for bulk InAsSb alloys with similar Sb compositions showed that the hole mobility continued to increase with temperatures beyond 120 K [44].

Although the barrier photodetector design enables to reduce the width of the depleted part of the absorber and to suppress the generation-recombination current originating from SRH recombination, respectively, thus, realizing low dark current diffusion-limited operation, the complexity of aligning barrier-absorber valence band positions and the doping in the barrier are two issues to resolve experimentally to reach the predicted device performance since the invention of the barrier heterostructure. [7,55,56] The former is owing to the limited knowledge of valence band bowing parameters in AsSb-based III-V ternary compounds, such as InAsSb,

GaAsSb and AlAsSb. The latter is attributed to the uncertainty of unintentionally doped carrier concentrations in the barriers with varied compositions. Our fitting of experimental current-voltage characteristics in a set of barrier detectors of various designs showed that a mixture of As-Sb alloys from group V inclined to p-type barrier, in contrast to Sb-based alloys exhibiting n-type residual background concentration of unintentionally doped barriers. It was reported that an n-type doping concentration of $1 \times 10^{16}\ cm^{-3}$ in the barrier can result in an increase of the turn-on bias by 0.1 V [56]. Both issues, the lack of data on the valence band bowing parameters of InAsSb and AlInGaSb alloys, and uncertainty of background concentration led to the difficulty of realization of the unimpeded minority hole transport across the barrier, and a high turn-on bias voltage of nBn heterostructure detectors. The data presented below summarize the experimental data on the turn on voltage in LWIR nBn detectors with bulk InAsSb absorbers and barriers of various compositions and doping levels. The analysis of experimental data was provided from the design perspective of LWIR detectors.

2.3.2 Description of heterostructures and experimental setup

The sample set consisted of five InAsSb/AlIn(Ga)AsSb/InAsb nBn heterostructures with 1-μm-thick $InAs_{0.6}Sb_{0.4}$ absorbers, 200-nm-thick undoped AlIn(Ga)AsSb barrier layers and heavily and moderately n-doped 200-nm-thick $InAs_{0.6}Sb_{0.4}$ top contacts. Heterostructures A, B, C, D had undoped $Al_{0.6}In_{0.4}As_{0.1}Sb_{0.9}$ barriers and different levels of electron concentration in the absorbers from unintentionally doped n-type background in structure A, to moderately tellurium doped (~10^{16} cm^{-3} level) in structure D. The background electron concentration in similarly grown undoped InAsSb was reported to be (1-3)x10^{15} cm^{-3}. Heterostructure E had undoped

$Al_{0.55}In_{0.4}Ga_{0.05}As_{0.09}Sb_{0.91}$ barrier and the absorber doped with tellurium to the level similar to that of structure B.

The nBn heterostructures were grown metamorphically on GaSb substrates by Molecular Beam Epitaxy (MBE). The lattice constant difference between GaSb substrate and the nBn heterostucture was accommodated by $Ga_{1-x}In_x$ Sb buffer with linear grading of In composition from 0% to 52%. The graded buffer was followed by a 500 nm thick $Ga_{0.65}In_{0.35}Sb$ virtual substrate with the lattice constant of 6.24 Å. The nBn heterostructures were grown lattice-matched to the virtual substrate. Thus, the absorber, the barrier and the top contacts were unstrained and unrelaxed. The details of the growth approach, XRD and TEM characterization were published earlier [25]. The band diagram of the nBn heterostructure is shown in Figure 2-13.

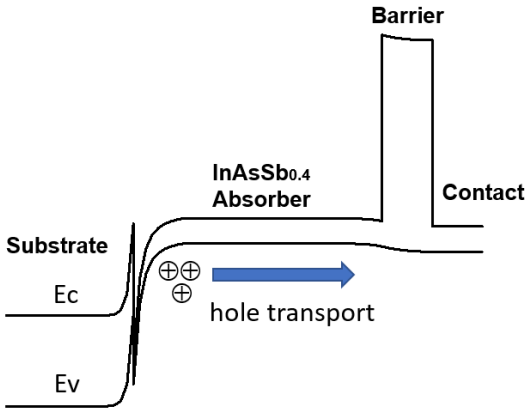

Figure 2- 13. Schematic band diagram of the nBn heterostructure with bulk InAsSb absorber in equilibrium.

Heterostructures A to D were intended for processing with illumination from the top contact side. In order to eliminate fundamental absorption in the top contact, the latter was heavily doped with tellurium to the level to 10^{18} cm^{-3} similarly to that reported in previous studies [6,57]. Heterostructure E was intended for processing with illumination from the

substrate side. The top contact was doped to a smaller level of $n=10^{17}$ cm^{-3} to decrease the required bias voltage. Summary of the heterostructure layers composition and doping is presented in Table.2-2.

Table 2- 2. Summary of the heterostructure layers composition and doping

Sample	**Barrier composition**	**Absorber doping (cm^{-3})**	**Contact doping (cm^{-3})**
A	$Al_{0.6}In_{0.4}As_{0.1}Sb_{0.9}$	undoped (low 10^{15})	1×10^{18}
B	$Al_{0.6}In_{0.4}As_{0.1}Sb_{0.9}$	low 10^{16}	1×10^{18}
C	$Al_{0.6}In_{0.4}As_{0.1}Sb_{0.9}$	medium 10^{16}	1×10^{18}
D	$Al_{0.6}In_{0.4}As_{0.1}Sb_{0.9}$	high 10^{16}	1×10^{18}
E	$Al_{0.55}In_{0.4}Ga_{0.05}As_{0.09}Sb_{0.91}$	low 10^{16}	1×10^{17}

Heterostructure A, B, C and D were processed as follows. The top contact mesa squares with a 500-μm side were etched in methane hydrogen reactive-ion inductively coupled plasma stopped at the barrier layer. The etched surface was passivated with a 300 nm thick silicon nitride. The windows in dielectric on the top of mesa were opened and a 100- μm wide ring TiPtAu contacts and side metal pads for wire bonding were formed by e-beam deposition and metal liftoff. No antireflection coating was deposited. The wafers were thinned to 170 μm by mechanical and chemical polishing then Ni/Au/Ge/Ni/Au metal contact was deposited to the substrate side and annealed at 250 ℃. Finally, Ti/PtAu metal was deposited on the substrate side. The wafers were cleaved into single chips. The devices were mounted with Indium on polished copper blocks and the top contacts were wire bonded to gold plated BeO stand-offs.

The dark current was characterized in a cryostat cooling down to liquid nitrogen temperature enclosed by a thermal-conductive copper foil. The QE spectra were measured by an FTIR spectrometer with the internal globar operating at the temperature of 1140℃ as the IR

source. The real QE values were corrected with account for the transparency of the cryostat's ZnSe window. No anti-reflection coating was deposited on the epi-side of the device. Thus, a considerable part of incident radiation was reflected from the heterostructure surface.

2.3.3 Experimental results and discussion

First, the bias dependence of quantum efficiency (QE) at 77 K will be discussed for heterostructures B and E which had similar doping level of the absorber and different barrier compositions. Second, the bias dependences of QE will be presented for four heterostructures, A, B, C, D, which had similar barrier design and different doping levels in the absorber.

In heterostructure A-D, the barrier layers had AlInAsSb and in heterostructure E the barrier was AlInGaAsSb quinary compound. The substrate was grounded. The negative voltage was applied to the top contact to eliminate the potential barrier for minority hole transport from the absorber to the top contact. The absorbers of both B and E heterostructures were n-doped with tellurium to the level of $1 \times 10^{16}\ cm^{-3}$. For this doping level in the absorber the hole diffusion length of 9 μm and hole mobility of 1000 cm^2/Vs were reported [6]. The normalized QE of heterostructures B and E are shown in Figure 2-14(a). For analysis of the bias dependences, we considered two bias voltage parameters: the initial bias voltage where the QE starts to increase and the saturation voltage where QE saturates to a constant level. In Figure 2-14(a), one can see that these bias parameters are different for heterostructures B and E which are attributed to differences in the valence band alignment between the absorber and the barrier, as well as different levels of n-doping in the top contact layers. The device with quaternary barrier and $1 \times 10^{18}\ cm^{-3}$ n-type doping in the top contact had a fast increase of slope from -0.2 V to -0.35 V, and reached saturation at -0.4 V. On the other hand, the device with quinary barrier and

less Te-doping of $1 \times 10^{17}\ cm^{-3}$ in the top contact showed an increase in the range of -0.05 V to -0.15 V and saturated at -0.15 V. The decrease of doping from $1 \times 10^{18}\ cm^{-3}$ to $1 \times 10^{17}\ cm^{-3}$ in the contact resulted in a significant bias reduction of 0.1 V to be applied. The remaining reduction of 0.15 V was an outcome of better valence band alignment between the absorber and the barrier.

The QE data below are presented for heterostructures A to E. Using the reported hole mobility and the minority hole lifetime data for heterostructures B and C in Figure 2-14(b), we concluded that the hole diffusion length was significantly longer than the absorber thickness. Thus, in the heterostructures with different levels of absorber doping, the major part of minority holes were able to reach the top contact.

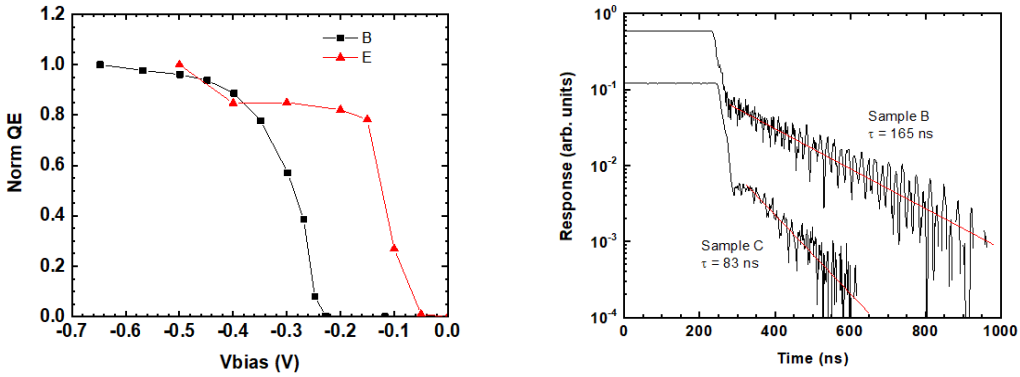

Figure 2- 14. (a) The normalized dependences of the quantum efficiency on bias voltages for heterostructures B and E. (b) Minority hole lifetime measurement by transient response to a pulsed laser excitation in structure B and C with low doping and medium doping. Structure C with higher doping significantly reduces the lifetime from 165 ns to 83 ns.

The QE spectra as a function of doping and temperature in structure set A-D were illustrated separately in Figure 2-15 (a) and (b). As estimated from QE edges, the quasi-Fermi level for electrons above the conduction band for structure A-D were 0 meV, 16 meV, 32 meV, and 46 meV, respectively. The doping concentrations were calculated as a function of Fermi level accounting for the nonparabolicity of the conduction band and the electron effective mass

of 0.011 m_0 concluded by magnetotransport measurements [58]. The corresponding doping levels for structure A-D were derived to be $3.8x10^{15}$ cm^{-3}, $1.7x10^{16}$ cm^{-3}, $4.7x10^{16}$ cm^{-3}, $8.6x10^{16}$ cm^{-3}.

The doping dependence of the QE was measured at 77 K. Increase the doping levels led to a blue shift of cut-off wavelength from LWIR region into MWIR. The cut-off wavelength taken at -3dB for the undoped sample was 7 μm, and QE of 10 % was retained at the longer wavelength of 8.6 μm. By increasing the doping from undoped to highly doped, the overall intensity of the QE spectra was lowered by 20 %.

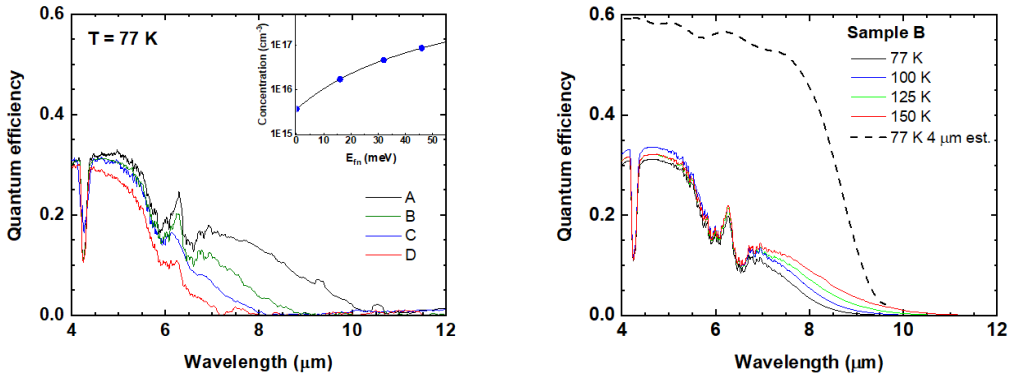

Figure 2- 15. (a) QE spectra of a set of heterostructures at a constant temperature of 77 K for difference doping concentrations. Inset shows electron concentrations depending on the quasi-Fermi energy level of electrons. (b) QE spectra of the heterostructure B at different temperatures. Dashed line shows an estimation of full photon absorption simulated in 4-μm absorber. The max QE reached 60 % in mid-wave infrared region without AR coating.

The temperature dependence of QE was measured in the device with an absorber doping of $1.7 \times 10^{16}\ cm^{-3}$ in structure B. A red shift with cut-off wavelength was shown in Figure 2-15(b) at elevated temperatures, indicating a decrease of the band gap energy at higher temperatures. The magnitude of QE in the spectral range of a complete light absorption (λ =5 μm) was improved upon increasing the temperature from 77 K to 100 K, which demonstrated the enhancement of hole mobility proportional to the thermal energy. At higher temperatures, the QE at 5 μm experienced a moderate drop from 100 K to 125 K. The photodetector operating at high

temperature of 150 K exhibited a 31 % QE at 5 μm and 9 % QE at 8 μm despite of a 33 % reflection of the incident photon flux at the air-epilayer interface.

In heterostructure E, a 10 % QE was measured at 7.8 μm. The transmittance and reflectance of the heterostructure detector were estimated by a two-layer stack model [59] using the experimental absorption spectrum of $InAs_{0.6}Sb_{0.4}$ [51]. The maximum external QE was calculated to be 39.0% at 4 μm and 30.4% at 5 μm. Due to the strong fundamental absorption of 7840 cm^{-1} at the wavelength of 4 μm in InAsSb and a long diffusion length of 9 μm [46], nearly all the carriers generated in the absorber were collected by the top contact. In addition to that, the QE intensity calibrated by experiment in structure B with 1- μm absorber agreed the max QE estimated by the model. Bias-dependent dark current densities for heterostructures A-E at T = 80 K are presented in Figure 2-16(a).

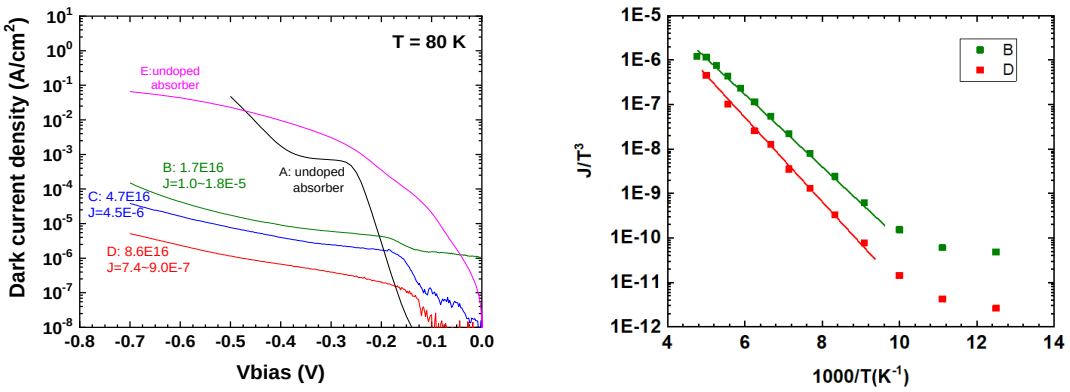

Figure 2- 16. (a) Bias dependent dark current density at 80 K for structure A-D with different doping levels. Structure A with undoped absorber shows a noticeable higher dark current density compared to the other n-doped structures. (b) Arrhenius plot of barrier heterostructure as a function of reciprocal temperature for low doped and highly doped structures. A greater slope in structure D indicated a higher thermal activation energy, in accordance with the doping level's impact on the electron quasi Fermi level.

From the undoped sample to those with doping levels from $1.7x10^{16}$ cm^{-3} to $8.6x10^{16}$ cm^{-3}, the dark current densities at the bias voltage of -0.4 V were approximately 10^{-3}, 10^{-5}, 10^{-6}, 10^{-7} A/cm^2, respectively. Decrease of the dark current at elevated doping levels was attributed to a

smaller minority hole concentration. The I-V curve for the undoped absorber consisted of three stages distinguished by different slopes. The initial rapid increase of the current was interpreted as lifting the valence band energy upwards in the heavily doped contact layer. Holes in the absorber set forth the carrier flow towards the top contact. The following plateau phase was the saturation operating point defined by the QE value. In the plateau, all holes generated in the absorber reached the contact layer by diffusion. A further increase of the slope with bias was attributed to extension of the depletion region at the absorber-barrier interface region. The latter resulted in a rapid increase with bias of the contribution of the thermal generation of hole in the depletion region. The I-V curves for the doped samples, shown as olive green, blue and red in Figure 2-16(a), mainly consisted of the first two stages of the slopes discussed above. This is because the n-type doping in the absorbers led to a reduction of the width of unwanted depletion region need the barrier layer. A greater current in structure E can be attributed to the higher thermal generation current due to higher concentration of defects originated from a less optimal design of the graded GaInSb buffer. Despite the higher dark current, the lower operating bias of -0.15 V could keep its magnitude at a level of 10^{-4} A/cm^2.

The temperature-dependent dark current densities in the Arrhenius plot shown in Figure 2-16(b) for heterostructures B and D demonstrated a diffusion-limited behavior of the dark current at temperatures above 100 K. The thermal activation energies in structure B and D were estimated to be 160 meV and 180 meV by fitting the J/T^3 versus reciprocal temperature. These two energies were slightly higher than the values calculated from QE edge discussed above, by band-filling of electrons above the conduction band.

2.3.4 Analysis of band alignment by drift-diffusion model

Modeling of the I-V characteristics of nBn heterostructure was performed to explore how the doping and valence band alignment at the absorber-barrier interface can affect the QE turn-on voltage. The modeling parameters including mobility, effective mass, and doping concentration were cited from previous designs as well as from this work [6,7,58]. The modeled structure was composed of four layers, including n+ GaSb substrate, n-type InAsSb absorber, undoped barrier, and n+ top contact. The layer thicknesses were 0.5 μm, 1 μm, 0.2 μm, and 0.2 μm, respectively. The minority carrier lifetime was set to be limited by Auger recombination with $C_n = 1 \times 10^{-25}\ cm^6/s$. According Vurgaftmann et al. [17], the valence band and conduction band energies of III-V binary materials were set initially without applying any bowing. In the next step, a total bowing of the energy band gap, if specified in the Ref [17], was applied to each ternary material accounting for the curvature of the band gap. Finally, a split of bandgap bowing into conduction band bowing Cc and valence band bowing Cv was used to determine the absolute energy level of the conduction and valence bands. In other word, the valence band potentials in epilayers were adopted by applying additional bowing parameters based on the originally proposed energies by Vurgaftmann et al. The band gap bowing parameter for $InAs_{1-x}Sb_x$ was taken to be 0.87 [26] determined by helium temperature PL maxima, from which 0.3 eV or 0.4 eV was assigned to the valence band bowing. Same Cv bowing was applied to $AlAs_{1-x}Sb_x$ and $GaAs_{1-x}Sb_x$.

In order to justify the impact of valence band offset (VBO), the initial case was proposed to be a heterostructure with a zero VBO and an undoped barrier. The estimated concentration of the undoped barrier was n-type $3 \times 10^{15}\ cm^{-3}$. Variation of VBO was applied thereafter in the barrier from -30 meV to 30 meV with a step of 15 meV. The I-V characteristics were illustrated

in Figure 2-17 (a), where the negative sign of VBO energy denoted the case with a higher valence band energy in the barrier layer. In such case, the diffusion of minority hole carriers was impeded by the VBO misalignment at the absorber-barrier interface. A better hole transport could be realized by lowering the valence band energy for holes in the barrier. The later increase of the valence band energy in the barrier has to be a small fraction of the energy gap in order to avoid the interband tunneling of electrons to the absorber. The common saturation level of all current densities with different VBOs indicated an exhausted supply of the holes under a large enough reversed bias. For each VBO, the barrier doping levels of n-type $3 \times 10^{15}\ cm^{-3}$, $1 \times 10^{16}\ cm^{-3}$, $2 \times 10^{16}\ cm^{-3}$were considered.

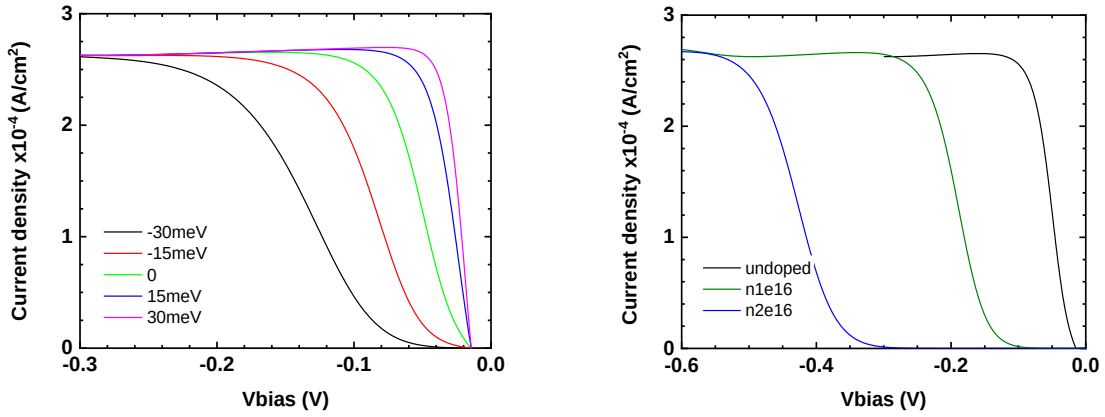

Figure 2- 17. (a) I-V characteristics based on different valence band offset and undoped barrier. (b) I-V characteristics based on different n-type doping levels and zero valence band offset. The main discrepancy of the impediment created by the barrier doping and the VBO can be identified with the help of the initial bias.

Figure 2-17 (b) shows dark current densities with a zero valence band offset for different barrier doping levels. It was noted that an n-doped barrier creates an impediment to the hole transport. The discrepancy of the impediments created by doping and by VBO can be identified with the initial bias where the current starts to increase. The signal onsets at a higher bias in the structures with greater n-doping level in the barriers were observed. For example, the doping

level of $2 \times 10^{16}\ cm^{-3}$ resulted in an initial bias of -0.28 V. In contrast, all the samples with undoped barriers had near-zero initial bias regardless of the VBO.

To testify the accuracy of the modeling, the starting bias V_{ST} and saturation bias V_{SA}, defined as 10% and 90% of the full scale of the current density, were compared with the experimental results. The VBO and doping dependence of the saturation voltages were mapped in Figure 2-18, where the smallest turn-on bias as low as 38 mV locates at the corner of positive VBO and undoped absorber. On the contrary, a large negative VBO and greater n-type doping results in an increase of bias by 17 times.

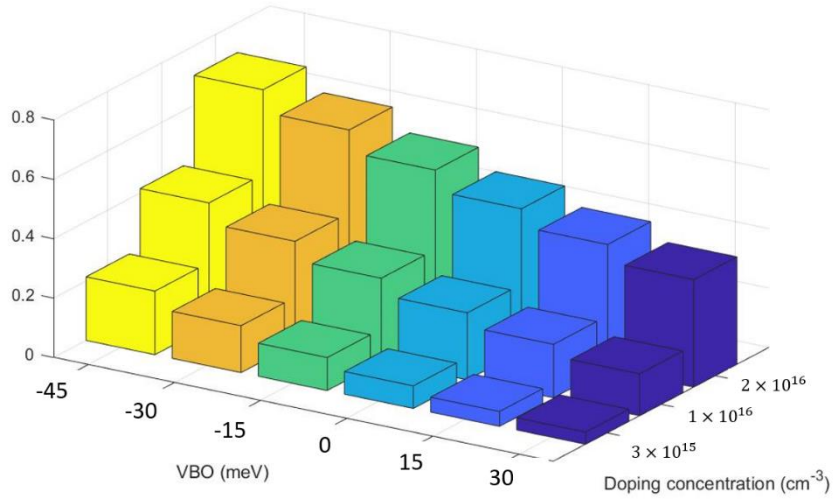

Figure 2- 18. 3D bar graph modeling, showing the x-axis as valence band offset, the y-axis as doping concentration and the z-axis as VST in the nbn barrier heterostructure. For higher doping concentrations and large negative valence band offsets, the Vst reached a maximum bias of 0.7 V which is shown by the yellow bar. For low doping concentrations and positive valence band offsets, the Vst reached a minimum of 0.041 V which is shown by the dark blue bar. Absolute values of bias are taken in the plot.

Several works have been discussed the value of the VB bowing parameter which was considered to be in the range of 0.3 to 0.4 eV [6,7] and summarized in Table 2-3 with a valence band bowing of C_V = 0.3 eV and Table 2-4 with a valence band bowing of C_V = 0.4 eV. For comparison, the valence band energy levels were estimated for the case without the valence band

bowing. All the estimations with zero valence band bowing presented lower valence band energies in the barrier as noted by the positive sign convention, ranging from +29 meV to +56 meV. If this were the case, no impediment is supposed to appear for hole transport. However, the measured turn-on bias opposed to this assumption but rather manifest a valence band bowing of C_V = 0.3-0.4 eV. For example, with zero C_V assumption, the worst case would be V_{SA} = -0.2 V as shown in Figure 2-17(b) for zero VBO and n-type $1 \times 10^{16}\ cm^{-3}$, but experimental data demonstrated the saturation bias is above -0.3 V in most cases, which indicated the existence of unwanted band misalignment between the absorber and the barrier.

Table 2- 3. Summary of barrier composition, barrier concentration, contact doping, valence band bowing used to fit the operating voltages in PADRE simulation. A valence band bowing of 0.3 was applied.

Ref	Barrier composition	Barrier dopant concentration in MBE (cm^{-3})	Modeled barrier concentration (cm^{-3})	Contact doping (cm^{-3})	VBO C_V=0.3 eV	V_{ST} (V) Mod vs Ex	V_{SA} (V) Mod vs Ex
1 [7]	$Al_{0.75}In_{0.25}Sb$	$p = 1 \times 10^{16}$	$n = 1.1 \times 10^{16}$	1×10^{18}	-26 meV	0.33 0.34	0.44 0.42
2 [6]	$Al_{0.6}In_{0.4}As_{0.1}Sb_{0.9}$	undoped	$n = 1 \times 10^{16}$	1×10^{18}	-16 meV	0.27 0.25	0.37 0.38
3 [7]	$Al_{0.75}In_{0.25}Sb$	undoped	$n = 2.2 \times 10^{16}$	1×10^{18}	-26 meV	0.60 0.61	0.75 0.87
4 .Struct. E	$Al_{0.55}In_{0.4}Ga_{0.05}As_{0.09}Sb_{0.91}$	undoped	$n = 8 \times 10^{15}$	1×10^{17}	+7 meV	0.06 0.05	0.13 0.15

Table 2- 4. Summary of barrier composition, barrier concentration, contact doping, valence band bowing used to fit the operating voltages in PADRE simulation. A valence band bowing of 0.4 was applied.

Ref	Barrier composition	Barrier dopant concentration in MBE (cm^{-3})	Modeled barrier concentration (cm^{-3})	Contact doping (cm^{-3})	VBO C_V=0.4 eV	V_{ST} (V) Mod vs Ex	V_{SA} (V) Mod vs Ex
1. [7]	$Al_{0.75}In_{0.25}Sb$	$p = 1 \times 10^{16}$	$n = 8 \times 10^{15}$	1×10^{18}	-50 meV	0.34 0.34	0.46 0.42
2. [6]	$Al_{0.6}In_{0.4}As_{0.1}Sb_{0.9}$	undoped	$n = 8 \times 10^{15}$	1×10^{18}	-31 meV	0.27 0.25	0.38 0.38
3. [7]	$Al_{0.75}In_{0.25}Sb$	undoped	$n = 1.8 \times 10^{16}$	1×10^{18}	-50 meV	0.62 0.61	0.75 0.87
4. Struct. E	$Al_{0.55}In_{0.4}Ga_{0.05}As_{0.09}Sb_{0.91}$	undoped	$n = 6 \times 10^{15}$	1×10^{17}	-7 meV	0.05 0.05	0.13 0.15

Comparing Cv = 0.3 eV with 0.4 eV, a higher native n-type barrier concentration in the range of $8x10^{15}$ to $2.2x10^{16}$ cm^{-3} was required in modeling to fit the operating voltages. We concluded that a 0.4 eV valence band bowing parameter provides a better agreement of the modeled and experimental data. The same value of the VB bowing parameter was obtained from the first principles by Bellotti et al.

From comparison of cases 1 and 2 in Tables 2-3 and 2-4 it was noticed that the barriers with As provide both a lower valence band energy due to the valence band bowing and additional acceptors compensating the n-type background concentration As estimated by band-filling effect, an increment of contact doping level from $1 \times 10^{17}\ cm^{-3}$to $1 \times 10^{18}\ cm^{-3}$, or to $1 \times 10^{19}\ cm^{-3}$ can lead to an additional increments of bias of 140 mV and 342 mV, respectively. A lower bias voltage can be also attributed to growth of barriers on the top of absorbers without growth interruption.

2.3.5 Specific Detectivity and performance evaluated by Rule07

The energy band gap of InAsSb absorbers with nominal 40 % of Sb was estimated to be 130 meV at T =77 K [5,6]. To identify the performance of the photodetector, the specific detectivity D^* spectra were calculated from QE spectra and the dark current density. The following equation was applied, where the thermal noise and shot noise signal were involved:

$$D^* = \frac{nqhv}{\sqrt{(2qJ + 4kBT/RA)}} \tag{2.3}$$

where η is the dispersive quantum efficiency, and hv is the photon energy. The resistance-area product can be derived by differentiating the current density over operating bias at -0.4 V. The doping-dependent peak detectivity shown in Figure 2-19 (a) appeared in the region of 4 to 5 μm. The maximum detectivity of $2.\times 10^{12}\ cmHz^{1/2}/W$ occurred in the device with high $10^{16}\ cm^{-3}$

doping level since the dark current density was greatly suppressed by increasing the dopant. On the other hand, the temperature-dependent detectivity spectra are shown in Figure 2-19 (b) with peak magnitudes in the same wavelength range. A decreasing trend of detectivities as increasing temperature was observed, where the peak detectivity $6 \times 10^{11}\ cmHz^{1/2}/W$ at 77 K dropped down to $7.4 \times 10^{9}\ cmHz^{1/2}/W$ at 150 K. The detectivity spectra also implied a D* of $3 \times 10^{11}\ cmHz^{1/2}/W$ can be achieved at the LWIR wavelength of 9 μm.

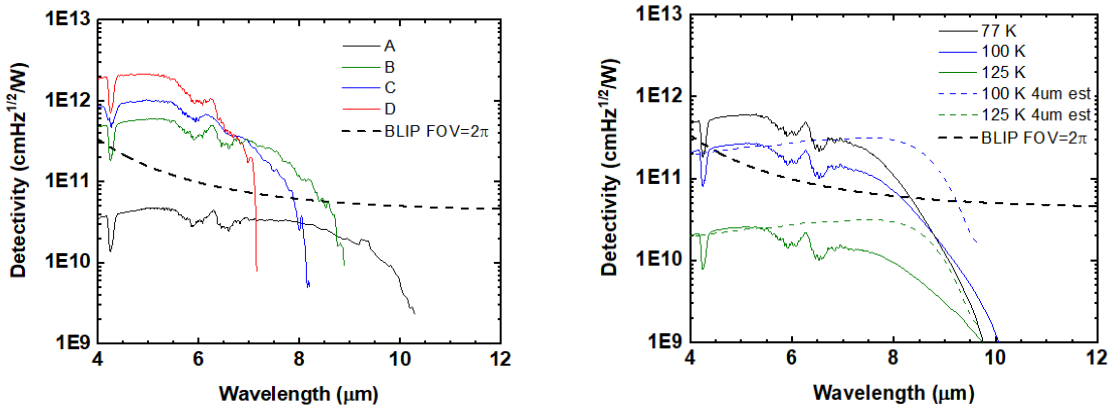

Figure 2- 19. (a) Detectivity spectra depending on different doping levels. Performance better than room-temperature background limited infrared performance (BLIP) in a solid angle of 2π is achievable in the mid-wave infrared region in structure B-D. (b) Detectivity spectra depending on temperatures from 77 – 125 K. Performance better than BLIP is possible at 77 -100 K. Modeling indicated a better detectivity at LWIR region could be realized in a thicker 4-μm absorber.

The performance of photodetectors in this section was evaluated by "Rule 07", which was proposed by Tennant [19,20] as a criterion for the state-of-the-art *pn* HgCdTe photodiodes. As seen in Figure 2-20, the photodetector performance at the temperature of 77 K is not comparable to that of MCT detectors. Heterostructure E with the smallest turn-on bias operating at 77 K showed a comparable cut-off wavelength-temperature product to structure B operating at 100 K. Also heterostructure E showed 4 orders of magnitudes greater dark current compared to Rule07 asymptotic. The overall best sample is structure B working at 150 K, indicating a competitive high-temperature performance with 2 magnitudes (60 times) greater dark current

density than Rule07. If the comparison were extended to the existing state-of-the-art InAs/InSb based detectors implemented with nBn heterostructures, our best photodetector still has very competitive performance, served as a high temperature operating photodetector with the cutoff wavelength at 7 μm.

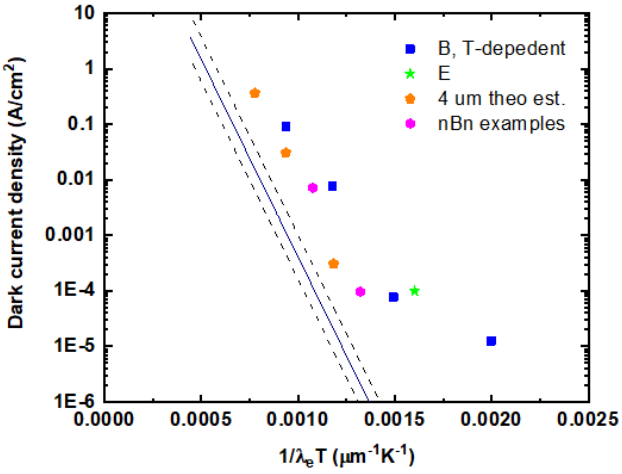

Figure 2- 20. Photodetector performance regulated by "Rule 07" in straight line, while the two dashed lines are speculated with 0.4x to 2.5x deviation. According to the reference, it is still in the best performance range. The magenta point shows two nBn examples for comparison [60,61].

To the best of our knowledge, we theoretically estimated the performance for photodetectors with a 4-μm-thick absorber. The external QE spectra was derived from the measured absorption spectra in undoped $InAs_{0.6}Sb_{0.4}$ absorber and double-path absorption was considered within the absorber. A variation of temperature-dependent band gaps was adjusted by fitting the QE edges. Only estimation above 100 K was given due to the feasibility of scaling the diffusion-limited current by a factor of 4 when increasing the absorber from 1 μm to 4 μm. In Figure 2-20, the orange scattered points representing the photodetector with a 4 μm absorber are way closer to Rule07, but it cannot exceed the performance of HgCdTe photodetectors.

2.3.6 Conclusion

In Section 2.3, nBn heterostructure photodetectors with 0.13 eV energy gap InAsSb bulk absorbers were studied with a variety of the absorber doping concentrations, the contact layer doping concentrations and the barrier compositions. The dark current as low as 10^{-6} A/cm^2 at T = 80 K and the diffusion limited behavior above T = 100 K were observed. The maximum QE of 35 % was consistent with the absorber thickness and implied a lower limit of the minority hole diffusion length of 2 μm at temperatures as high as 150 K and high absorber doping level to 8.6×10^{16} cm^{-3}. The best fitting of the QE versus bias voltage of barrier heterostructures was obtained with the valence band bowing parameter of 0.4 eV. It was concluded that a 9 μm cut-off wavelength and BLIP at 100 K can be theoretically achieved with growth of the devices with 4-μm-thick InAsSb absorbers.

2.4 Summary

In this chapter, type-II superlattice InAsSb and bulk InAsSb absorbers are used in the barrier heterostructure for photon detection operating at long-wave infrared region. InAs/$InAs_{1-x}Sb_x$ SLS was grown latticed matched to GaSb substrate, while $InAs_{1-x}Sb_x$/$InAs_{1-y}Sb_y$ SLS and bulk $InAs_{1-x}Sb_x$ were grown on the virtual substrate on the metamorphic buffer. Vertical hole transport and minority hole lifetime were explored in T2SL with a bandgap of λ= 10 μm. $InAs_{1-x}Sb_x$/$InAs_{1-y}Sb_y$ SLS with a shorter superlattice period and wider valence band miniband showed at least two times greater hole lifetime and vertical hole mobility compared to InAs/$InAs_{1-x}Sb_x$ SLS at temperatures from 77 K to 150 K. A longer diffusion length in the short-period structure resulted in an enhancement of quantum efficiency from 40 % to 63 %.

A set of barrier heterostructures with bulk InAsSb absorbers for LWIR responsivity were grown by MBE. Bulk absorbers of $InAs_{1-x}Sb_x$ with 40 % Sb were used and its energy band gap was 130 meV. Variation of absorber doping concentration, barrier composition and contact doping were extensively investigated in terms of temperature dependence, I-V characteristics, minority hole lifetime, and detector response. A balancing between the penalty to the cut-off wavelength and the suppression of dark current with n-type absorber doping can be satisfied at the doping level of $1x10^{16}$ cm^{-3}. At higher operating temperatures up to 150 K, the device operation was demonstrated with a such doping level, and the performance of the devices with InAsSb absorbers was closer to Rule07. Using simulation data obtained with PADRE, the valence band bowing parameter of 0.4 eV for InAsSb alloys was found to be appropriate and recommended for heterostructure design. In order to achieve a smaller turn-on bias and a better hole transport, it was concluded that an intentional p-type doping of the barrier layer in nBn heterostructures is demanded for compensation of native n-type background concentration in the barrier, especially in the barrier compositions without As.

Chapter 3 InAsSb-based barrier heterostructures for beam steering and modulation

3.1 Introduction

Free-space amplitude modulator and phase modulator are essential parts in optical systems for beam shaping, wavefront correction, and beam steering. They have a wide application in Laser scanner, pulsed Laser source (Q-switching and mode locking), LiDAR and telecommunication. Beam modulations are commonly realized by electro-optic (EO) effect or acousto-optical (AO) effect to induce the change of refractive indices. In optical phased arrays (OPA), thermal-optical effect is mainly used to achieve phase shift in the waveguide for azimuthal and vertical steering [62]. Those using electro-optical effects of Pockels or Kerr types require high voltage drivers. For nanosecond response, the drivers have to output high current [63] due to high cell capacitances. The steering angle obtained with EO devices are small. For example, the electro-optical deflector (EOD) requires hundred volts for the beam deflection of $\pm 0.1°$ [64]. Unlike fiber-coupled modulators supporting high-speed modulation at GHz range [63,65–68] with a single-digit half-wave voltage, free-space modulators need kilovolt driven voltage with slow response at the modulation frequency from a few hundred kHz to a few hundred MHz [63,69,70]. Typical EO materials available at LWIR include GaAs, CdTe, ZnSe and ZnTe [71–73]. Compared to the most popular EO material - lithium niobate (LN) with a cut-off wavelength at 5 μm [68,74–76], these materials have one magnitude less electro-optical coefficients at the wavelength of 10.6 μm [77]. The change of refractive index in these EO materials is in the order of $10^{-5} – 10^{-6}$.

The speed of AO modulator is determined by the acoustic wave velocity. Modulation controlled by acoustic wave is of at least one magnitude slower speed than EO materials and lack

of high-precision manipulation in beam steering. Fast-response modulators operating at long-wave infrared (LWIR) are in demand for numerous gas and solid-state laser sources, such as CdTe, GaAs-based modulators for 10.6 μm CO_2 lasers [78-79] and Quantum Cascade Lasers (QCL) operating in the wavelength range up to 16 μm [80-81]. Modulation of intensity and beam deflection was realized by a change of free carrier absorption in GaAs waveguide heterostructure [82], and the response time was a few ns working at 10.6 μm.

In the chapter, a new approach for beam intensity and phase modulation is demonstrated by manipulation of fundamental absorption in InAsSb-based heterostructures. The fundamental absorption is significantly stronger compared to free carrier absorption. Therefore, the change of refractive index is orders of magnitude greater than those conventional EO materials. Change of refractive index was realized by carrier injection to populate the states above the conduction band based on Burstein-Moss shift [83–85]. Excess carriers were injected in nBp heterostructure under forward bias, where holes and electrons were injected from p side and n side separately due to the unipolar transport property of nBp structure. Again, bulk $InAs_{0.58}Sb_{0.42}$ and $InAs_{0.65}Sb_{0.35}/InAs_{0.35}Sb_{0.65}$ strained layer superlattices were adopted as the active region of the barrier heterostructure. The intensity modulation depths of up to 9 % were demonstrated in bulk InAsSb with 8.6 μm QCL and in type-II InAsSb-based SLS with 10.6 μm CO_2 laser. Modeling of transmittance in a thin film multiplayer stack [59] had an agreement with the experimental results of the modulation depth. A 2 ns time response of intensity modulation was demonstrated with a pulsed current injection. We also explored the refractive index change in the vicinity of the absorption edge using Kramers-Kronig relations and theoretically estimated the index changes up to 0.06 and 0.05 at T = 77 K in bulk InAsSb and type-II InAsSb-based SLS, respectively. It enlightened us to apply this phenomenon in design of beam steering devices

based on Optical Phased Arrays (OPA), Fabry-Perot etalons or Mach-Zehnder interferometers (MZI) which operations are based on the carrier-induced refractive index change.

3.2 Beam intensity modulation in bulk InAsSb

3.2.1 Heterostructures and experimental setups

Unstrained bulk InAsSb active regions were grown with a 42 % Sb composition by solid-source molecular beam epitaxy on GaInSb virtual substrate grown metamorphically on GaSb. As mentioned in Chapter 2, the strain mismatch between the virtual substrate and GaSb was accommodated with a 2 μm thick compositionally graded GaInSb buffer. The topmost portion of the buffer layer was unrelaxed and under compressive strain.

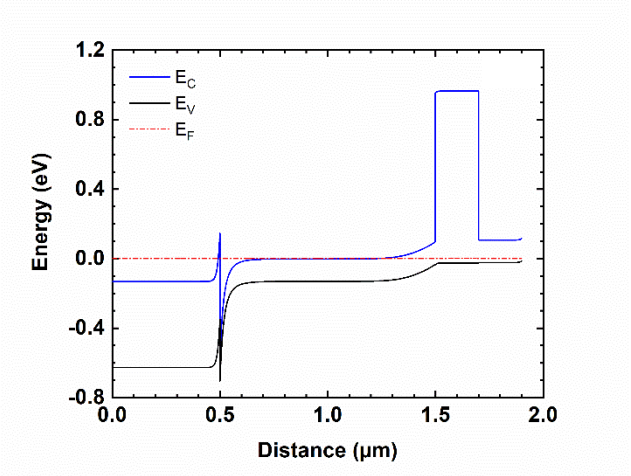

Figure 3- 1. Energy band diagram of the nBp heterostructure for beam modulation in equilibrium.

The undoped 1-μm InAsSb absorber was grown lattice matched to $Ga_{0.64}In_{0.36}Sb$ virtual substrate. The virtual substrate had a lattice constant of 6.25 Å at 77 K. The absorber was followed by a 200 nm $Al_{0.35}In_{0.65}As_{0.284}Sb_{0.716}$ barrier doped with Be to a level of 10^{17} cm^{-3} followed by a 200 nm thick p-doped $InAs_{0.58}Sb_{0.42}$. The heterostructure formed a nBp device as shown in Figure 3-1. This barrier heterostructure provided good carrier confinement for both

electrons and holes in the active region injected from n- and p-sides, respectively. The energy gap of the active region was determined to be 133 meV at 77 K.

The processing of the heterostructures into modulators was as follows: the mesa with a dimension of 300 x 300 μm^2 was defined by reactive ion etching. It was metalized leaving a window of 250 x 250 μm^2 for optical transmission. The mesa was coated with a 200-nm SiN dielectric layer for sidewall passivation. The substrate side had an open window of 300 x 300 μm^2 aligned with the epi-side window done by dual-side mask aligner. Ti/Pt/Au metal alloy was deposited on p-side (or frontside). Ni/Au/Ge/Ni/Au followed by Ti/Pt/Au was used on n side (or substrate side). The metal annealing was conducted by rapid thermal processing to achieve an ohmic contact on the n-side with low resistance. The schematic of the side-view of the device and an example of modulator arrays are shown in Figure 3-2.

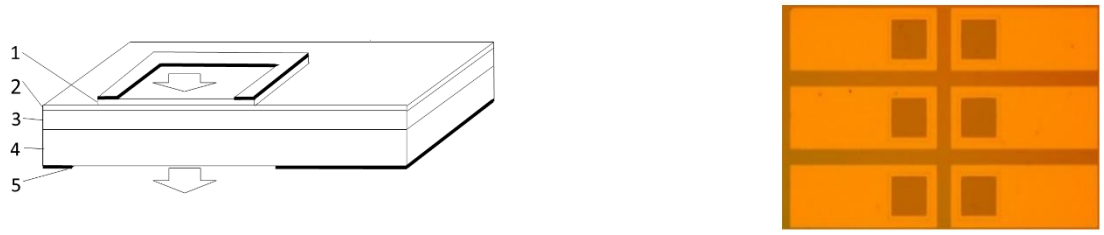

Figure 3- 2. (a) Cross-section of the mesa, 1-5 refer to contact layer, barrier, active region, substrate and n-side contact. (b) Epi-side view of the modulator arrays. Square represented open window for optical transmission. Light orange rectangle refers to metal pad for wire bonding.

The beam intensity modulation measurements were composed of two parts: modulation spectra with a large duty cycle current injection were measured by Nicolet FTIR spectrometer and modulation depth by a short-pulse current injection was determined with a CW-mode 8.6 μm QCL. With the FTIR spectrometer working in the step-scan mode, the electrical modulation of transmission spectra was measured with an internal globar IR source and a HgCdTe detector with cutoff wavelength at 14 μm. The injection of current into the heterostructure was in the

range of 20 – 500 mA. The current was injected into the active region of the heterostructure with a 1-μs-wide pulse with a 100 kHz repetition rate (a duty cycle of 10 %). The modulation depth of the intensity of QCL was measured with 100 ns pulse width and 10 kHz repetition rate equivalent to 0.1 % duty cycle. The QCL was ran in continuous-wave mode. The transmitted light was detected with a fast response HgCdTe photodiode with a cut-off wavelength of 12 μm used with a preamplifier. The bandwidth of the pre-amp is 80 MHz at -3 dB. The beam propagated through the modulator in a single path transmission configuration. The modulation of the transmitted light was observed with a scope for data acquisition in a PC.

The modulation depth was defined as $M = \frac{\Delta I}{I_0}$, where M was the modulation depth, ΔI was the change of the transmitted signal due to Burstein-Moss shift, I_0 was the signal without carrier injection.

3.2.2 Results and analysis

The modulation of transmission spectra is shown in Figure 3-3 (a). As we can see, the transmission spectra were measured at photon energies from 0.05 eV up to 0.25 eV with a peak modulation at 0.14-0.15 eV. Three levels of current injection were characterized under 20 mA, 100 mA and 500 mA. No change of transmitted signal was observed in the spectra with the blocked globar IR source. Thus, the transmission modulation can be completely attributed to the modulation arising in the InAsSb heterostructure. The increase of current injection level enhanced the modulation level proportionally under low excitation levels. A saturation of modulation depth was observed under the current level of 1 A (Figure 3-3b). Under a short-pulse low duty cycle current injection, the Joule heating of the device was negligible. The maximum modulation depth of 9 % was observed. Analysis showed that the saturation of the modulation

depth corresponded to a complete population of electrons in the conduction band at the energy defined by the difference of the photon energy and the energy gap. The modulation depth was consistent with expectation from the 1-μm absorber with the absorption coefficient of 800 cm^{-1} at Eph = 144 meV. For further increase the modulation depth, a stronger absorption or a thicker active region would be required.

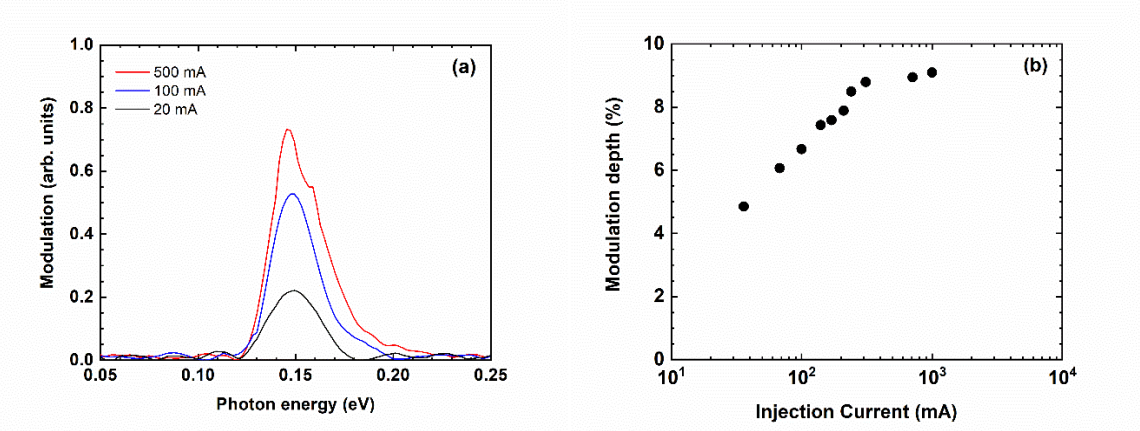

Figure 3- 3. (a) Modulation of transmission spectra measured under current levels of 20 mA, 100 mA and 500 mA at 77 K. Modulation occurred at photon energies from 0.12 eV to 0.20 eV with a peak at 0.14 – 0.15 eV. (b) Modulation depth was characterized with CW 8.6-μm QCL an [59]d a saturation of modulation was found to be 9 % under 1 A current injection.

The transmission spectra of the heterostructure under current injection were modeled using a thin film multilayer stack method. The experimentally determined absorption spectra and free carrier absorption in the substrate were considered. The real parts of the refractive indices of all layers except the absorber were taken to be constant. The modeled transmission spectra are illustrated in Figure 3-4 (a). The spectra were estimated with the elevations of the quasi-Fermi level by 10 meV, 15 meV, 20 meV and 30 meV. In a previous work, it was found that the electron Fermi level in an undoped InAsSb under the equilibrium condition is aligned with the bottom edge of the conduction band [44]. Therefore, with current injection a lift of the electron quasi Fermi level occurred above the bottom of the conduction band. Among these, the spectrum with a rise of E_F = 20 meV closely resembled the energy peak as well as extension of the

transmission spectra to higher photon energies observed experimentally with FTIR. Our estimates showed that the quasi Fermi level of 20 meV corresponded to an excess carrier concentration of $2x10^{16}$ cm^{-3} at 77 K, estimated by an integral of the density of state with consideration of the nonparabolicity of the conduction band and Fermi distribution. The effective mass for electrons of 0.01 was obtained from Ref. [58]. The maximum modulation depth in the heterostructure obtained by modeling was 8 % at Eph = 144 meV, which fairly agreed with the value of 9 % obtained with a short-pulse current injection measurement. Modeling showed that with the active region thickness increase from 1 μm up to 4 μm, the maximum modulation depth based on fully population of states can reach 39 % as shown in Figure 3-4 (b).

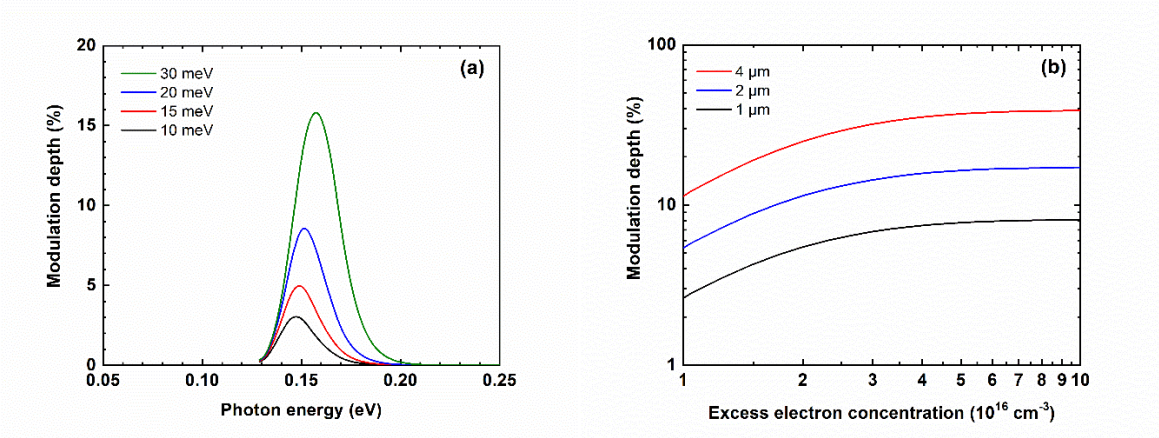

Figure 3- 4. (a) Modelled modulation of transmission spectra at quasi Fermi level of 10, 15, 20 and 30 meV above the conduction band. (b) Modulation depth as a function of excess carrier concentration depending on active region layer thickness. A thickness of 4 μm was projected to serve a modulation depth of 39 %.

Based on the excess carrier concentration of $2x10^{16}$ cm^{-3} and the injection current I = 40 mA under the same modulation depth of 5 %, equation $I = q\frac{n}{\tau}W$ was used to estimate the hole lifetime. The excess carrier lifetime was estimated to be 10 ns. For that estimate, the Auger coefficient limiting the excess carrier concentration for a given current was derived by $Cn+Cp = 1/\tau n_e^2 = 2x10^{25}$ cm^6/s, where Cn >> Cp in n-type active region. The details can be found in Ref. [37].

The imaginary and real parts of the refractive index are one pair of parameters that meets the requirement of time-space causality. Therefore, one known parameter from either of these two can be used to unveil the other according to Kramers-Kronig Relations [86,87]. Owing to the strong fundamental absorption in InAsSb alloy, a small shift of the absorption edge due to carrier injection can lead to large change of the refractive index. This idea is illustrated in Figure 3-5 (a), where the absorption spectrum shifts due to quasi Fermi level rises of 0, 20, 30 meV were investigated. The maximum index change near the energy band gap of Eg = 133 meV was up to 0.06 with an electron quasi Fermi level of E_F = 30 meV above the bottom of the conduction band. This change of the refractive index is at least one order of magnitude greater than those in most EO materials operating in LWIR region.

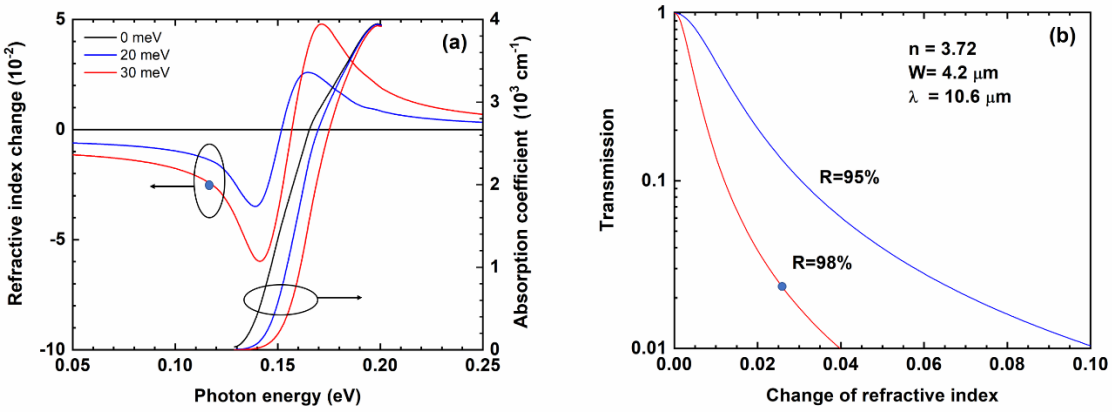

Figure 3- 5. (a) Left y-axis: refractive index change caused by quasi Fermi level rise of 0 (black), 20 (blue) and 30 meV (red) at 77 K. A maximum of 0.06 was obtained by E_F = 30 meV. Right y-axis: absorption edge shift due to quasi Fermi level rise. (b) Transmission as a function of refractive index change in FP etalon. The index, thickness of active region and the targeted wavelength were specified in the figure. According to panel (a), index change is 0.025 at 10.6 μm. Two cases were illustrated for mirror coating reflection of 95% and 98%. The extinction ratio can approach 40 with R=98% at the wavelength of 10.6 μm under full carrier population condition.

The large index change in the bulk InAsSb motivated us to evaluate the effectiveness of the beam intensity modulation implemented with a barrier heterostructure in a Fabry-Perot etalon with high-reflection mirror coating. In this way, the free-space beam modulation depth should be

improved substantially reaching high extinction ratios. According to the equation [88], a 4.2-μm-thick InAsSb active region layer with the reflection of 98 % should demonstrate the extinction ratio (the reciprocal of transmission) approaching 40 at the wavelength of 10.6 μm CO_2 laser.

3.2.3 Conclusion

To conclude Section 3.2, the beam intensity modulation was demonstrated in bulk $InAs_{0.58}Sb_{0.42}$ barrier heterostructure. The modulation was realized by carrier injection into nBp heterostructure based on Burstein-Moss shift. The transmission spectra showed the intensity modulation in a broad photon energy range from 0.12 eV to 0.20 eV with a peak modulation at 8.6 μm. The maximum modulation depth of 9 % was measured with a CW-mode QCL operating at 8.6-μm with the current injected to the InAsSb absorber with a duty cycle of 0.1 %. This number agreed with the modeling results which showed the maximum modulation depth of 8 %. The data suggested the index change up to 0.06 by population of conduction band states described with the Fermi level rise of E_F = 30 meV above the conduction band edge. The implementation of the Fabry-Perot etalon could enable reaching a high extinction ratio of 40 for a free-space laser bean intensity modulation.

3.3 Beam intensity modulation in InAsSb Type-II superlattice

3.3.1 Heterostructure design

The heterostructure consisted of a GaSb substrate, a compositionally graded GaInSb buffer with top portion unrelaxed as the virtual substrate (VS), a type-II SL active region, a 200-nm electron barrier and a p-contact layer. The 3-μm-thick $Ga_{1-x}In_xSb$ linearly graded metamorphic buffer was studied in previous works [25,89–93], the In composition was

incremented from x = 0 to 53 % during growth. The 500-nm-thick unrelaxed, unstrained VS had the composition of $Ga_{0.54}In_{0.46}Sb$. The lattice constant of the VS was 6.27 Å. Both the graded buffer and the VS were Te-doped to the level of $1x10^{18}$ cm^{-3}.

The undoped 2-μm $InAsSb_{0.65}/InAsSb_{0.35}$ SLS active region was grown with a period of 1.8 nm/1.65 nm repeated 580 cycles. The energy band gap estimated from analysis of the experimental data was estimated to be Eg = 85 meV at 77 K, a lower than that in the bulk $InAsSb_{0.6}$ with Eg = 0.1 eV [6]. The energy gap was selected to be sufficiently smaller than photon energy of a 10.6-μm CO_2 laser emitting photos with the energy of Eph = 117 meV. The SLS energy band dispersion in k-space was calculated with the Kronig-Penny model. The average Sb composition in the strain-balanced $InAsSb_{0.65}/InAsSb_{0.35}$ SLS was matching to that in bulk InAsSb on the VS of the same lattice constant. For ordering-free growth, the compressive strain in $InAsSb_{0.65}$ and the tensile strain in $InAsSb_{0.35}$ were designed to be less than 1 %. The heavy-hole miniband width of 70 meV was estimated by an 8-band $k \cdot p$ method.

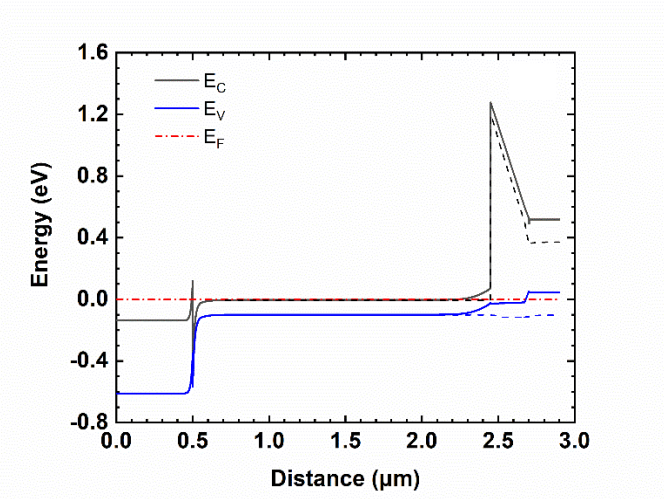

Figure 3- 6. Band diagram of the nBp barrier heterostructure with SLS active region in equilibrium.

The design of the barrier layer was different from that described in the above section for the modulator based on the bulk InAsSb absorber. A compositional graded barrier was applied

from $Al_{0.50}Ga_{0.15}In_{0.35}Sb$ to $Ga_{0.54}In_{0.46}Sb$ followed by a 200 nm thick $Ga_{0.54}In_{0.46}Sb$ p-contact layer doped to a level of 1×10^{19} cm^{-3}. The barrier was moderately p-doped to the level of $1x10^{17}$ cm^{-3}. The thought behind was to have zero valence band offset between the contact layer and the barrier to facilitate the hole injection. The schematic band diagram is shown in Figure 3-6.

3.3.2 Fabrication and experimental setups

The wafer was processed with frontside mesa sizes of 300 µm × 300 µm by etching off the p-type contact layer, in which an open window of 30 µm × 250 µm left open for light propagation. The area other than the window was deposited the p-metal Ti/Pt/Au. The backside window with the dimensions of 300 µm × 300 µm was aligned with the frontside window. The n-side contact was deposited with Ni/Au/Ge/Ni/Au followed by Ti/Pt/Au. The deposition of Pt was made for the purpose of soldering and a 100-nm thick Au was deposited for wire bonding [7].

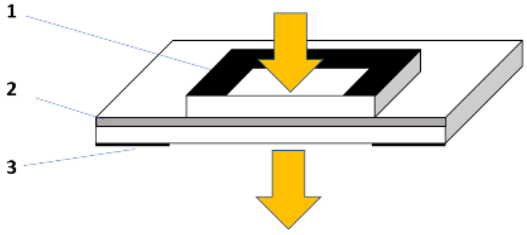

Figure 3- 7. Cross-section schematic of the nBp heterostructure modulator. No 1-3 refer to p-side ring contact, barrier and active region, n-side contact.

The wafer was polished down to a 100 μm thickness for cleaving and minimize losses due to free carrier absorption. The cleaved arrays of the modulators were mounted on the copper blocks with a 1-mm-diameter hole aligned with the window on the substrate side of the samples for optical transmission.

The characterization of the transmission spectra of the SLS modulators was the same as that described in Section 3.2.1. The modulation depth was measured with a Merit-S CO_2 laser operating in the continuous-wave mode. The laser wavelength was stabilized at 10.6 μm. The laser power heating the sample was 30 mW. The laser power density was 400 W/cm^2. The sample area exposed to the laser power was 30 μm × 250 μm. Due to the short-pulse current injection with 100-ns pulse width at 10 kHz repetition rate, the effect of Joule heating on the modulation depth was negligible. However, the heating effect from the current injection was observed in the measurements of the transmission spectra with FTIR under a pulsed injection current and a duty cycle of 10 %. The temperature-dependent measurements of the modulation depth of CO_2 laser beam with a short pulse current injection were conducted at 77 K, 150 K and 200 K.

3.3.3 Results and analysis

For the theoretical analysis of the transmission spectra, the data for the fundamental absorption in the SLS active region and free-carrier absorption in the heavily doped substrate were required. The absorption spectra for the short-period (16.5 Å/18 Å) $InAsSb_{0.35}/InAsSb_{0.65}$ superlattices were studied experimentally in the previous work [51], where the absorption spectra were determined from the transmission measurements by FTIR and HgCdTe detector with cut-off wavelength of 22 μm. A blue shift of the absorption edge due to Burstein-Moss effect was

calculated based on the increase of the quasi Fermi level of electrons. For E_F = 10 meV, 20 meV and 30 meV, in accordance with Equation 3.1.

$$\alpha'(h\nu) = \alpha_0 \frac{1-f_i}{1-f_0} \tag{3.1}$$

Here α' is the interband absorption coefficient under carrier injection, α_0 is the absorption coefficient at equilibrium state, f_i and f_0 are Fermi functions with and without the carrier injection, respectively.

Change of transparency ΔI can be calculated based on the formula proposed for two-layer stacks with a thin film absorber and a semi-transparent substrate [59], where the transmittance is described as,

$$T = \frac{(1-\rho)T_{123}U}{1-\rho R_{321}U^2} \tag{3.2}$$

$$\rho = \frac{(n_1-n_3)^2+{k_3}^2}{(n_1+n_3)^2+{k_3}^2} \tag{3.3}$$

Here T_{123} and R_{321} are ordinary transmittance and reflectance of three-layer stacks computable from the transmission matrix. Indices 1, 2, 3 are referred to the air, absorber, and substrate layers, respectively. The complex refractive indices $\widetilde{N}_i = n_i + ik_i$ $(i = 2, 3)$ were applied to all layers with their corresponding absorption coefficients. The factor $U = \exp(-\alpha_s d_s)$ accounts for the free-carrier absorption in the substrate. In earlier work, it was found to be about 100 cm^{-1} at 10 μm wavelength from the transmission measurements of the sample with a polished off epilayer.

The spectra of the transmission modulation were measured in the wavelength range from 0.05 eV to 0.25 eV. Unlike that measured for bulk InAsSb, the peak of the modulation occurred in a broader range of photon energies roughly from 0.12 eV to 0.17 eV and the peak position was changing with the injected current level. A valley at the photon energy of 0.135 eV was attributed to a feature in the spectral response in the internal MCT-A detector of the FTIR. The

modeling results are illustrated in Figure 3-8 (b) for three different quasi Fermi levels: 10, 20 and 30 meV all at 77 K and for E_F = 20 meV at 200 K. A decrease of the modulation depth and spectral broadening toward shorter wavelengths with temperature were observed. Considering a high duty cycle of current pulses, we attribute the experimentally observed spectral broadening at the shorter wavelengths near 0.20 eV (see Figure 3-8 (a)) to the Joule heating of the devices.

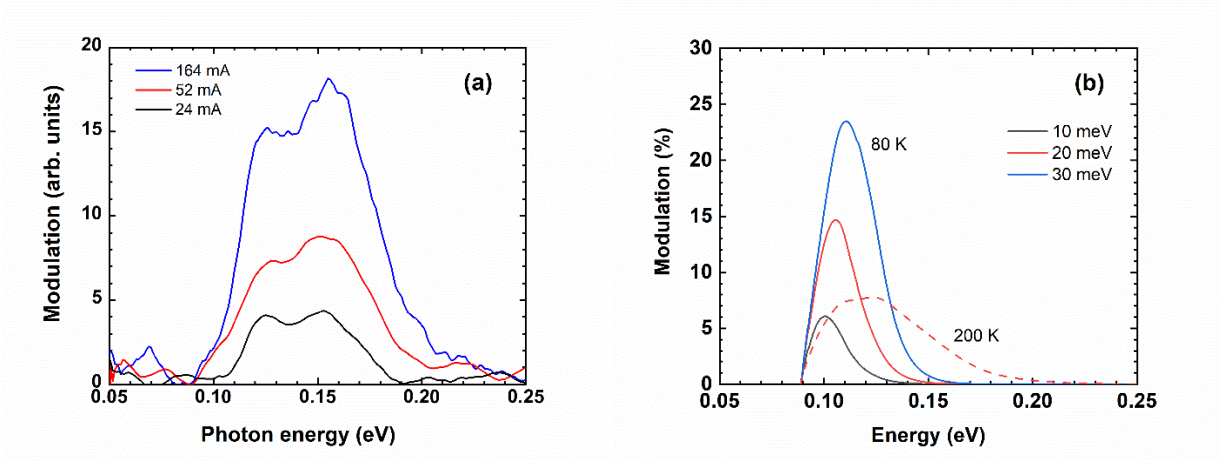

Figure 3- 8. (a) the transmission spectra were measured by FTIR spectrometer, and the modulation depth was illustrated as function of photon energy in arbitrary unit. The actual value of modulation depth was calibrated by short-pulse current injection described in the next figure. (b) Modeling of modulation spectra for quasi Fermi levels of 10, 20 and 30 meV. A broadening of the spectrum was observed for the elevated temperature from 77 K (solid red) to 200 K (dashed red).

The modulation depth was measured with a short-pulse, low duty cycle conditions at 10.6-μm with the CO_2 laser operating in the CW mode. The maximum modulation depths of 7 %, 5 % and 3 % were observed at the temperatures of 77 K, 150 K and 200 K, respectively. (Figure 3-9a). For comparison, the results of modeling of the modulation depth as a function of the excess carrier concentration are shown in Figure 3-9 (b). The maximum increase of the quasi Fermi level by 20 meV with an excess carrier concentration of 2×10^{16} cm^{-3} was obtained by comparison of the experimental and modeled modulation depths.

By matching the modulation depths in panel (a) and panel (b), the lifetime of excess carriers was determined. The injected current in panel (a) and the excess carrier concentration in

panel (b) were taken in pairs for the same modulation depth. The pairs of the current and the concentration were plugged into equation $J = q\frac{\delta n}{\tau}W$, where W is the absorber thickness, and δn is the excess carrier concentration. Using this equation, the lifetime τ was obtained in a range of excess carrier concentration. To reduce the noise, an empirical 5th-order polynomial fitting for the experimental data was conducted with a 95 % confidence bounds. Since in the temperature range of interest the dominant carrier recombination mechanism is Auger process CHCC (Auger-1) [94] , we determined the Auger coefficient with equation $C_n = 1/\tau n^2$, assuming that $C_n \gg C_p$.

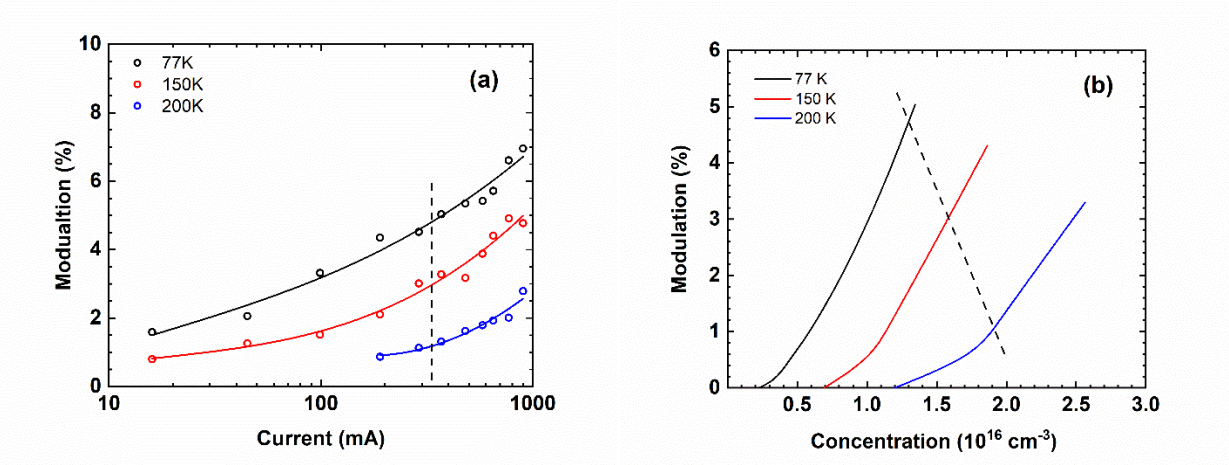

Figure 3- 9. (a) Modulation depth was measured with a laser excitation at 10.6 μm and short-pulse current injection in the modulator. The modulation was determined as a function of injected current levels at the temperatures of 77 K, 150 K, and 200 K. (b) modulation depth as a function of excess carrier concentration at the same three temperatures. Dashed lines in each panel denoted the way of matching the modulation depths for each pair of current and concentration.

The Auger coefficients determined in a range temperatures were fitted by Beattie-Landsberg-Blakemore (BLB) expression as the following [95],

$$C_n = \frac{8(2\pi)^{5/2}q^4 m_0}{h^3(4\pi\epsilon_0\epsilon_\infty)^2}\frac{(m_e/m_0)|F_1F_2|^2}{n_i^2(1+\mu)^{1/2}(1+2\mu)}\left(\frac{k_BT}{E_g}\right)^{3/2} exp\left(-\frac{1+2\mu}{1+\mu}\frac{E_g}{k_BT}\right) \quad (3.4)$$

where m_0 is the free electron mass, $\mu = m_e/m_h$ is the ratio of effective masses for electrons and holes, h is the Planck constant, ϵ_∞ is the high-frequency dielectric constant, n_i is the

intrinsic concentration and $|F_1F_2|$ is the Bloch function overlap integral parameter. The electron effective mass m_e was calculated to be 0.0086 by Kane model [44,96], assuming bulk $InAs_{0.4}Sb_{0.6}$ parameters with the same energy band gap of 85 meV at 77 K [6]. The summary of the BLB model parameters are presented in Table 3-1. For BLB fitting, we used a reduced current range of 30 mA – 150 mA.

Table 3- 1. Summary of the parameters used in BLB fitting.

ϵ_∞	14.14
m_e	0.0086
m_e	0.41
E_g	85 meV
$\|F_1F_2\|$	0.28

The effective mass of electrons in the SLS was derived with Kane matrix P and split-off energy Δ extrapolation using Equation 3.5,

$$\frac{1}{m_e} = \frac{4P^2}{3\hbar^2 E_g}\frac{\Delta+\frac{3}{2}E_g}{\Delta+E_g} \tag{3.5}$$

The found effective mass of 0.0086 was matched to the range of 0.0065-0.011 obtained by magneto-transport measurements for bulk InAsSb with Sb from 44 % to 63% [58]. The Block overlap integral function $|F_1F_2|$ was usually suggested to be 0.1-0.3 in the literatures for HgCdTe [52]. By fitting of the BLB expression to the experimental data for this heterostructure, we obtained $|F_1F_2| = 0.28$. The determined Auger coefficients in a temperature range and the BLB fitting are shown in Figure 3-10.

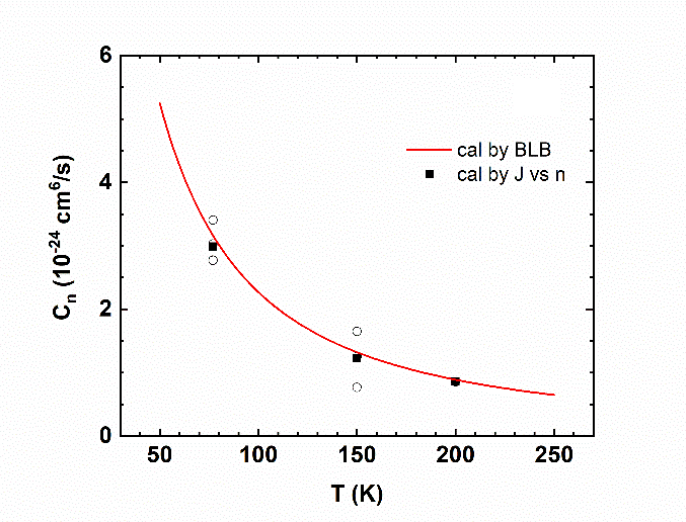

Figure 3- 10. The BLB fitting curve was calculated for this SLS active region. The filled circles represent the average Auger coefficient at each temperature of 77, 150 and 200 K based on the low-current-injection modulation depths from 1 to 4 % represented with open circles.

The change of the refractive index was calculated from the change of the absorption spectrum by Kramers-Kronig relations. The latter is an expression that depicts the relationship between the real and imaginary part of one physical parameter pair, such as absorption α and refractive index n in this case. It can be used for the analysis of the linear optical properties of most semiconductor structures which are satisfied to the requirements of the space-time causality [87]. The refractive index can be obtained as an integral of absorption,

$$\mathrm{n}(\omega) = 1 + \frac{c}{\pi} P \int_0^{+\infty} \frac{\alpha(\Omega)}{\Omega^2 - \omega^2} d\Omega \tag{3.6}$$

where Ω and ω are angular frequencies of photons. The result of integral near singularity ω is a Cauchy Principal Value denoted as P. The integral can be easily solved except for the range near the singularity frequency ω. In the frequency range of $\omega - \delta$ to $\omega + \delta$, it was evaluated with $\delta \to 0$. As suggested by Ref. [86], the integrand can be expanded as Taylor expansion series near the singularity point,

$$n'(\omega) = \frac{c}{\pi}\left[P \int_{\omega-\delta}^{\omega+\delta} \frac{\alpha(\Omega)}{\Omega^2 - \omega^2} d\Omega\right] = \frac{c}{2\pi\omega}\left[-\int_{\omega-\delta}^{\omega+\delta} \frac{\alpha(\Omega)}{\Omega+\omega} d\Omega + 2\,\delta\alpha'(\omega) + \frac{1}{9}\delta^3\alpha'''(\omega)\right] \tag{3.7}$$

We computed numerically both integrals, $n'(\omega)$ in the vicinity of ω and $\mathrm{n}(\omega)$ in the full span, and concluded that the former one can be kept to be less than 1% of the latter, if the step size of $d\Omega$ is chosen small enough. The results of change of refractive index for the maximum modulation depth in the temperature range from 77 to 200 K are presented in Figure 3-11. Here we can see that the maximum change of refractive index -0.05 at 77 K occurs in the vicinity of the superlattice energy band gap of 85 meV.

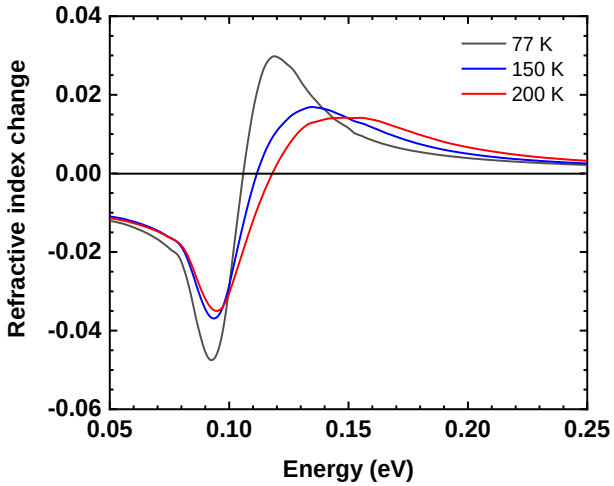

Figure 3- 11. change of refractive index was calculated based on absorption spectrum. For each temperature, maximum modulation depth was selected, with 8.45 % at 77 K, 5.3% at 150 K and 3.3% at 200 K.

Note that at elevated temperatures of 150 K and 200 K, the maximum changes of the refractive index up to 0.037 and 0.035 are similar to the low temperature value. This can be explained with a small decrease of the probability of occupation of highly populated states with temperature near the photon energy of the energy band gap. Due to the term $\Omega^2 - \omega^2$ in the denominator of Equation 3.7, and the integrated contribution of populated states to the refractive index n, the spreading of electron population to high-energy states at higher temperatures does not significantly affect the population in the spectral range of optical transparency (i.e. E < Ec).

The energy band gap in the SLS shows a weak temperature dependence. Thus, due to the factors listed above, the change of refractive index showed a relatively weak temperature dependence.

3.3.4 Conclusion

Carrier-induced beam intensity modulation was studied in barrier heterostructures with type-II InAsSb-based SLS absorbers. The SLS energy band gap of 85 meV at 77 K was selected for the efficient modulation of the beam intensity of a 10.6-μm CO_2 laser. The modulation of transmission spectra was characterized with the FTIR spectrometer in a range of current injection. In the FTIR measurements, a Joule heating was identified to be the major reason for the broadening of the modulation transmission spectra towards higher energy. The intensity modulation depth versus the injected current was measured with short-pulse, low-duty-cycle current injection at the temperatures of 77, 150 and 200 K with the CW CO_2 laser operating at 10.6 μm. The dependences of the excess carrier concentration on injection current were determined from the comparison of the experimental and theoretical modulation depths. The excess carrier lifetime was determined in the temperature range. The Auger coefficient in the temperature range was determined from the lifetime data. The temperature dependence of the CHCC Auger coefficient was found to be in a good agreement with the BLB expression under low carrier excitation approximation. The maximum refractive index change was found to be -0.05 at T = 77 K in the vicinity of the absorption edge. This value is orders of magnitude greater than the change of the refractive index which can be obtained with most EO materials. This approach is attractive for future intensity and phase modulation or applications of beam steering with voltages and currents compatible with CMOS-driver technology.

3.4 Application outlook in beam steering

The development of LWIR beam steering devices was pursued based on the previous accomplishments summarized in section 3.2 and 3.3. The beam steering devices such as Optical Phased Arrays (OPA) are getting attention due to important applications in LiDAR and remote sensing. Nowadays, most of the LiDAR scanning systems are still using conventional beam deflecting method, such as a mechanical controlled moving mirror or a MEMS micro-scanning technology [97]. The mechanical systems are bulky and not fully controlled by electrical signal. Optical phased arrays with electrical control of the refractive index do not comprise moving parts, and thus, offer faster steering and broadband modulation response. The beam steering can be realized with the integrated optical waveguides and grating couplers.

The waveguided phase shifter was realized using the substantial index change derived by the KK relations. The mode confinement with the dielectric waveguide using InAsSb epi-layer grown on GaInSb buffer and GaSb was not sufficient due to the similarity of refractive indices in the GaInSb metamorphic buffer and the GaSb substrate compared to that in the InAsSb active region. Most of the optical power is prone to mode energy leaking into the buffer and the substrate layers. One of the solutions is to use AlInSb graded layer as the metamorphic buffer with a relatively small refractive index. It is a good solution in the case of the optical injection of excess carriers. However, growing the InAsSb active layer on GaInSb graded buffer is more favorable because of the well-known properties such as good electron transport. AlInSb buffers have less attractive electron transport properties. The electron mobility in heavily n-doped AlInSb to the level of $1x10^{18}$ cm^{-3} is ~100 cm^2/Vs at 77 K, in which only about 10% of the dopants are typically ionized. A large concentration of impurity results in higher defect density in AlInSb graded buffer.

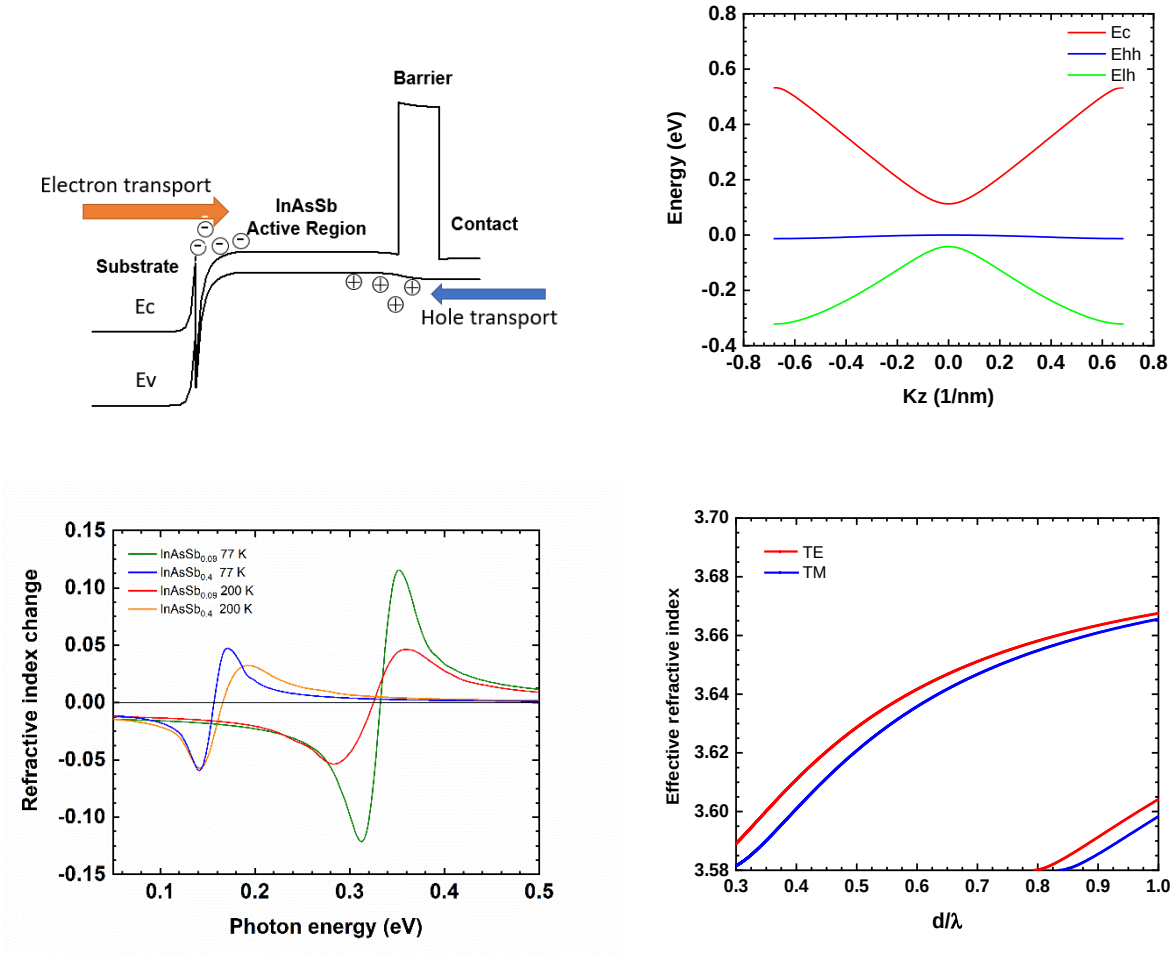

Figure 3- 12. (a) Schematic band diagram of a nBp structure for electron and hole injection. (b) A proposed new design of T2SL $InAsSb_{0.25}/InAsSb_{0.5}$ with a period of 2.6 nm/2 nm and the energy gap Eg = 110 meV simulated at 0 K. (c) Change of refractive indices in MWIR $InAsSb_{0.09}$ and LWIR $InAsSb_{0.40}$ were explored at 77 K and 200 K. Weak temperature dependence of index change can facilitate HOT performance. (d) Supported modes in planar waveguide were calculated for a simplified three-layer stack composed of air with $n_1 = 1$, InAsSb active region with $n_2 = 3.69$ and n-doped GaSb substrate with $n_3 = 3.58$.

The other option is to increase confinement by implementing surface plasmon polariton (SPP) based waveguide which supports TM mode only. In this configuration, the peak of confined magnetic field is pushed towards the metal-dielectric interface. The additional metal losses are needed to be taken into account in the consideration of the maximal length of light propagation [98]. According to the estimations of optical losses for deposited Au metal layer, a 29-μm long waveguide should be sufficient for a phase change of π assuming an index change of

0.05 near the band edge of Eg ~ 110 meV (based on 100% confinement). According to the equation in Ref. [62], π-shift is required for a maximum azimuthal beam steering in OPA.

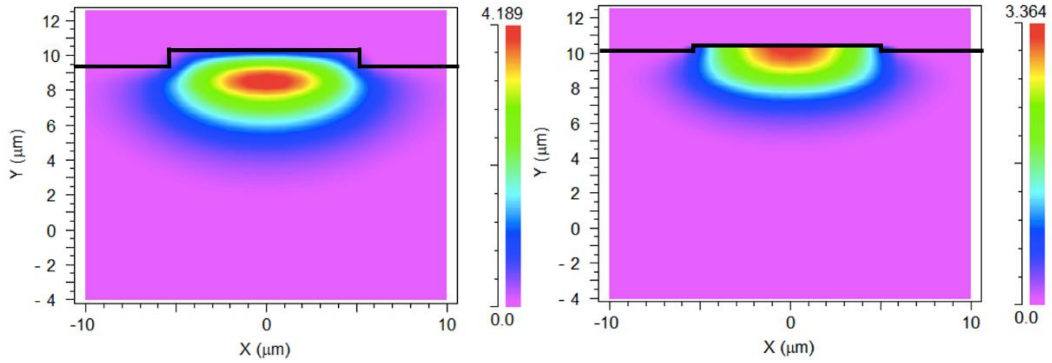

Figure 3- 13. Two examples of magnetic field profile in 10-μm wide (a) dielectric waveguide and (b) plasmonic waveguide for TM0 mode on GaAs. The etching depths were 1 μm and 0.2 μm, respectively. The confinement factors in the 2-μm-thick active region were found to be 46 % and 70 %. The optical confinement was nearly constant in broad ranges of the metal layer width and the ridge etching depth.

On the other hand, the beam steering in the plane normal to the surface can be realized with a grating coupler and the dielectric planar waveguide. A simple idea for implementation of the beam steering is presented in Figure 3-14. The waveguide is fabricated with two grating sections for coupling of the laser light in and outcoupling of the deflected light of a CO_2 laser operating at 10.6 μm. The grating period of Λ = 4 μm at m = 1 was selected under phase matching condition $k_{z0} sin\theta + \frac{2m\pi}{\Lambda} = \beta \pm \Delta\beta$. Here k_{z0} is the wavevector of the incident beam along propagation direction, $m = 0, \pm1, \pm2, ...$, β is the wavevector in the waveguide and $\Delta\beta$ is the change of β due to change of the refractive index.

A broad selection of grating period and the etching depth are viable according to both the analytical calculation (see Figure 3-16(b)) and the numerical modeling in Lumerical FDTD [99]. The simulation of the outcoupling with grating was performed with Lumerical shown in Figure 3-15. For a carrier-induced index change of 0.06, a steering angle of 4.5° was obtained for outcoupling at 45°. The max steering angle up to 20° is hypothetically viable at the outcoupled angle close to 90°. In reality, the outcoupled power drops to zero near the grazing angle.

$$\Delta\theta = \arcsin\left(n_{eff2} - n_g\right) - \arcsin(n_{eff1} - n_g)$$

$$n_g = \frac{m\lambda_0}{\Lambda} \quad \text{m} = 0, \pm 1, \pm 2, \ldots$$

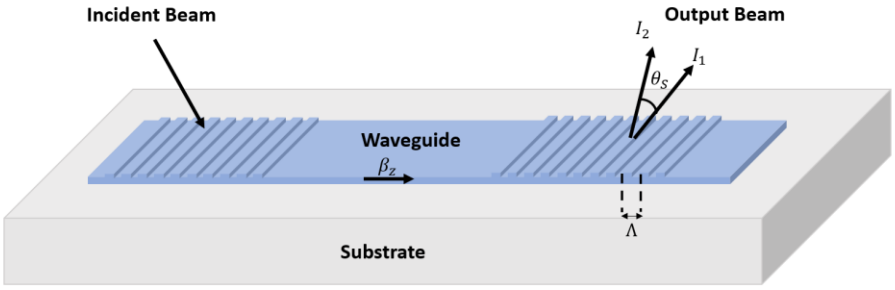

Figure 3- 14. The waveguide with two grating sections for coupling of the laser light and outcoupling of the deflected light. The waveguide index in the region with the second grating was modulated by carrier injection. The equation for Δθ shows the steering angle versus the effective indices in the waveguide with and without carrier injection.

The parameters used in Lumerical simulation were as follows. First, the structure comprised a 2-μm InAsSb waveguide (grating layer thickness not included), a 4-μm AlInSb graded buffer and a 20-μm GaAs substrate. The AlInSb buffer was simplified as a four-layer stack, and each layer was 1 μm. The refractive indices are WG (3.69), graded buffer (3.45, 3.39, 3.33, 3.27), GaAs substrate (3.2). The FDTD was performed in 2D, therefore the layer width was not considered. The total length of the waveguide was 100 μm. The source was a plane wave with an amplitude of 1, whose wavelength was centered at 10.6 μm with a FWHM of 2.40 μm. The purpose of the broadband beam in frequency domain is to provide a longer pulse in time domain. The grating period in Figure 3-15 is 4 μm with a duty cycle of 50 %. The etching depth is 500 nm.

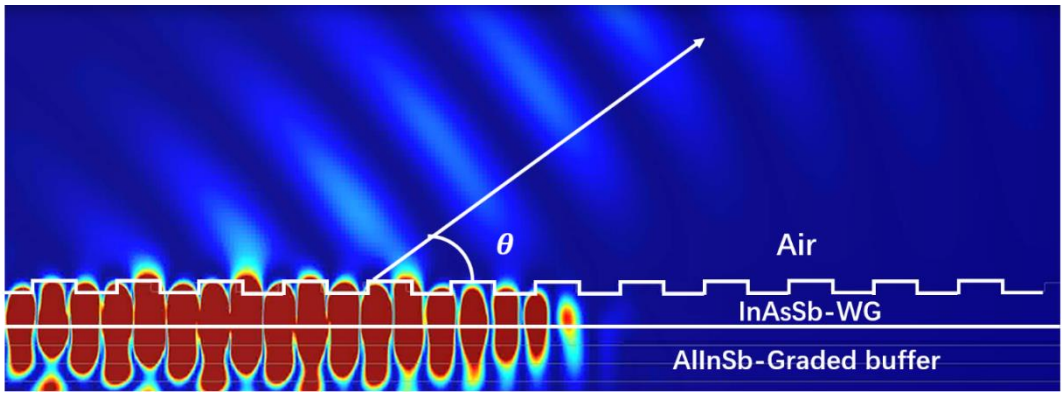

Figure 3- 15. 2D FDTD simulation of the grating coupler. The structure is composed of a 2-μm thick InAsSb waveguide grown on a 4-μm thick AlInSb graded buffer and GaAs substrate. With a period of Λ=4μm, the beam was outcoupled at 45°.

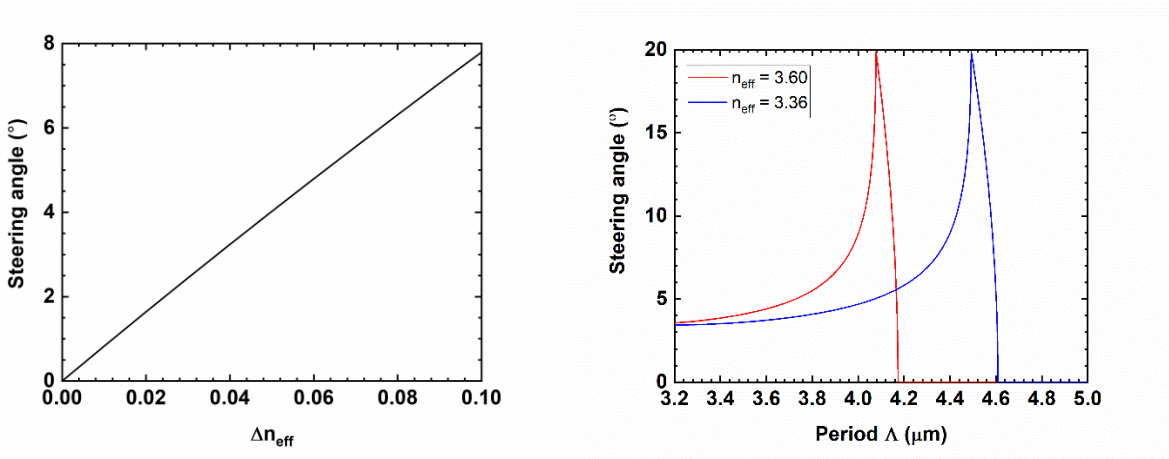

Figure 3- 16. (a) Dependence of vertical steering angle on the refractive index change. (b) Steering angle as a function of grating period assuming an index change of 0.06. Max steering angle reaches 20°. Two cases were simulated based on plasmonic WG with neff = 3.60 and dielectric WG with neff = 3.36.

3.5 Summary

To summarize Chapter 3, free-space beam intensity modulation in InAsSb-based nBp barrier heterostructures have been demonstrated at LWIR region due to the strong fundamental absorption. The heterostructure comprised bulk $InAsSb_{0.42}$ with Eg = 133 meV, and the heterostructure comprised T2SL $InAsSb_{0.65}/InAsSb_{0.35}$ with Eg = 85 meV at 77 K were fabricated. The maximum modulation depths were determined be to 9 % for an 8.6-μm QCL and

7 % using 10.6-μm CO_2 laser, respectively. These data were in good agreement with the transmittance modeling results. Using the measured and simulated modulation of the transmission spectra, the elevation of the quasi Fermi level was found to be 20 meV and the electrically injected excess carrier concentration above Ec was found to be (1-2) $x10^{16}$ cm^{-3}. The dependences of the excess carrier concentration on the injected current density were used for determination of the excess carrier lifetime, and the temperature-dependent Auger coefficients for CHCC recombination process. By Kramers-Kronig relations, the refractive index changes up to 0.05 in InAsSb-based materials were obtained. Based on that, an insight on the application of the effect for optical beam steering was discussed which included the devices based on the optical phased arrays and the devices based on grating couplers. The design options for the optical waveguides were proposed.

Chapter 4 Modeling of the integrated double-barrier heterostructure for pixel multiplexing

4.1 Introduction

During last decades, researchers have kept their long interest in exploring III-V compound semiconductors. The unique properties of III-V compounds make them suitable for use in the field of integrated circuit, optoelectronic devices and high-power electronics. Moreover, the engineering of energy gaps of semiconductor compounds, alloys and SLS, dramatically expands the range of device operation spectrum from X-ray to long-wave infrared region. The energy band gaps for most III-V compounds are direct and tunable by change of the composition. The energy gaps of ternary alloys can be approximated by a linear combination of the energy gaps of binary compounds with a bowing parameter defined by the following equation: $Ax + B(1-x) - Cx(1-x)$, where A and B are the energies (Ec, Ev or Eg) of two binaries and C is the bowing parameter. With the negative sign of bowing parameter C, the band gap of the alloy is smaller than the value defined by the sum of weighted linear combination two binary compounds.

Modern arrays of LED require high resolution, e.g. 1000x1000 lines. The current technology requires the fabrication of individual contacts to drive millions of pixels to be addressed [100,101]. Making connections to each pixel reduces the yield as there is finite probability of fabrication defects. The CMOS electronic circuit with an individual driver becomes expensive to design and fabricate. Switching of the pixels performed in silicon requires more than millions of ball bumps. This can be realized by Ball Grid Array (BGA), which is an industrial standard package for large number of multiplexing arrays with high densities up to thousands of bump but not in the scale of a million. BGAs require precise alignment in

integration with the III-V LED matrix and possess challenges in inspection and reliable soldering.

In this chapter, we discuss the LED matrix design which requires a considerably lower number of electrical contacts. It is realized by organization of LED pixels into 1D arrays and array multiplexing on the chip. In this way, the number of required external contacts can be reduced from a million down to 2,000. The latter can be implemented with the modern BGA technology with high yield and reliability. The LED pixels are multiplexed in time domain so that each pixel must be driven with a low duty cycle high pulsed current to maintain the same light intensity as in the case of DC driving with individual addressing. An LED pixel is selected by applying the drive current to a row and the control potential to a column of the LED array. In the perspective of the control multiplexer integrated with the LED array on the same chip, the power dissipation of the multiplexer should be a small part of the power dissipated by the entire LED array. Since the maximum LED power is limited by the array overheating, it is important to design the multiplexers with a low dissipated power. The latter has to be below the power dissipated by the LED array in order to have the intensity of LED with multiplexers to be comparable to that of the LED array with individual pixel addressing. Thus, of the goals of the design considered below was to keep the power die to switching on/off the pixels at the minimum. The power dissipated by the integrated multiplexer was one of the critical design parameters. One prospect of designing the novel integrated switching arrays is to achieve high current gain, defined as the ratio of injection current over control (gate) current, by minimizing the control power consumption. On the other hand, the on/off switching ratio should be sufficiently high in order to address one pixel (turn it on) out of a thousand pixels which are supposed to be in off state with a low dissipated power.

we proposed an integrated double barrier heterostructure with a conducting gate layer between the barriers for control of the LED pixel injection current. The multiplexer circuit dissipated a small current which controlled the pixel injection current. The ratio of the injection and control current is defined as the current gain of the multiplexer. The current gain and 2D current distribution were simulated. The potential application includes MWIR light emitting diode (LED) and modulator arrays.

4.2 Considerations in design of the double barrier gated LED

The material compositions for the active LED region and the barrier layers were selected with the requirement of a large conduction band offset and near-zero valence band offset between the narrow gap active region and the barriers. The band gap of the active region was selected to be in the mid-wave IR range, i.e. 3-5 μm. The lattice constants in each layer must be either unstrained or strained-balanced to guarantee high-quality growth and low defect density for a low non-radiative recombination current in the active region. For the active region, $InAs_{0.91}Sb_{0.09}$ alloy with 9% Antimony lattice matched to 6.09-Å GaSb substrate was selected. The estimated band gap of the $InAs_{0.91}Sb_{0.09}$ alloy is Eg = 0.29 eV at 200 K as shown in Figure 4-1a. The calculation for the absolute energy levels referred to the Vurgaftman's review of III-V compounds parameters [17] and the up-to-date bowing parameter of $InAs_{1-x}Sb_x$ measured in our group to be C= 0.87 eV [26]. The bowing parameter C of 0.87 eV for the energy gap was obtained with a low temperature photoluminescence data. It includes the contributions from separate bowing parameters for the conduction and valence bands. A reasonable splitting for the bowing parameter C into conduction band component Cc and valence band component Cv was

inferred from theoretical modeling of absorption spectra by Vurgaftman et al., where Cv was chosen to be 0.15 eV [51].

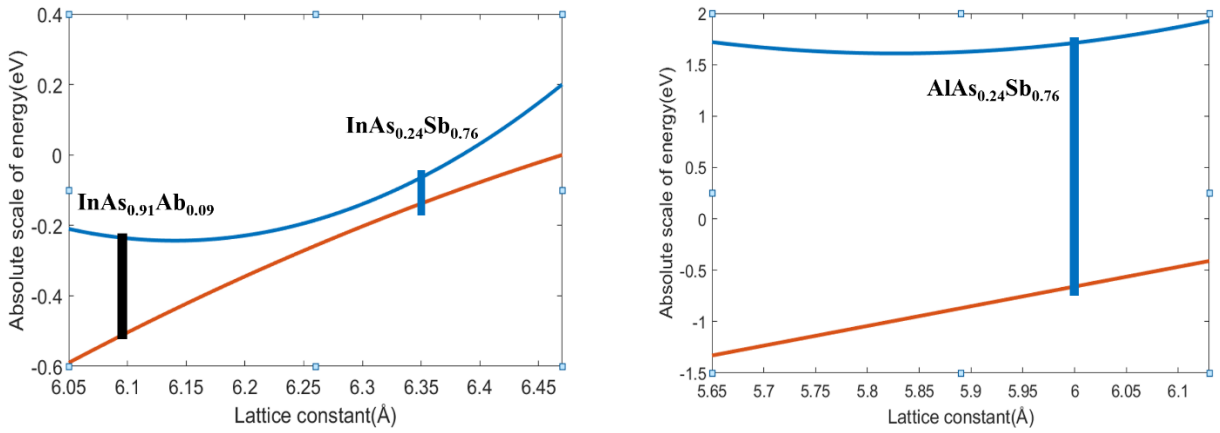

(a) (b)

Figure 4- 1. Energy levels in two ternary compounds InAsSb (a) and AlAsSb (b) using bowing parameters of 0.87 and 0.8, respectively.

For a wide-band-gap barrier, we selected AlInAsSb alloy lattice matched to GaSb substrate with a low valence band offset with the InAsSb active region. To guarantee the lattice-matched growth and minimize valence band offset, the barrier composition was determined to be as follows: a 80% Al (20% In , respectively), and a 24% As (a 76% Sb, respectively). In the selection of the barrier composition, we assumed a linear interpolation of InAsSb and AlAsSb ternaries. A bowing parameter of C = 0.8 eV in conduction band and no bowing in valence band were assumed for $AlAs_{1-x}Sb_x$ [17].

The energy levels in the active region and barrier are shown in Table 4-1. The energy of Ec, Ev in the absolute scale were calculated at 200 K and the parameter space was later applied in PADRE simulation. A near-zero valence band offset and the conduction band offset of 1.22 eV were determined, allowing for unimpeded hole transport from the top contact injector to the active region across two barriers and a complete blocking of the electron current.

Table 4- 1. Energy levels and band gaps of III-V compounds selected for the active region and the barrier calculated at 200 K, no bowing was applied to AlInAsSb and bowing of 0.87 was applied to InAsSb with 0.15 assigned to valence band.

Material	Ec (eV)	Ev (eV)	Eg (eV)
$InAs_{0.91}Sb_{0.09}$	-0.232	-0.524	0.291 (Γ valley)
$Al_{0.80}In_{0.20}As_{0.24}Sb_{0.76}$	0.988	-0.533	1.521 (X valley)

4.3 Double barrier gated heterostructure design

The double-barrier heterostructure composed of 5 epitaxial layers was proposed. A single pixel contained, from the bottom to the top, a GaSb substrate, a 1 μm active region, a 0.2 μm first barrier, a 0.2 μm gate layer, a 0.2 μm second barrier, and a heavily doped 0.2 μm carrier injector as shown in Figure 4-2. Metal contacts were deposited on the top of the injector, the gate, and at the bottom of the substrate.

The design parameters including doping levels of the layers we optimized by modeling for a fast switching rate and high current gain with low power dissipation. The double barrier gated heterostructure functioned as the current multiplexer. The barrier adjacent to the active region helped reduce the width of the depletion region in the active region thus surface current and generation-recombination current [102] at the heterostructure interface of the barrier with the active region. The purpose of adding the second barrier was to reduce the backward electron transport from the gate to the injector (the current direction is from the injector to the gate). The hole transport is controlled by rising or lowering the valence band in the gate to realize the switching of the device on /off with a small control current. The injection of holes is realized by applying the positive voltage to the highly n-doped top injector layer. It results in a large

diffusion current in the vertical direction from the top contact injector layer towards the active region. Thus, the switching between on and off states is obtained by change of the voltage between injector-gate V_{ig}. Figure 4-2 shows a 3D view of the double-barrier structure device. The heterostructure with a narrow bandgap InAsSb active region and wide bandgap AlInAsSb barriers is grown by MBE on GaSb substrate. All layers are lattice matched to GaSb substrate with no residual strain. The doping types and levels for each layer are listed in Table 4-2.

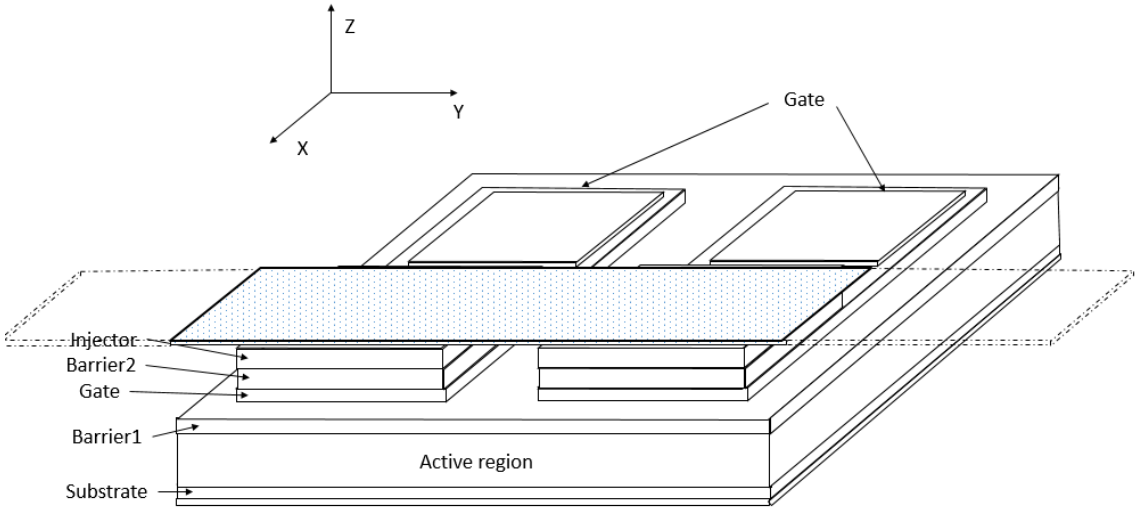

Figure 4- 2. 3D view of the double barrier heterostructure device with two pixels, the dashed-line plane refers to the contact connected over multiple pixels in the horizontal direction. The pads on the rear side coated on the gate layer are supposed to connect along x axis.

Beryllium doping level of the barriers was selected to eliminate a potential energy bump impeding the vertical transport for holes [57]. The barriers need to be fully depleted for effective control of valence band potential in the gate layer. Injection of holes to the active region requires a heavily p-doped top injector layer. Considerable effort was made for optimization of the doping concentration in the gate layer. The n-type doing of the gate layer with tellurium to the level of 3e16 cm^{-3} was determined to the optimal by exploring a trade-off between the required long minority hole lifetime in the gate for low recombination current in the gate and a high

lateral gate layer conductivity for a low voltage drop in the planar device. The details of the design parameter selections will be discussed in the following section in relation to analysis of I-V characteristics.

4.4 2D modeling of double barrier heterostructure by PADRE

Modeling of IV characteristics of a single pixel of the 2D LED array was implemented in PADRE software operating under Solaris and Linux operating systems [103]. The PADRE software was developed by Bell Labs to solve the hydrodynamic equations in the drift-diffusion approximation in steady state, transient and with period small-signal AC excitation conditions.

Table 4- 2. Summary of doping types and levels in each layer of double barrier heterostructure device

	Material	Doping Type	Doping Concentration (cm^{-3})
Substrate	GaSb	*n*	1e18
Active Region	$InAs_{0.91}Sb_{0.09}$	*n*	3e15
Barrier1	$Al_{0.80}In_{0.20}As_{0.24}Sb_{0.76}$	*p*	1e16
Gate	$InAs_{0.91}Sb_{0.09}$	*n*	3e16
Barrier2	$Al_{0.80}In_{0.20}As_{0.24}Sb_{0.76}$	*p*	1e17
Injector	$InAs_{0.91}Sb_{0.09}$	*p*	1e18

It solves a coupled set of partial differential equations supported with a variety of physical mechanisms, including carrier mobility, generation/recombination rates, for various

device shapes and boundary conditions. One feature of the PADRE framework is the capability of modeling 2D and 3D semiconductor devices. The software is available on nanoHUB website as a free tool.

4.4.1 Diffusion-drift model

The diffusion-drift model used in the simulation is composed of the following equations 4.1 - 4.5. For simplification, we considered the steady state condition with a little perturbation deviating from the thermal equilibrium under a constant temperature.

The sets of equations were derived from the Boltzmann transport equation to get the expressions for the current with the drift and diffusion terms shown below. Here V is the potential and μ is the mobility of n and p types of carriers.

$$J_n = q\mu_n(\frac{k_BT}{q}\nabla n - n\nabla V) \tag{4.1}$$

$$J_p = q\mu_p(-\frac{k_BT}{q}\nabla p - p\nabla V) \tag{4.2}$$

The continuity equations below describe the conservation of the total number of carriers as follows,

$$\nabla \cdot J_n = qU(n,p) + q\frac{\partial n}{\partial t} \tag{4.3}$$

$$\nabla \cdot J_p = -qU(n,p) + q\frac{\partial p}{\partial t} \tag{4.4}$$

where $U(n,p)$ is the net recombination/generation rates for electrons and holes. The last one is the Poisson Equation,

$$\nabla \cdot (\varepsilon\nabla V) = q(n - p + N_A - N_D) \tag{4.5}$$

where N_A and N_D are acceptor and donor concentrations, respectively.

In the model three carrier recombination mechanisms were considered: Shockley-Read-Hall (SRH), radiative and Auger type. The total carrier lifetime was calculated as,

$$\frac{1}{\tau_{total}} = \frac{1}{\tau_{SRH}} + \frac{1}{\tau_{radiative}} + \frac{1}{\tau_{Auger}} \tag{4.6}$$

Here each of the type of carrier recombination is described by a corresponding lifetime. The SRH lifetime was taken in the form

$$\tau_{SRH} = \frac{\tau_p(n+n_1)+\tau_n(p+p_1)}{n_0+p_0} \tag{4.7}$$

where τ_p and τ_n are lifetime for holes and electrons, respectively. n_1 and p_1 are determined by the trap energy level with respect to the conduction and valence band edges, respectively. The excess carrier lifetime values for holes and electrons are determined by defect density N_t, capture cross section $\sigma_{n,p}$ and thermal velocity $v_{n,p}$.

$$\tau_{n,p} = \frac{1}{\sigma_{n,p} v_{n,p} N_t} \tag{4.8}$$

The radiative lifetime under low injection rate was taken to be,

$$\tau_{radiative} = \frac{1}{B(n_0+p_0+\delta n)} \tag{4.9}$$

where δn is the excess carrier concentration under non-equilibrium condition and B is the radiative coefficient. In many cases for Auger recombination process only Auger-1 and/or Auger-7 types are sufficient to consider. Auger-1 is the process with recombination of electron hole pair with the excess energy transferred to another electron (CHCC), Auger-7 is the process with the excess energy transfer to hole typically excited to a split-off hole subband (CHHS). Typically one these cases dominates depending on the types of doping in materials [52]. The Auger recombination rates are given by, $R_n = C_n n^2 p$ and $R_p = C_p n p^2$, where $C_{n,p}$ are Auger coefficients for type-1 and type-7 processes.

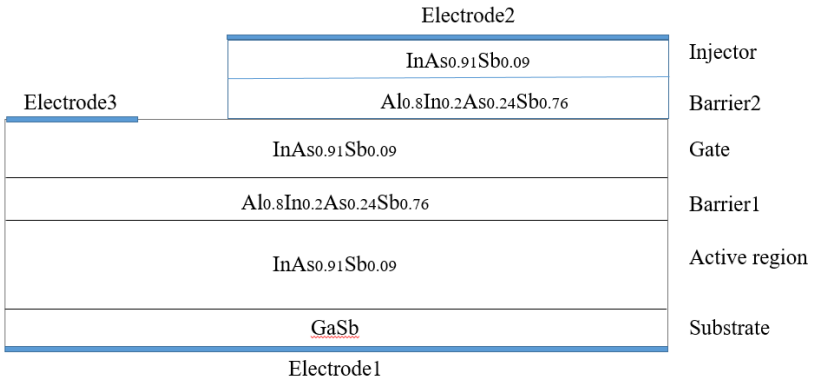

Figure 4- 3. Cross-section schematic of double-barrier multiplexing device.

4.4.2 Device geometry and definition of the device parameters

The modeling was performed in PADRE by defining geometry of the device and the material parameters. The physical models defined in PADRE for the double barrier heterostructure device included: doping concentrations; Auger, radiative, and Shockley-Read-Hall (SRH) three types of recombination mechanisms with concentration-dependent lifetime; statistics (Fermi or Boltzmann); generation-recombination rate; the tunneling model was also included and the temperature was set to 200 K. The LED pixel mesa size for a single device was set to 20 x 20 μm^2. A larger mesa of 200 x 200 μm^2 was also modeled for the case with no edge effects involved. The data were used assessment of the efficiency of the current injection, the role of the current spreading and carrier diffusion in the small mesa.

The geometrical definition is described in Figure 4-3, where a finer mesh with the density of 35 node/μm was used in the vertical direction and 0.5 node/μm was used in the lateral direction. The total thickness of the epitaxial layer was 2 μm. The mesa had a side lateral contact to control the gate potential. The total largest lateral width was 45 μm with a gap of 5 μm between the metal contacts of the gate and the injector. Thus the top metal contact was covered a

width of 20 μm for the small mesa and 200 μm for the large mesa. Doping concentration levels are described in Table 4-2. More device design details can be found in Appendix III.

To consider more realistic model of the double barrier structure, parameters including mobility, minority carrier lifetime [104], effective mass [105] and radiative-lifetime coefficient [106] and Auger coefficient [104] were cited from more recent papers or estimated by calculation. Olson et al. [104] studied the lifetime of bulk III-V and type-II superlattices (T2SL) and plotted the temperature dependence of lifetimes with three types of recombination mechanism: Shockley-Reed-Hall (SRH), radiative and Auger. At high temperatures (T = 200 K), the recombination lifetime is primarily limited by Auger recombination for which a lifetime of 200 ns was taken. The n-type doping concentration in the reference was similar to our case in the gate layer, thus we applied the lifetime to postulate the Auger coefficient under 200 K to be 10^{-26} cm^3/s. Regardless of the well-defined radiative-lifetime coefficient, the simulation results implied the recombination current was Auger-limited. All the parameters used are listed in Table 4-3.

Table 4- 3. parameters applied in PADRE simulation at 200 K.

$C_n(cm^6/s)$	$B_0(cm^3/s)$	n-type Mobility (cm^2/Vs)	p-type Mobility AlInAsSb (cm^2/Vs)	Electron Effective Mass in InAsSb
1×10^{-26}	7×10^{-11}	1×10^{4}	1×10^{2}	0.02

Hole Effective Mass in InAsSb	Electron Effective Mass in AlInAsSb	Hole Effective Mass in AlInAsSb	Intrinsic Minority Carrier lifetime (s)
0.4	0.071	0.35	1×10^{-6}

4.4.3 Modeling results and discussion

The following simulation results were extracted: the conduction and valence band energy levels, quasi-Fermi levels for electrons and holes, electron and hole concentrations, the metal contact currents and the 2D current density distribution.

The band diagrams of the double barrier heterostructure device in the growth direction (Figure 4-4) were simulated for three operating modes. The panel (a) shows the potential profiles under zero bias for all metal contacts, and the panels (b) and (c) show the band diagrams in the on and off states, respectively. Both zero-bias mode and off state showed a negligible injection current as expected due to a large bump in the valence band blocking the hole transport into the active region. In the on state, the valence band potential of the injector layer was bent down to the same energy level as that of the active region. The turn-on bias for hole injection was found to be 0.15 V. Considering the trade-off between minimizing the control current I_g and increasing the active-region current I_a, the voltage between the injector and the substrate was selected to be 0.4 V. At that bias voltage the quasi-Fermi level of electrons increased by 37 meV above the conduction band, indicating the effective injection of holes and recombination of carriers in the active region. In the device switched on with a zero gate voltage, most of the holes would recombine in the gate region. It meant a significant part of the injected current would turn to the control current I_g, which is not desired. It was found that a +0.2 V applied to the gate contact greatly reduces the recombination of carriers in the gate region. The simulation demonstrated that a 99 % of the gate current was suppressed with that gate bias while a 70% of injected holes eventually reach the active region. A sufficiently high ratio of the currents in the on and off states can be obtained with V_g = 0.2 V, V_i = 0.4 V under ~μA range of the control current which is less than a 0.1 % of the total injected current.

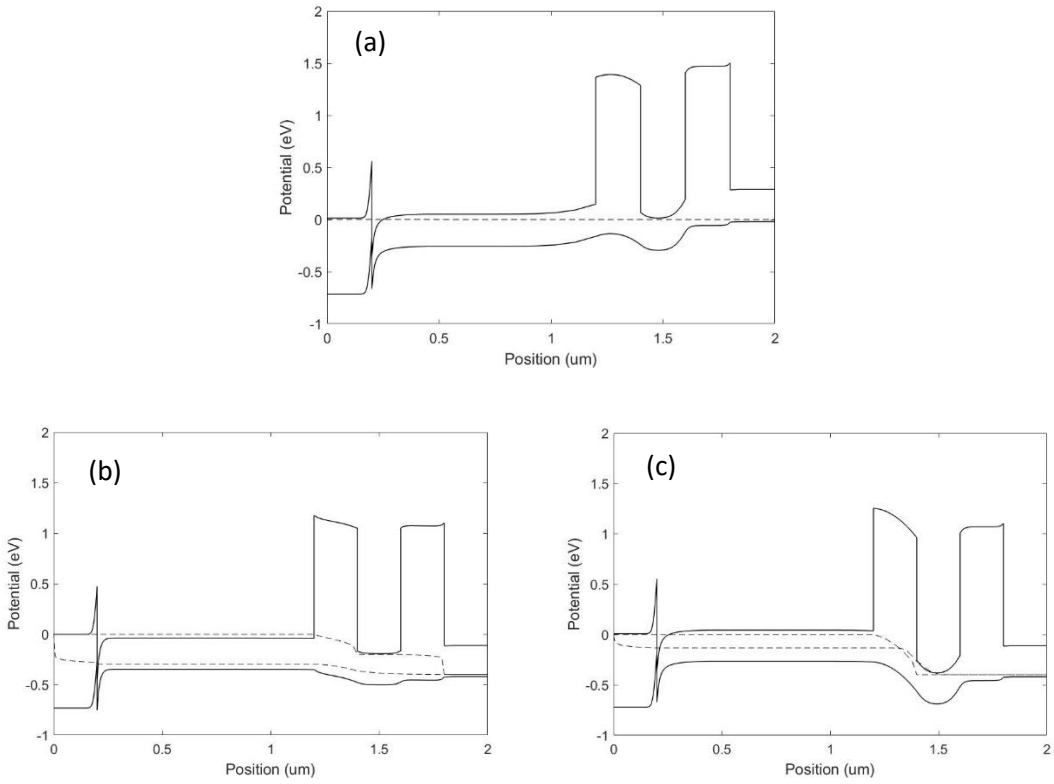

Figure 4- 4. Potential profile of Ec, Ev and quasi-Fermi levels in the double barrier heterostructure device under zero bias (a), on (b) and off (c) states.

The device I-V characteristics and 2D current density distribution were simulated to assess the device current switching performance. At the injector bias voltages $V_i < 0.3$ V, a small negative gate current was observed as shown in Figure 4-5(a). The gate current was flowing from the gate to the injector. The direction of the gate current was opposite to the direction of the gate recombination current. That negative gate current was attributed to thermal generation of excess carriers in the gate region. With a compensation voltage of 80 mV applied between the injector and the gate, the recombination current in the gate was increasing which cancelled out the negative current due to thermal generation of carriers in the gate region. A further investigation was done to verify this speculation.

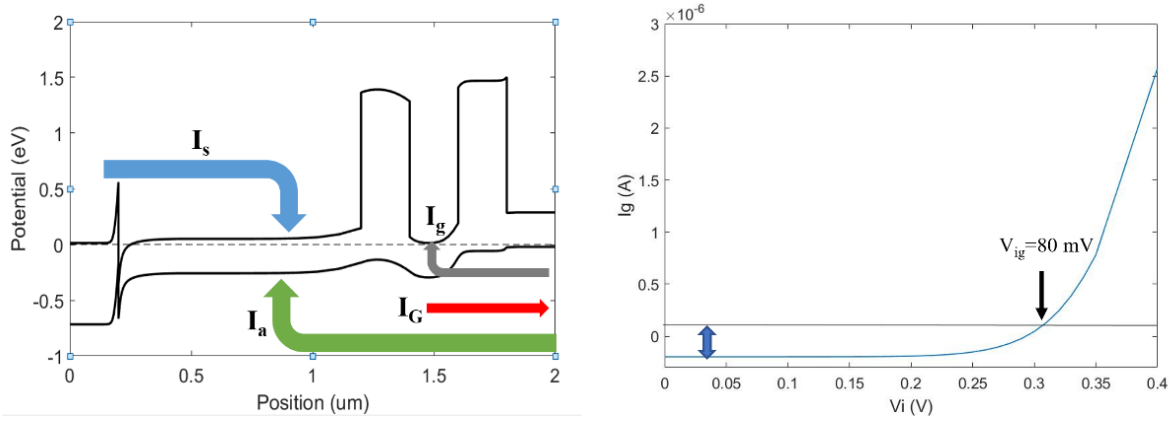

(a) (b)

Figure 4- 5. (a) Current flow in the device. It composed of substrate electron current I_s, active region hole current I_a, control current I_g and backward thermal generation current I_G. (b) Gate current vs injector voltage Vi. A compensation voltage of 80 mV was found to cancel out the negative I_G.

The thermal generation current is a weak function of the concentration of carriers. It is caused by two mechanisms: the band-to-band thermal generation and the thermal generation through the SRH centers. The band-to-band recombination/generation rate is defined as,

$$U_{b-b} = R - G_{therm} = b(np - {n_i}^2) \tag{4.10}$$

$$J_{b-b} = q \int U_{b-b}\, dx \tag{4.11}$$

$$= qb{n_i}^2 (\exp\left(\frac{Va}{V_T}\right) - 1) x_g$$

where $J_{b\text{-}b}$ is the thermal generation current which occurs with $np \ll {n_i}^2$ under the reverse bias, b is bimolecular recombination constant, Va is the bias voltage applied in the gate with a layer thickness of x_g. The bimolecular recombination constant is proportional to the average velocity of carriers v and cylinder scattering cross section σ. The SRH recombination/generation rate and the SRH current density are defined as follows,

$$U_{SRH} = R - G_{therm} = \frac{np - {n_i}^2}{n + p + 2n_i \cosh\frac{E_i - E_t}{kT}} \frac{1}{\tau_{SRH}} \tag{4.12}$$

$$J_{SRH} = q \int U_{SRH}\, dx \tag{4.13}$$

$$\approx q\frac{n_i}{2\tau_0}\left(\exp\left(\frac{Va}{V_T}\right)-1\right)x_g$$

the SRH lifetime $\tau_{SRH}=1/N_t\sigma_t v_{th}$ is determined by the density of traps N_t, cross section of traps $\sigma_{n,p}$ and thermal velocity $v_{n,p}$.

In our case, the designed device at the temperature of 200 K was not limited by SRH, hence the thermal generation rate was dominated by the band-to-band carrier generation process. The thermal generation rate can be further simplified as,

$$G_{therm}=b{n_i}^2 \tag{4.14}$$

where $b=v\cdot\sigma$, and the intrinsic carrier concentration n_i is temperature-dependent described as,

$${n_i}^2=N_cN_v\exp\left(-\frac{E_g(T)}{k_BT}\right)\propto T^3\exp\left(-\frac{E_g(T)}{k_BT}\right) \tag{4.15}$$

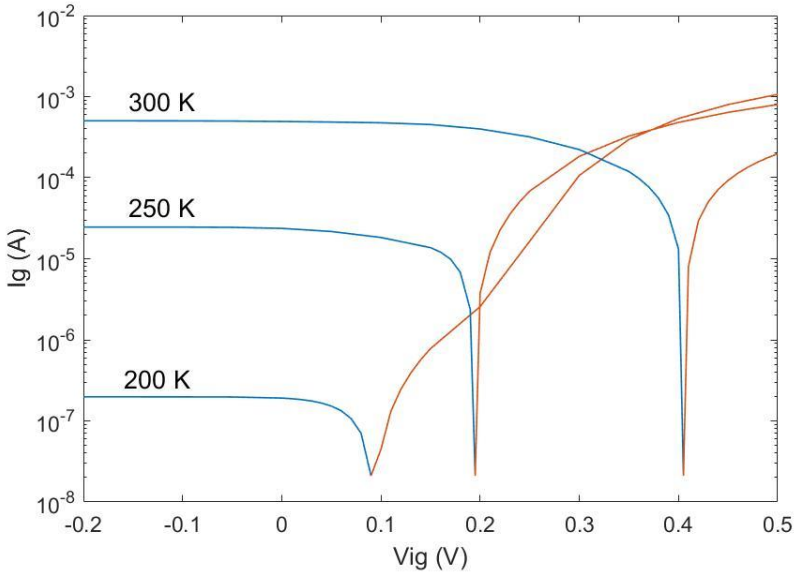

Figure 4- 6. Temperature-dependent thermal generation current at 200 K, 250 K, 300K. The saturated thermal currents under negative V_{ig} (blue) exhibited a linear dependence of ${n_i}^2$.

Based on the formula, a group of simulations in the range of temperature of 200 K, 250 K and 300 K were tested and the ratio of saturated gate current under negative V_{ig} was supposed to be proportional to ${n_i}^2$. The temperature-dependent thermal current as a function of injector-gate

voltage was plotted in Figure 4-6 in absolute scale. The saturated thermal currents under negative V_{ig} exhibited a linear dependence of n_i^2.

Dependence of hole current on injector voltage V_i and gate voltage V_g were studied. The common ground was applied to the substrate contact. The voltage bias of V_i = 0.4 V and V_g = 0.2 V was used at on state, and V_i = 0.4 V and V_g = 0.4 V was used at off state. Voltage sweeps of the injector-substrate voltage V_i based on fixed gate voltage V_g under two operation modes (i.e. V_g = 0.2 V and V_g = 0.4 V) are illustrated in Figure 4-7, where the blue and red line depicted the dependences of injector current I_i on the injector bias V_i at on and off state, respectively. At off state, a gate voltage of 0.4 V was sufficiently large for blocking the hole injection as red line indicated, where negligible change of current was found by varying V_i. In contrast, the injector current I_i varied over four orders of magnitude at on state can approach a current density level 1000 A/cm^2, presumably good enough as a high-brightness LED array [107]. Moreover, a high active region current density of $J_a = 1.66 \times 10^3$ A/cm^2 and a high switching ratio $I_{i\text{-}on}/I_{i\text{-}off}$ = 5600 were simultaneously obtained.

Voltage sweeps of the gate voltage V_g was also conducted based on fixed injector voltage of V_i = 0.4 V for stable hole injection. The active region current I_a and gate current I_g were illustrated in Figure 4-8. At zero gate bias, the current collected in the active region was quite high, but 10% of the total current was consumed by the gate current for multiplexing. On the other hand, at our selected operating point of V_g = 0.2 V, the active region current I_a dropped slightly while the gate current was suppressed by 99%. As an estimation, the current gain defined as $\beta = I_a/I_g$ = 2580. This number was much higher than that in the regular bipolar junction transistor, where a common-emitter DC current gain is typically in the range of 20 - 200.

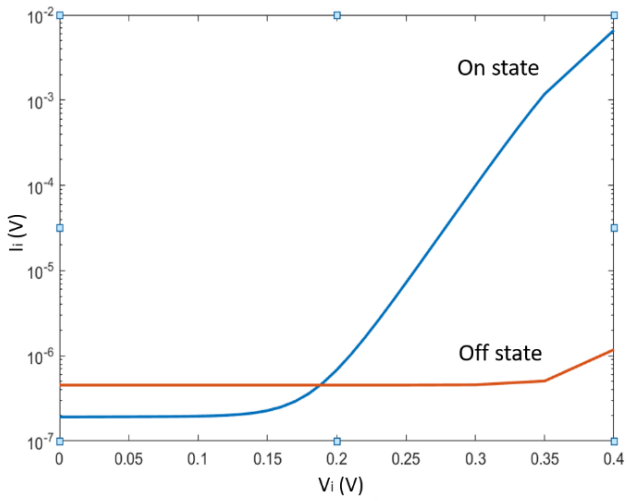

Figure 4- 7. I-V characteristic of I_i vs V_i based on two fixed gate voltages under their corresponding operation modes (on/off).

In order to optimize the doping level of gate layer, studying the current dependence on doping concentration provided a way to explore the tradeoff between higher current gain and lower off-state current. With modeling we figured out the important role of the gate doping level. The dependences of four types of currents on gate doping level are shown in Figure 4-9 in logarithmic scale. The four types of currents were $I_{a\text{-}on}$, $I_{g\text{-}on}$, $I_{a\text{-}off}$, $I_{g\text{-}off}$. Three of them were decreasing with increase of the doping concentration except $I_{g\text{-}on}$.

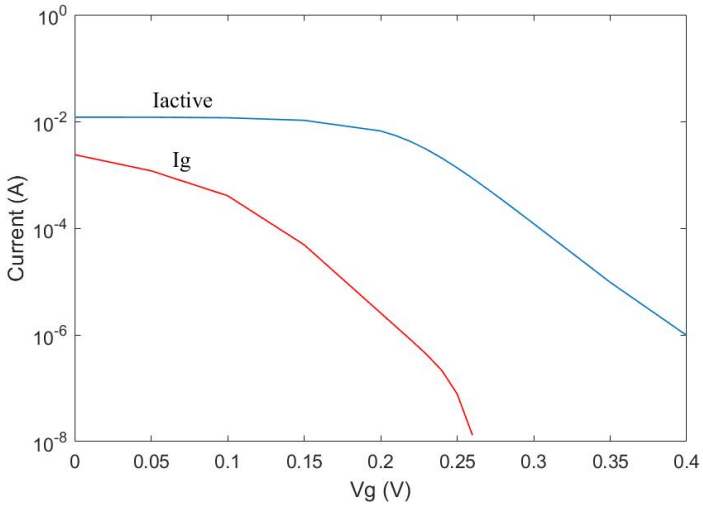

Figure 4- 8. I-V characteristic of current dependence on gate voltage V_g at fixed injector voltage of 0.4 V.

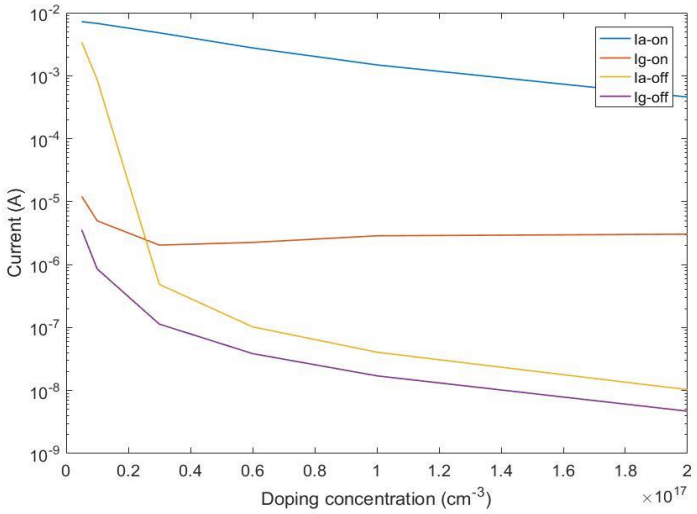

Figure 4- 9. Dependence of active region and gate current on doping concentration were explored. n-doping of 3e16 cm^{-3} was demonstrated to be the optimum for balancing the need of lower off-state current and higher current gain β.

$I_{a\text{-}on}$ current (the blue curve) was easy to interpret: the active region current was exponentially dependent on the doping concentration. The doping level of 3e16 cm^{-3} was used as a boundary to separate the plot into two regions. The region with the doping concentration lower than 3e16 cm^{-3} was found to be undesirable for device operation due to high off-state current, especially for $I_{a\text{-}off}$. The band diagram for that doping level indicated an insufficient suppression of the valence band bump and resulted in a huge hole current passing through the bump. In the region with the doping concentrations higher than 3e16 cm^{-3}, $I_{g\text{-}on}$ was gradually going up. Meantime, the active region current was decreasing, which indicated a decrease of the current gain regardless of the decrease of both leakage currents $I_{a\text{-}off}$ and $I_{g\text{-}off}$ in the off state. Finally, the gate doping level of 3e16 cm^{-3} was chosen to calculate the current gain and the current on/off switching ratio.

Selection of the doping concentrations in two barriers weas carefully examined. In each barrier, a fully depleted region was required for an efficient control of the current switching. It was found that in the on state the valence band of the barrier does not create a bump to block the

hole transport. The first barrier satisfied the requirements under no intentional doping or a low doping of ~1e16 cm^{-3}. It showed 800 times higher I_a current leakage in the off state if the doping concentration was further increased to the level of 1e17 cm^{-3}. A low p-type doping of the barrier was found to be preferrable from the experimental results on a similar single-barrier heterostructure photodetector with InAsSb-based absorber [57]. In these experiments the devices with undoped AlInSb barriers layer exhibited slightly n-type background concentration. These devices had a five orders of magnitude greater dark current density than those with a 1e16 cm^{-3} Be-doped barriers at the bias of 0.4 V. The second barrier had a p-type doping of 1e17 cm^{-3} in a view of the raising up the valence band potential. This way, the valence band energies in the second barrier and the injector would be well-aligned. It was found to be an effective way to reduce the necessary V_{ig} for turning on the device because the bump in the second barrier was initially flattened with high p doping. Otherwise, the valence band level needed to be significantly pulled down for allowing holes to pass over the second barrier in the vertical direction.

As previously indicated, the gate doping of 3e16 cm^{-3} was found to be optimal. A summary of the simulation results is shown in Table 4-4. Although higher doping levels may seem to be attractive, experimental data often show that heavily doped III-V compounds have shorter Auger or SRH carrier lifetimes. As we know, Auger lifetime is inversely proportional to the square of the carrier concentration n^2. The gate layer with n-type donor concentrations of 6e16 cm^{-3} and 1e17 cm^{-3} would possibly have 4 and 10 times shorter lifetimes compared to that with the n-type doping level of 3e16 cm^{-3}. It would further result in a higher gate recombination current and a lower active region current. Besides, the current density in the active region would

be lower than 1000 A/cm^2 for the doping level higher than 6e16 cm^{-3}, which also had a negative impact on the device performance.

Table 4- 4. Summary of currents and current gain under various gate doping levels.

Doping (cm^{-3})	Contact Area (μm^2)	$J_{a\text{-}on}$ (A/cm^2)	$J_{a\text{-}off}$ (A/cm^2)	$J_{g\text{-}on}$ (A/cm^2)	$J_{g\text{-}off}$ (A/cm^2)	Current Gain $I_{a\text{-}on}$ / $I_{g\text{-}on}$
1e16	20 × 20	2.13e3	3.85e2	2.00e0	4.25e-1	1.06e3
3e16	20 × 20	1.66e3	2.44e-1	6.43e-1	5.68e-2	2.58e3
6e16	20 × 20	1.06e3	5.15e-2	6.25e-1	1.93e-2	1.70e3
1e17	20 × 20	6.13e2	2.02e-2	8.13e-1	8.48e-3	7.54e2
3e16	200 × 200	1.18e3	2.39e-1	1.58e-1	5.55e-2	7.47e3

To make it more convincing, we took a further step to make a comparison between a regular contact area 20×20 μm^2 and an enlarged contact area of 200×200 μm^2 described as the 2nd and 5th cases in the table. The thicknesses of each layer in the vertical direction remained unchanged. Comparing these two cases, the current densities in the off state agreed with each other. In the on state, the device with a larger contact area had smaller current densities in both the active and the gate regions. This is due to a limited hole mobility in InAsSb that constrained the current from spreading over large areas.

The 2D current densities and the concentration distributions were also studied. In Figure 4-10, the L-shape represents the geometry of the device, where the higher flat top is the injector contact and the lower one is the gate contact. The yellow region showed a high current density with 1600 A/cm^2 and 3000 A/cm^2 for electron current and hole current contributions, respectively. The right side of L-shape (rectangle) showed an ordinary current distribution in any barrier heterostructures, where the total current density of holes and electrons were supposed to

be constant. Due to the high potential spike at the interface of substrate and active region, the hole carriers cannot be collected by the substrate-side contact and hence transit into electron current by recombination process. A ridge in the current distribution was formed along the vertical direction. It is located between two contact pads at the lateral location of 20 μm - 25 μm.

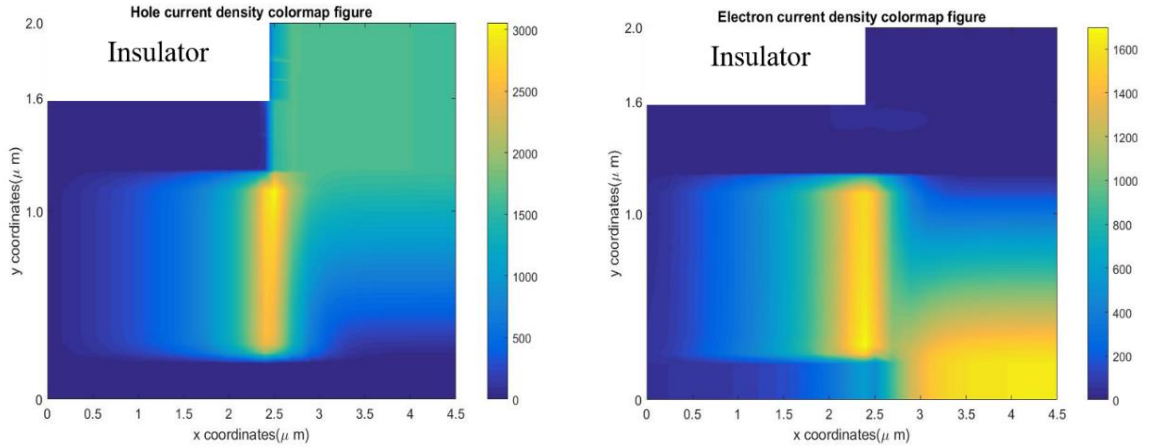

Figure 4- 10. Color map describing the current density distribution for hole and electron at on state.

A 2D modeling of the concentration gradient and the electric field was simulated for further analysis of the dominant current types. Figures 4-11 and 4-12 illustrate the results of modeling of the concentration and electric field in lateral direction of the active region.

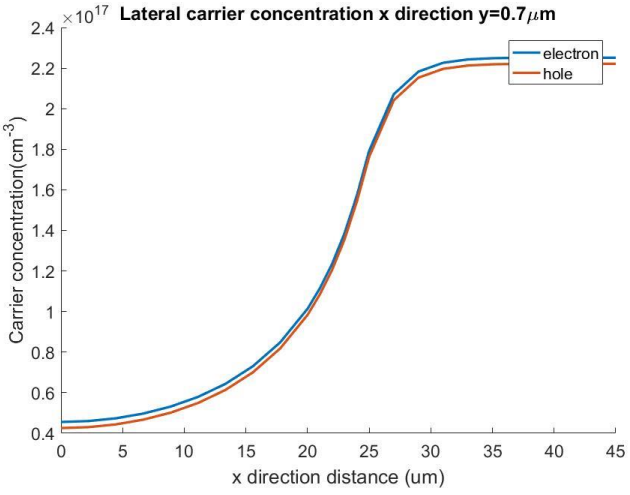

Figure 4- 11. Lateral electron and hole concentrations in the active region

A fast drop of both electron and hole concentrations occurred in the gap between two epi-side contact pads in the range of 20 μm to 25 μm laterally, causing a high concentration gradient in this region. It resulted in a large increase of the diffusion current due to high ∇n. At the same time, a moderate electric field by taking the derivative of the lateral potential was found in the same area across the active region, with a peak occurring at x = 24 μm. According to the current density equation,

$$J = qD\nabla n + \sigma E \tag{4.16}$$

where D is the diffusion coefficient and σ is the conductivity. Consequently, a large current was found in this region, and a 2D current density distribution also illustrated the ridge-shape occurrence in Figure 4-10.

The 2D concentration distributions for hole and electron were also studied as shown in Figure 4-13. Additionally, two cross-sections along the growth direction were taken at x = 25 μm and x = 45 μm in the center and at the edge of the device, respectively.

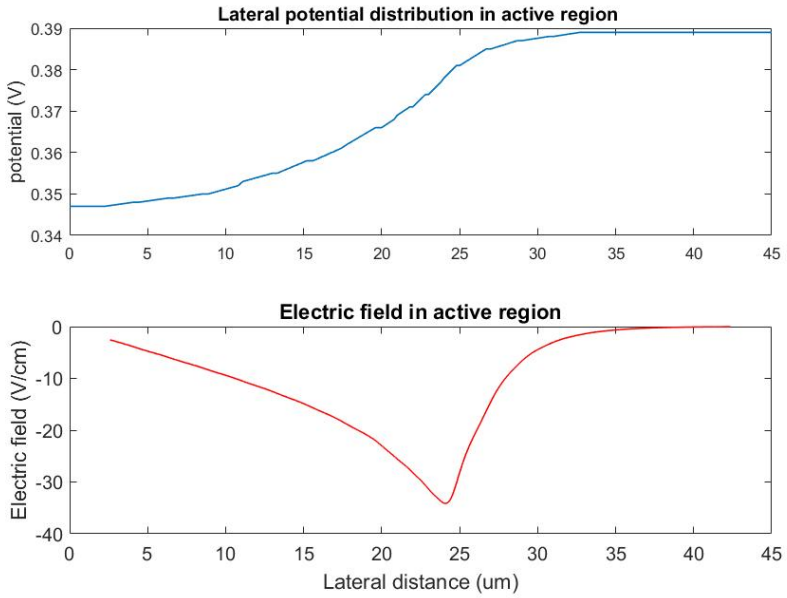

Figure 4- 12. Lateral potential distribution (top) and electric field (bottom) in the active region

Both hole and electron concentrations shown in Figure 4-14 were homogeneous in the active region (y = 0.2 – 2 μm), and the excess carrier concentration decreased by a 20 % from the center to the edge at x = 45 μm. A small curve of the electron concentration appeared in the range from 1.4 μm to 1.6 μm in the gate region, showing the electron concentration of 3e16 cm^{-3}. On the other hand, the hole concentration in the gate was only 3e15 cm^{-3}.

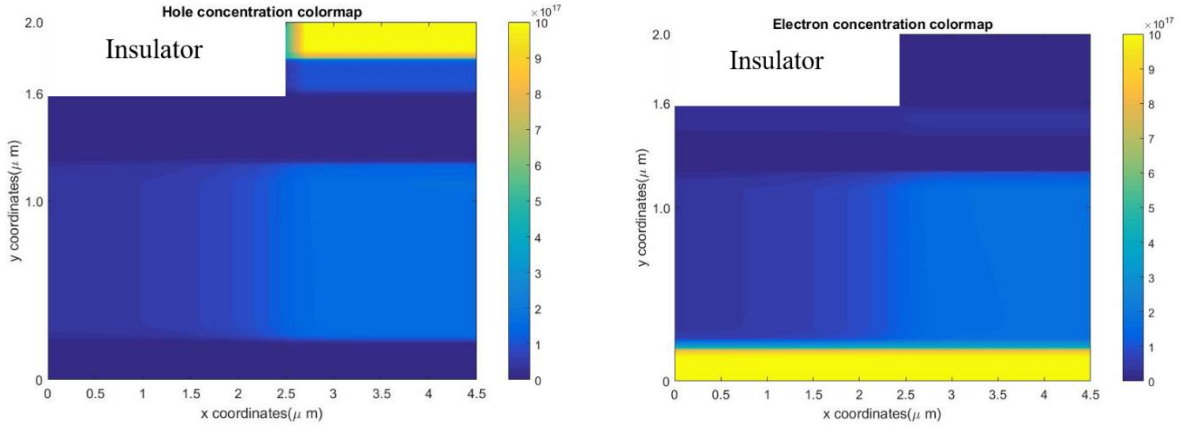

Figure 4- 13. Color maps for hole (a) and electron (b) concentration distribution at on state.

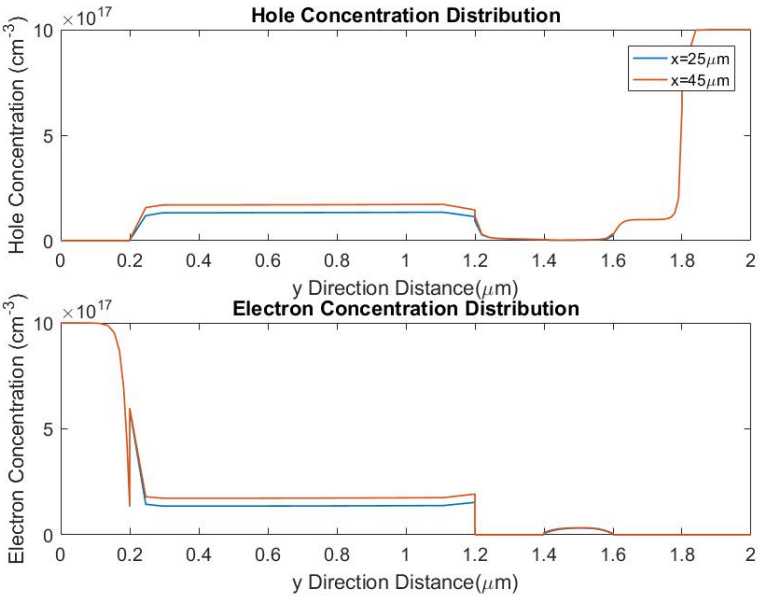

Figure 4- 14. cross-sections of hole and electron concentration distribution were taken at in the center (x = 25 μm) and at the edge (x = 45 μm) of the device.

With the minority hole lifetime of 200 ns, the gate recombination current was supposed to be less than 0.1% of the active region current as demonstrated above, reducing the power dissipation due to the control signal in the double-barrier heterostructure device. The yellow region in panel (a) showed a high hole concentration injected from the top electrode, while the yellow region in panel (b) showed a high electron concentration to be collected by the substrate contact.

4.5 Summary

In conclusion, we propose a novel optoelectronic device which consisted of the double barrier heterostructure. $InAs_{0.91}Sb_{0.09}$ and $Al_{0.80}In_{0.20}As_{0.24}Sb_{0.76}$ were used in the active region/gate/injector and the barriers, respectively. Both layers were latticed matched to GaSb substrate and had zero valence band misalignment. Modeling of a single device was completed in PADRE to analyze the band diagrams, I-V characteristics and 2D current/concentration distributions. The device design was optimized to achieve a microamp-scale control current, a high current gain of 2,580, a homogeneous concentration distribution. The active region current density of $J_a = 1.66x10^3$ A/cm^2 and the on/off current switching ratio $I_{i\text{-}on}/I_{i\text{-}off}$ = 5,600 were obtained, making this device suitable for MWIR LED or intensity light modulator arrays.

As integrating thousands of these single pixels into an array of multiplexed devices, the number of contacts can be greatly reduced by connecting the gate and the top injector contacts into columns and rows.

Chapter 5 GaAs detector arrays for soft X-ray beam position monitoring

5.1 Introduction

The soft X-ray scattering and spectroscopy are essential to advance the understanding and controlling the physics of emergent phenomena and catalysis at the nanoscale [108]. The Coherent Soft X-ray Scattering beamline (23-ID-1 or CSX) offers researchers state-of-the-art soft x-ray scattering and imaging tools with coherent, high-intensity photon flux to study the electronic texture and dynamics of composite materials. X-ray beam position monitors (XBPMs) are instrumental for storage ring light sources. It delivers the information of beam position and overtime stability to the researchers during the operation of the beamlines. The X-ray imaging resolution is limited due to the finite stability of the electron beam and photon beam. Meantime, the XBPMs should not invade into the beam core to distort the wavefront. Therefore, installing the high-resolution, non-invasive beam position monitors are critical in synchrotron light sources. The hard X-ray beam position monitors as a diagnostic tool have been established over a long time. However, such no-invasive XBPMs for soft X-ray beamlines do not exist. This is due to the soft X-ray has limited penetration capability and diffraction-limited wavefront.

We plan to demonstrate the first non-invasive soft X-ray beam position monitors (SXBPMs) based on a funded 3-year R&D project [109]. The imaging solution for SXBPMs is based on GaAs detector due to its mature manufacturing technology, ability to operate at high current density, and wide energy gap for temperature stability. The device must withstand high power under long-term exposure to the high-power ionizing radiation, operate in ultrahigh vacuum and preserve beam coherence. From beam diagnosis point of view, challenges such as 1) systematic errors by varying the insertion device gap and 2) contamination of stray radiation

[110] (dipoles, quadrupoles) that occur in the regular XBPMs [111,112] also need to be addressed in the novel device for coherent soft X-ray.

The topics in this thesis will cover 1) Design, fabrication of the GaAs photodiode arrays. 2) Algorithms for optimal detector positioning. Others including mechanical design of the test-stand, photodiode characterization and thermal analysis, readout integrated circuit (ROIC) will not be discussed.

5.2 Design, fabrication of GaAs photodiode array

The first prototypes of GaAs photodiode array are targeted for sensing the photon beam in the energy range of 250 eV – 2 keV defined as soft X-ray in CSX beamline. People may find a variation of soft X-ray range definitions in literatures [113–116]. The customized photodiode was composed of a shallow p-n junction grown by solid-source molecular beam epitaxy. The total thickness of epilayers was 0.4 μm. It is composed of a 0.2-μm Be-doped p-type layer on the top, and a 0.2-μm undoped n-type layer on heavily n-doped GaAs substrate. The p-type layer has the doping level variation of $2.5x10^{17}$ cm^{-3} (wafer D1711) and $8x10^{17}$ cm^{-3} (wafer D1710) determined by Van Der Pauw method from hall measurement. Based on the limit of ADC input current and wisdom of CSX beamline staff, the open window sizes of the photodiode array were decided to be 2x2 μm^2, 4x4 μm^2, 10x10 μm^2 and 60x60 μm^2 referred to as S, M, L and XL. Each has a corresponding pitch sizes of 10 μm, 20 μm, 30 μm and 125 μm.

The fabrication procedure is as following: The pattern of the mesas in four sizes were defined by photolithography and wet etching. The wafers were heated on the hot plate before spin coating to remove the moisture. The adhesion promoter was tried but not necessarily help the patterning of 2x2 μm^2 pixels. A new designed photomask for the processing of linear detector

array was shown in Figure 5-1 (b). Due to the small size of pixels, the wafer needed to dip into RD6 developer for 1 minute, which is two times longer than the regular developing for 50-μm scale pixels. The wet etcher used was H_3PO_4 : DI water : H_2O_2 = 60 mL : 30 mL : 30 mL plus 50 drops of NH_4F. Both wafers dipped for 3 s. The etching depth characterized by Dektak profiler was 500-700 nm.

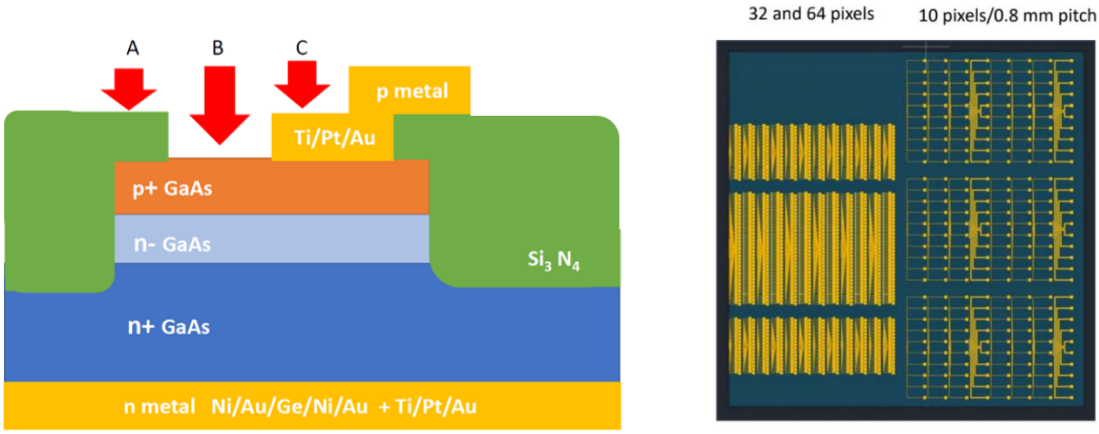

Figure 5- 1. (a) cross-section schematic of the p^+-n^--n^+ diode. (b) top view of the metal layout in the photomask.

For completely removing the negative photoresist, Qtip wiping was needed. Then wafters were treated by O_2 plasma two times for 10 min each to remove invisible photoresist residue. SiN dieletric layer with a thickness of 200 nm was deposited on the epi-side for 3 min by plasma-enhanced chemical vapor deposition (PECVD) for surface and sidewall passivation. A second round of photolithography was conducted for opening windows using the same negative photoresist NR71. SiN was removed by PECVD under the RF power of 100 W for 1.5 min, followed by 4-min O_2 plasma. Metallization of p-side and n-side contacts were made by e-beam deposition system. The n-side contact Ni/Au/Ge/Ni/Au was annealed by rapid thermal processor (RTP). Various recipes for GaAs annealing were proposed in previous works [117–119]. Annealing was studied for three cases: 1) one-time regular annealing at 420 ℃ for 15 s 2) twice

regular annealing at 420 ℃ for 15 s each 3) one-time regular annealing and an additional round of high temperature annealing at 460 ℃ for 30 s. The results were illustrated in Figure 5-2.

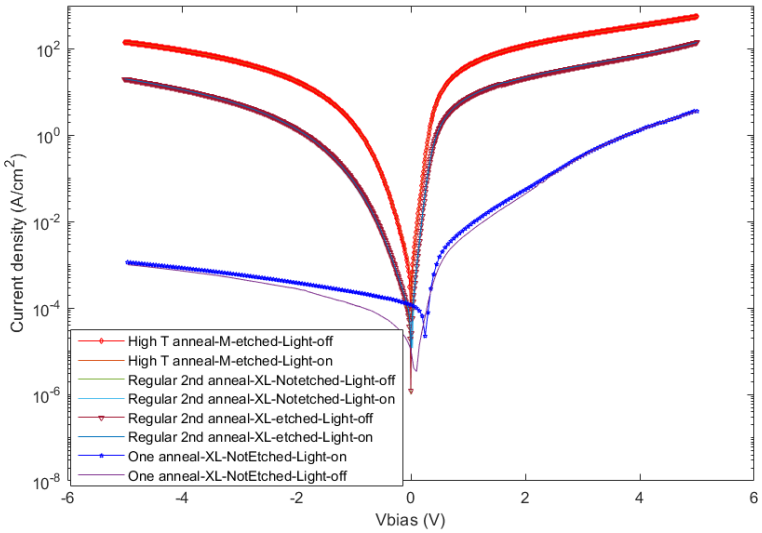

Figure 5- 2. Three annealing recipes were investigated and characterized by I-V characteristics.

As we can see, the 2nd round of annealing improved the current under forward bias. Annealing at higher temperature does not suppress the series resistance, instead it has negative impact on the reverse dark current. The annealing needs to be optimized further in order to suppress the reverse saturation current and reduce series resistance.

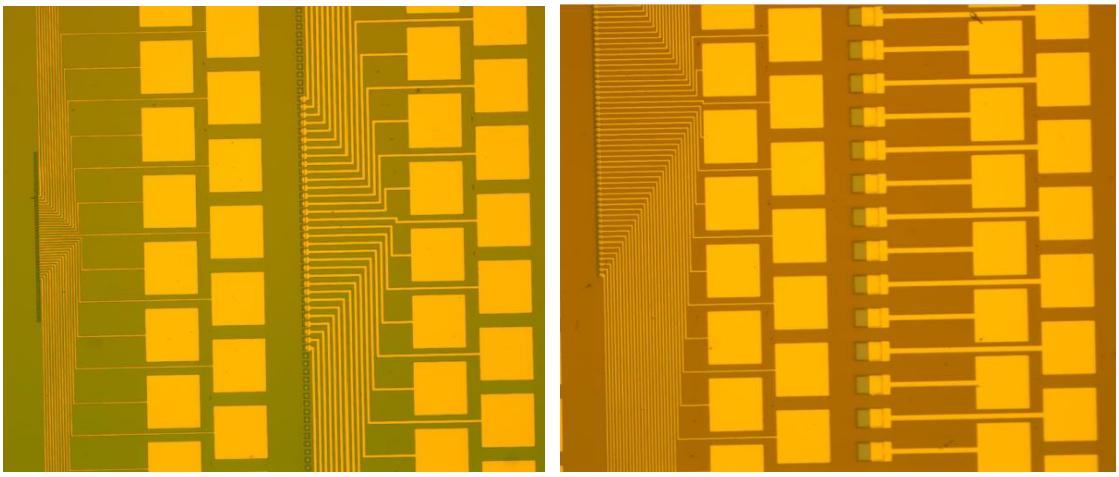

Figure 5- 3. Metal layout for S/L (left) and M/XL (right) pixels taken under microscope.

The processed wafers were cleaved into bars with 32 and 64 pixels and mounted in the leaded ceramic packages with indium solder for characterization with Ar-ion laser and for measurements of spectra responsivity in soft X-ray range at the CSX end-station. The 200x200 μm^2 metal pads were wired bonded to the package.

The shallow p^+n^- junction was chosen due to a stronger absorption of GaAs in soft X-ray compared to that in hard X-ray. The photons were expected to be absorbed in sub-micron range of the absorbing layer [115], thus surface recombination may become an issue [120]. According to the response measurement in the visible light range, the detector with lighter p-doping showed a reduction of photo responsivity due to the surface recombination and the poor carrier separation in built-in electric field near the surface. This Schottky barrier at metal-semiconductor interface impeded electrons from traveling towards the depletion layer. Moreover, the SiN-GaAs interface may also arise the surface leakage current and result in crosstalk between pixels.

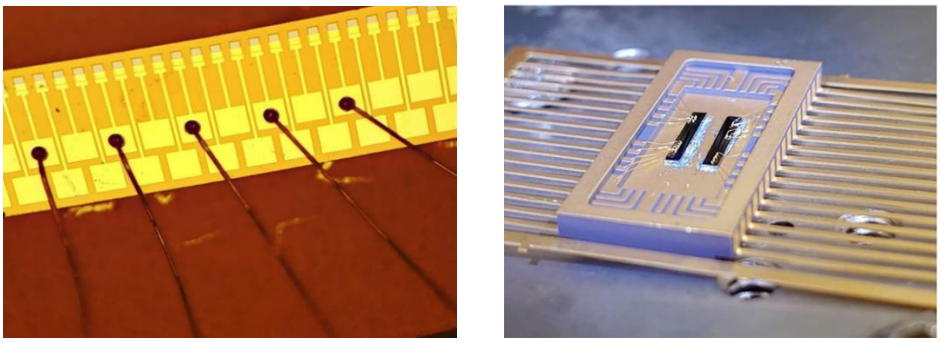

Figure 5- 4. (a) Photodiode arrays with 64 pixels and XL mesa. Metal pads were wire bonded to (b) the leaded ceramic carrier. Two cleaved bars were mounted with indium solder in the carrier.

5.3 Algorithm for optimal detector positioning

5.3.1 Overview

Due to the operation requirement from the beamline, photodiode arrays are movable and must completely extract from the X-ray beam. Having the flexibility in transverse positioning of

the detector arrays gives us an advantage in selecting the optimal detector position for best resolution as well as better immunity from synchrotron radiation contamination due to sources other than the target undulator. Because the size and shape of the photon beam varies greatly with undulator tunning these optimal detector positions are elliptical polarized undulator (EPU) gap- and phase-dependent. On the other hand, if we could show that the sXBPM achieves adequate performance without relying on detector repositioning for the entire range or even a sizable fraction of undulator tunning parameters, this would be of value for future SXBPM designs. Stationary detector arrays would allow to greatly simplify SXBPM mechanical design, reduce its cost and improve the reliability.

The resolution achieved by SXBPM, as well as its ability to discriminate stray radiation sources depend, among other factors, on the algorithm one uses to determine beam position from the detector signals. Multi-pixel detector arrays greatly enhance the choice and complexity of the algorithms one could use, potentially bringing significantly better performance.

Several algorithms of beam position determination were investigated. The conventional method of solving for beam position in BPMs is the difference-over-sum (DOS). DOS is applicable to either two or four sensors, placed symmetrical with respect to the x and y axis. Beam positions are found from the signals by using the equation $\frac{1}{S_{x,y}}\frac{U1-U2}{U1+U2}$, where Ui refers to the individual electrical signals from the sensors and Sx,y is the position sensitivity of one pair of sensors' arrangement with unit of [1/m] [121]. Difference-over-sum method is easy to implement and the error of position estimated by DOS is negligible if the beam displacement is much less than the beam sizes. However, there are limitations when using DOS. The position derived by DOS uses only 2 or 4 sensors, thus the accuracy of the algorithm is spatial dependent and can potentially be distorted by the noises arising from unwanted scattered light and electronic

circuitry. Multi-pixel arrays offer the flexibility of applying shape-fitting algorithms, such as [122] and [123]. These typically require an iteration procedure to derive the beam position, so it is more computationally expensive but proved to be more noise resistant in other applications [124]. Machine learning based algorithms could also be used in principle [125], especially if one needs to account for the effects that are hard-to-model, e.g. aging of the detectors, changes in electron beam size in the undulator, orbit changes, etc.

5.3.2 Constraints

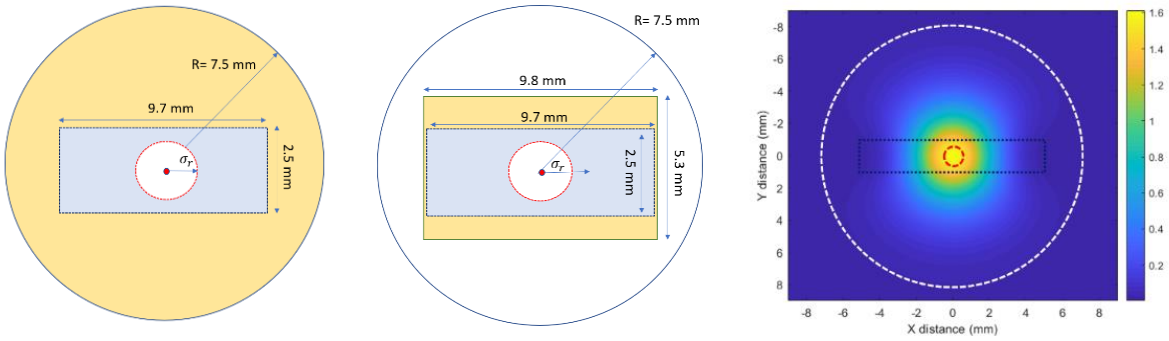

Figure 5- 5. the apertures along the CSX beamline are projected to 26 m downstream of undulator center considering two cases: (a) without a FOE fixed mask and (b) with a FOE fixed mask. It is composed of a circular fixed mask with radius of 7.5 mm and a rectangular slit aperture of 9.7 mm x 2.5 mm. The FOE fixed mask has a dimension of 9.8 mm x 5.3 mm. The dashed red circle represents the beam central cone for K = 0.4. (c) the undulator distribution for K=0.4 is simulated at 26 m downstream with the white dashed fixed mask and black dashed slit aperture.

In this section, the parameter space is defined for optimal array positioning analysis. First, we limit ourselves to linear horizontal polarized undulator radiation only. The idealized undulator distributions as a function of deflection parameter K are analyzed assuming no random noise and no contamination from the dipole radiation. Noise can affect this choice of position as well, but so far we did not find this important. Position is calculated assuming the detector signal is proportional to the total local incident power, i.e. the detector has a large spectral bandwidth well matched to the spectral content of the undulator radiation.

For simplicity, we assume two pairs of identical linear arrays, located symmetrically with respect to x or y axis. Four movable arms with the installed arrays have only linear motion, either horizontal or vertical, to approach the center of the beam. The placement is also constrained by the apertures along the CSX beamline. Figure 5-5 (a)-(b) show two configurations of the aperture projections at 26 m downstream of the undulator center, i.e. where the sXBPM test-stand will be located. At CXS beamline, a First Optics Enclosure (FOE) fixed mask located 0.8 m upstream of the SXBPM serves as an additional geometrical constraint of array positioning. For non-invasive measurement, arrays are placed in the yellow zone during beamline operation but outside the blue zone. Consequently, no space is available for left and right arrays for the configuration with FOE fixed mask. Locations ranging from 1.25 mm – 2.65 mm away from x axis is vertically available for top and bottom arrays.

However, by analyzing the objective function defined below, the FOE fixed mask has little effect on the calculation of the horizontal position from top/bottom detector arrays. It decreases the sensitivity of the vertical position measurement especially for the outer pixels for small K. However, pixels close to the array center should still provide adequate sensitivity.

The following analysis is focused on a more general configuration without the FOE fixed mask. Moreover, several SXBPM locations along the beam propagation direction are still being considered, and that transverse dimensions, found below scale proportionally.

The dynamic range of the analog-to-digital converter (ADC) reading the detector signals can potentially limit the minimal detectable signal due to beam displacement. Currently we assume the integration is performed with a 20-bit ADC. This should provide adequate precision to achieve micron-scale resolution for the entire K range from 0.4 to 3.458, provided the detectors are placed reasonably close to the optimal locations found below.

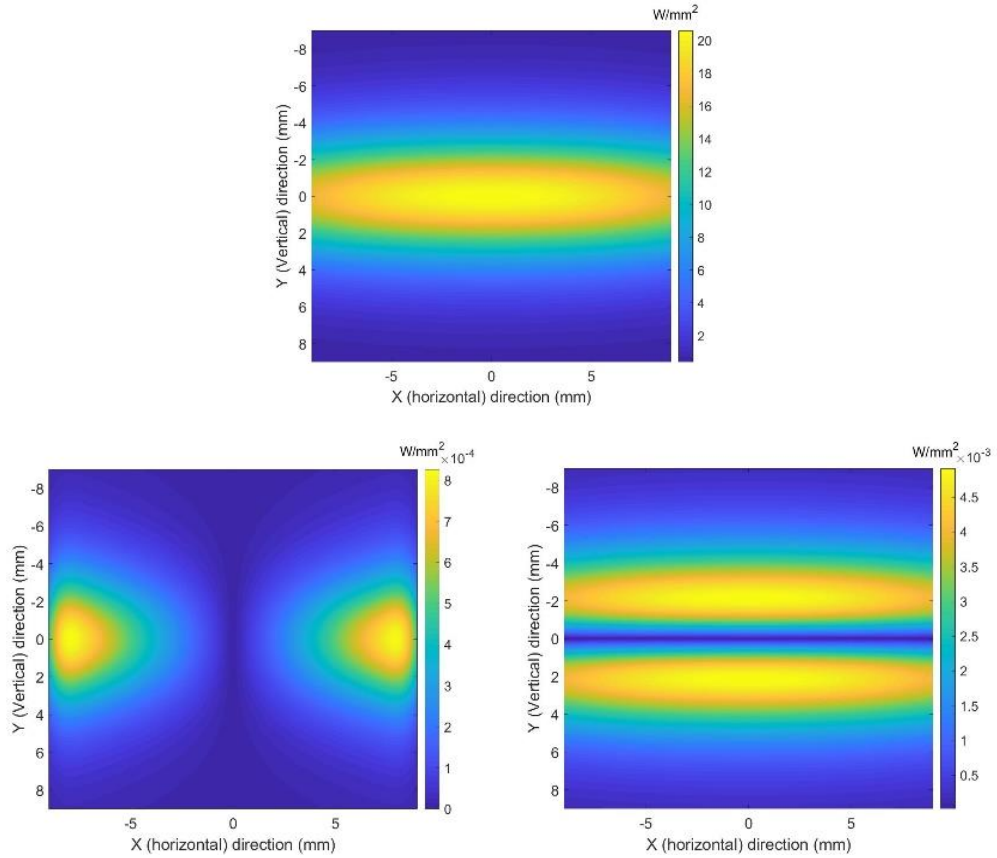

Figure 5- 6. (a) power density distribution of undulator radiation for K=3.458. The change of power density distribution due to 1-μm displacement in x direction (b) and in y direction (c). Horizontal and vertical positions are in mm scale and color bar shows the power density in W/mm^2.

5.3.3 Optimal diode array position analysis

In this section we investigate the optimal array placement as a function of undulator parameter K, limiting ourselves to the case of horizontal linear polarization. We also derive the optimal placement for the case of stationary detector arrays and estimate the performance degradation for this scenario.

First, the undulator radiation with the deflection parameter K=3.458 resulting in the first harmonic at 250 eV was evaluated. The beam profile, as well as its changes due to 1-μm displacement in x-direction and 1-μm displacement in y-direction were plotted in Figure 5-6. With larger deflection parameter or smaller undulator gap, the maximum power density change

in x-direction ΔP_x occurs beyond the edge of fixed mask. As K decreases, the total power goes down as K^2, the max power density change ΔP_x moves towards the beam center as the total power density shrinks in x direction. The position of max power density change in y-direction ΔP_y shows weak dependence on K, and stays relatively constant at 2 mm away from the beam center.

Assume that the photodiode arrays are 1D linear arrays positioned parallel to the x or y axis, the length of the arrays should be extended to the locations showing maximum sensitivity to beam displacements. To quantitively understand the optimal positions, the objective function $B(x, y)$ is defined as the ratio of change of power density $\Delta P(x, y)$ over slice maximum power density P_{max}, then converting to number of bits as follows,

$$B(x, y) = log_2\left(\frac{\Delta P(x,y)}{P_{max}}\right) \tag{5.1}$$

where the slice maximum power density is spatially dependent. Assuming that one detector array is positioned 4 mm to the left of the center, the P_{max} value is found among y in the range of -7.5 mm to 7.5 mm with x fixed at -4 mm. The reason for converting to binary is to confirm the change of signals is detectable in the full range of 20-bit ADC. The objective function describes number of bits at each location needed to sense the beam shift under a certain undulator configuration. Objective function is always negative since the change of the power density is smaller than the slice maximum power density, but more negative value means higher sensitivity of ADC required. That is why we are looking into the optimized objective function.

For the following analysis, the derivation of objective function is based on a fixed ADC full-scale range for each individual array for a given K. The range can be modified for each K and calibrated by the maximum slice power in each of the four arrays. Figure 5-7 shows two possible orientations of two diode array configurations for x and y beam displacements. The

corresponding 2D profiles of $B(x, y)$ are calculated as shown in Figure 5-8. A broad positioning area having a relatively constant signal located near the maximum of the objective function distribution, was identified in both lateral and vertical directions. Negative B is explained as the number of bits taken by ΔP that is lower than the maximum slice power density. For example, if the maximum slice power P_{max} takes the entire 20 bits, B = -16 indicates that ΔP is 16-bit smaller than P_{max} and takes 4 bits. Those B values beyond -20 are not detectable by ADC.

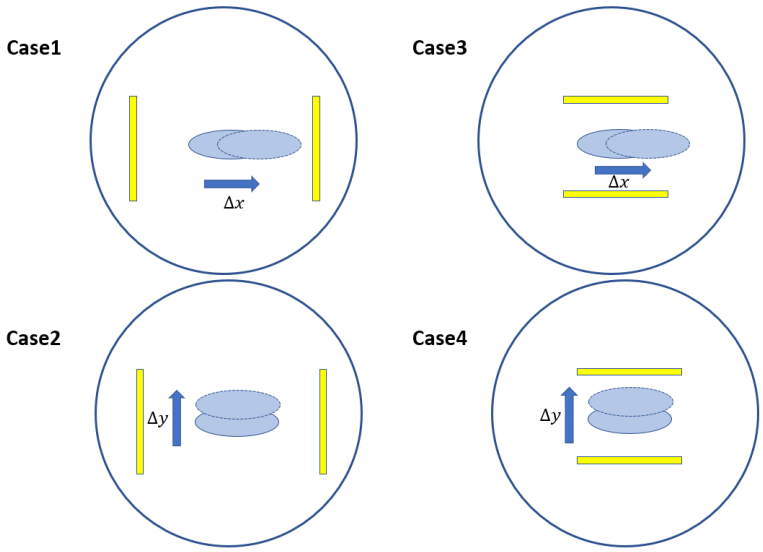

Figure 5- 7. four cases of beam displacement analysis: 1) left/right diode array arrangement. 2) top/bottom diode array arrangement. The x- and y- components for 1-μm displacement are addressed separately.

For all the deflection parameters ranging from 0.4 to 3.458, the smallest objective function occurs at K=3.458 under horizontal motion, which means higher sensitivity is required to resolve the beam displacement in this case. Compared to vertical motion using 7-9 bits in Figure 5-8 (b) and (d), the number of bits used in horizontal motion is 4-5 bits depending on the array arrangement as shown in Figure 5-8 (a) and (c). On the other hand, the top/bottom array arrangement is more tolerant to positioning than left/right arrangement due to a slow variation of objective function in y direction as shown in Figure 5-8 (c) and (d). Therefore, the optimal

position for left/right detector arrays were set to be 7.5 mm away, and top/bottom arrays were set to be 5.2 mm away from the center at K=3.458.

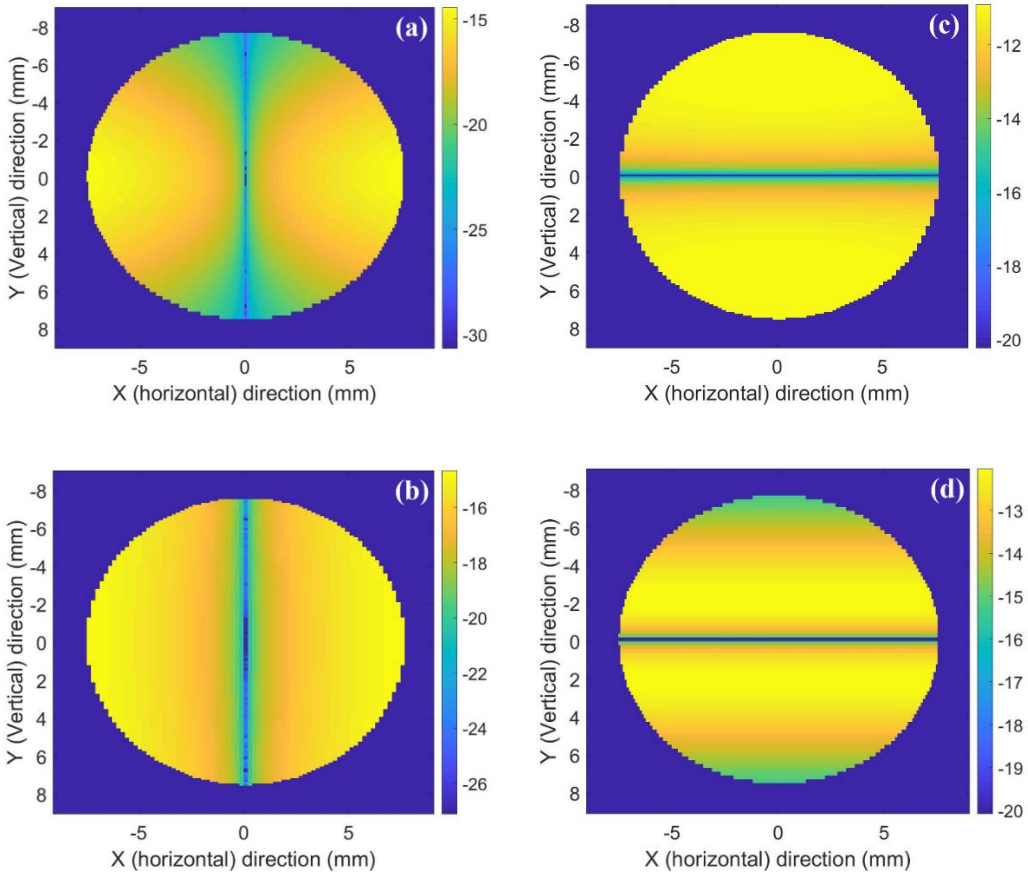

Figure 5- 8. Objective function $B(x,y)$ for the corresponding cases described in Figure 5-7. The deflection parameter is K= 3.458.

The optimal positions were then determined for deflection parameters of 1.978, 1.323, 0.864, 0.4 with corresponding first harmonics at 590 eV, 930 eV, 1270 eV, 1615 eV, respectively. The positions, summarized in Table 5-1, were found by locating the regions with the maximum power density change due to 1 micron beam shift for each case, then suggesting the optimal position of left/right and top/bottom detector arrays at each K.

Table 5- 1. optimal positioning in mm for variable deflection parameter K at 26 m downstream. Positions beyond the 7.5-mm radius of fixed mask and within 9.7 mm x 2.5 mm slit aperture are not accessible. Δx and Δy refer to 1-μm displacement along the axis respectively.

K	C1. Left/right array position considering Δx only	C2. Left/right array position considering Δy only	C3. Top/bottom array position considering Δx only	C4. Top/bottom array position considering Δy only	Optimal position for left/right array	Optimal position for top/bottom array
0.4	3.4	5.2	0	4.8	5.2	4.8
0.864	5.2	6.9	0	5.2	5.2-6.9	5.2
1.323	7.1	2.9	0	5.3	5.2	5.3
1.978	7.5	5.9	0	5.2	7.5	5.2
3.458	7.5	7.2	0	5.2	7.5	5.2

As K increases, the RMS horizontal beam sizes expand by four times, the optimal positions for left and right arrays considering horizontal motion (C1) monotonically move away from the beam center. Same trend applies to case 2 (C2) considering vertical motion for K above 1.323. In addition to the RMS horizontal beam sizes, the optimal positions in C2 are also influenced by the appearance of dumbbell-shape undulator radiation contour at K values below 1.323. That contour directly leads to the emergence of trident-shape features located symmetrically with respect to y axis as shown in Figure 5-9.

The optimal spots stay fixed for case 3 (C3) on x axis and the change of power density in this case also shows weak dependence on y. On-axis positioning is not suggested due to the existence of slit aperture, and such positioning is unable to derive the vertical displacement. Therefore, the determination of top and bottom arrays can be completely based on case 4 (C4), where the optimal positions are slightly varying near 5 mm.

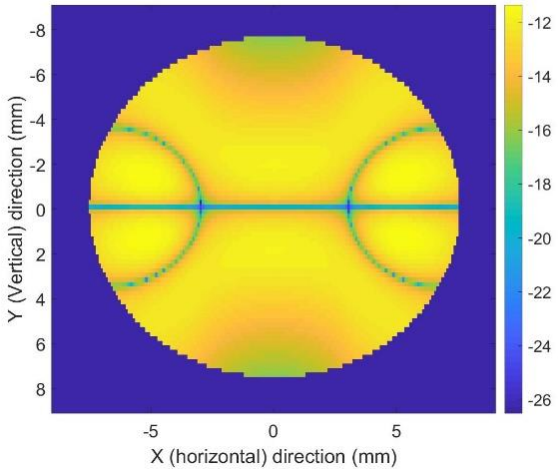

Figure 5- 9. Trident-shape dark field appears for K values below 1.323. Color bar represents the objective function $B(x, y)$.

Under compromised performance of the diode arrays, the placement of sXBPM could be further simplified by using two arrays only and/or fixing their positions without travel capabilities. Since the optimal position of the top and bottom pair is not very sensitive to the change of undulator gaps compared to that of the left and right pair. The x and y component of displacement can be obtained simultaneously by placing the top/bottom detector arrays only.

At large Ks, the horizontal distirbution of linear-polarized undulator radiation is flat and exhibits slow spatial variation. As a consequence, smooth distributions of objective function with shallow maximum are observed in both case 3 and case 4. Those locations close to y axis requires very high sensitivity due to the tiny change of power density at the peak of the undulator beam distribution. As arrays extend further away from y axis, the objective function B(x,y) becomes larger resulting in more number of bits available to detect the horizontal motion. Therefore, the length of the array should be long enough to reach the boundary of fixed mask. At smaller Ks, a comparable horizontal and vertical RMS beam sizes lead to similar power density change resolved by two pairs of arrays, the unique trident-shape feature under K = 1.323 also add the complexity of left/right array positioning optimization. Thus, in the entire K range

of interest, placing one pair of movable horizontal arrays instead of four arrays is a promising alternative solution, sacrificing at most 1-bit resolution of beam displacement.

5.3.4 Power distribution with finite spectral bandwidth

The power distribution was also studied for the finite spectral responsivity. The power distributions were studied in SPECTRA [126] and SRW [127] by applying a bandpass filter. Figure 5-10 illustrated two cases by the superposition of intensity profiles from 250 eV to 1 keV for panel (a) and from 250 eV up to 2 keV for panel (b). The intensity profiles were simulated in Jupyter hub, a module in Sirepo, where the source code was modified based on SRW simulation. The parameters in simulation are cited from the NSLS-II storage ring and ID-23-1 beamline.

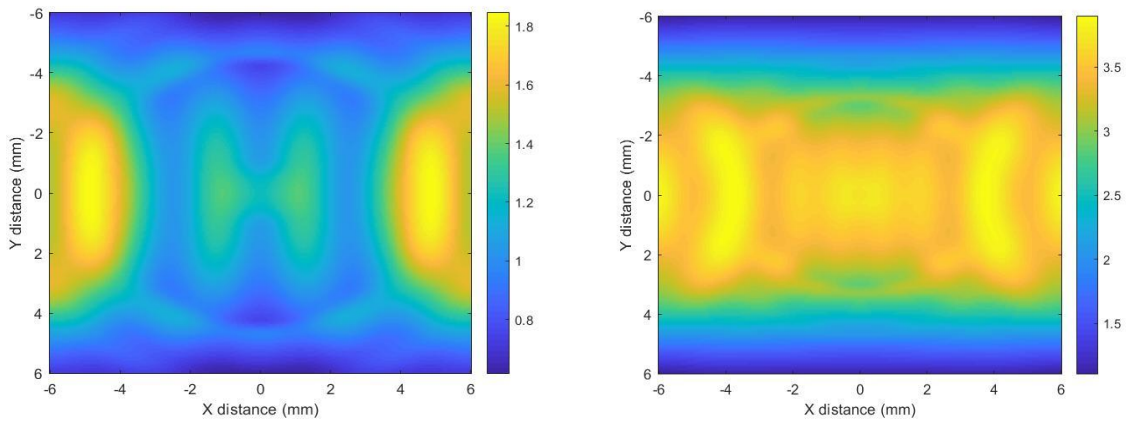

Figure 5- 10. The power density distribution simulated with a finite bandwidth from 250 eV to (a) 1 keV and (b) 2 keV. Color bar is in W/mm^2.

Fine features are observed in the power density profile with finite bandwidth. This may potentially affect the spatial resolution of beam displacement as well as the optimal positioning of diode arrays. The maximum power density reduces by 15 times for cut-off energy of 1keV and 7 times for cut-off energy of 2 keV. Most of the power is at higher frequencies. Moreover, softer photons mainly contribute to the power towards the outside of the beam, while harder photons establish the power in the center.

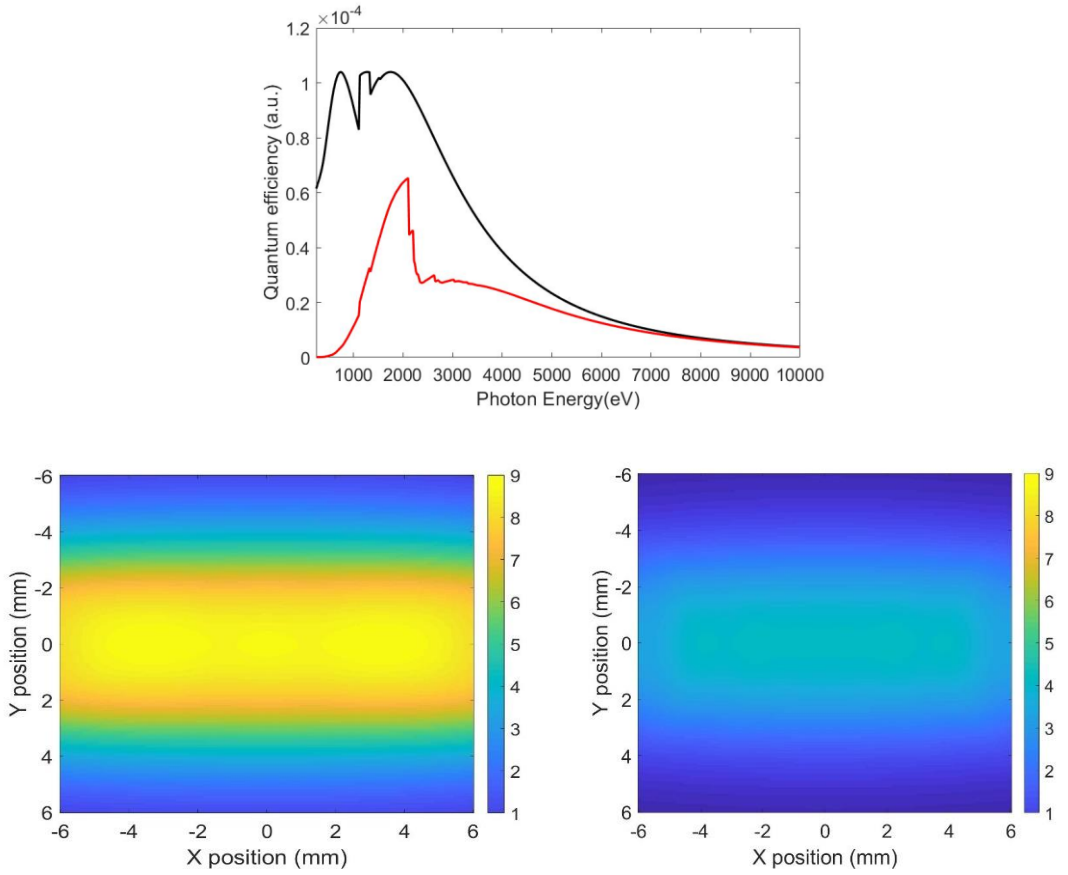

Figure 5- 11. (a) The quantum efficiencies for the shallow pn junction photodiode without (black) and with (red) Ti/Pt/Au metal alloys. We used them as band filters in SPECTRA and obtained the corresponding power distribution in (b) and (c), respectively. Color bar is in W/mm^2.

The modelled absorption spectrum [128] was applied to the analysis of spectral responsivity of GaAs photodiode. Three types of current were identified in shallow pn diode, including the electron diffusion current from p+ region, electron-hole drift current in the depletion region, and hole diffusion current generated in n+ region. Quantum efficiency was plotted as a function of photon energy in Figure 5-11 (a). It addressed two cases: 1) open GaAs surface and 2) GaAs with attenuation by Ti/Pt/Au n-side metal contact. It can be clearly seen that the entire spectrum is attenuated with the coating of n-side metal alloys.

These QE spectra were converted to transmission spectra, then applied as a band pass filter to calculate the spatial distribution of the beam power density detected by the arrays. The

simulation was complete in SPECTRA. Compared to the distribution with full bandwidth, fine features are observed in the power density profile with finite bandwidth. Due to narrowed spectral response, the detected power density is reduced by a factor of 4x because only soft X-ray part of the spectrum contributes to photocurrent. It facilitates for us to lower the photocurrent under long-term operation.

5.4 Summary and outlook

The project is underway at Brookhaven National Laboratory and Stony Brook University to demonstrate the first soft X-ray beam position monitor (SXBPM) based on GaAs photodiode array technology. The device is intended for use in soft X-ray beamlines in synchrotrons in high-power “white” X-ray beam. It must be non-invasive to the user experiments, so arrays are placed in the X-ray beam halo to preserve beam coherence. Meanwhile, it should provide micron-scale positional resolution and operate in ultrahigh vacuum. Photodiode arrays meeting the project goals have been designed and extensively simulated. The first detector array prototypes with up to 64 pixels have been fabricated and characterized with Ar-ion laser. Eight arrays have been packaged in ceramic and shipped to BNL to be tested in soft X-ray beam at CSX end-station.

Due to the geometrical constraints from the upstream of the SXBPM location, the detectors must be placed inside the FOE fixed mask but outside the slit aperture. Beside the traditional difference-over-sum method, new algorithms for beam position calculation are under development to take full advantage of extended multi-pixel arrays.

For the next iteration of the detector design, AlGaAs cap layer lattice matched to GaAs is under consideration. It can shrink the potential barrier near the surface. In this way, one type of carriers should dominant the transport and the dark current can be effectively reduced. For the

development of algorithms, deterministic fitting algorithms can be investigated first, followed by the attempt of implementing artificial neural networks (ANNs). For the advancement of optimal detector positioning, factors including the contamination of stray radiation, random noises, variation of detector sensitivity should be taken into account.

Appendix I Analytical solution of transient drift-diffusion

A 1D analytical solution of transient drift-diffusion model is used in Section 2.2.4 as a comparison to the COMSOL model. The resultant minority hole lifetimes had a good agreement within the two models.

According to Ref. [50] Section VI, the analytical solution of Green's function recorded in Appendix I is suitable for undepleted sensors, where the recombination term $\exp(-\frac{t}{\tau})$ should be taken into account in addition to the 1D diffusion equation. The boundary conditions are adjusted as Neumann boundary for the backside and Dirichlet boundary for the frontside. The origin of coordinated is set be at the frontside contact.

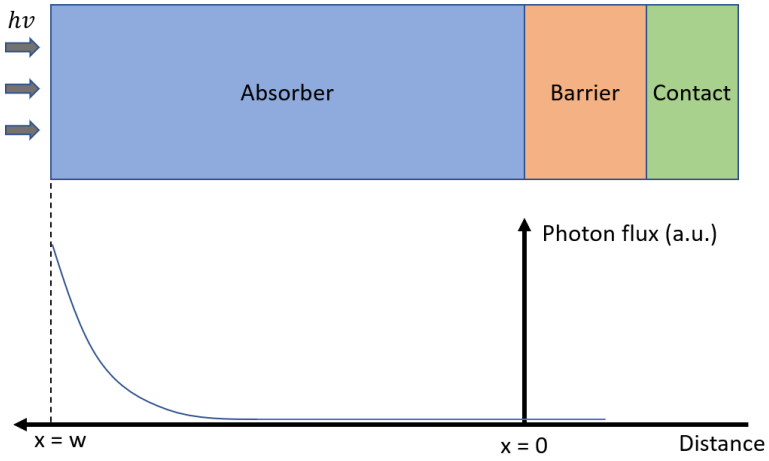

Figure AI- 1. Schematic of nBn heterostructure with backside illumination. The photon flux excitation shows an exponential decay. Full photon absorption is achieved at 2-μm wavelength.

The initial condition is the steady-state solution for backside illumination. This condition is applicable when we had square-wave modulated laser signal in the transient response measurement. The factor exp(-ax) should be considered for the photon absorption. Several steady-state (SS) solution examples can be found from Refs. [48,49], and all of them start from the standard form of continuity equation,

$$\frac{d^2p}{dx^2} - \frac{p}{L^2} = \frac{F_0\alpha\exp\left(-\alpha(w-x)\right)}{D} \quad (1)$$

where L is the diffusion length and D is diffusion coefficient. F_0 is the photon flux with the unit #/cm^2/s. The absorption dependence $\exp\left(-\alpha(w-x)\right)$ is plotted in Figure 1. As mentioned before, x = 0 is the frontside contact, x = w is the backside window. w is the layer thickness of the absorber, i.e. 2 μm in the nBn heterostructure photodetector.

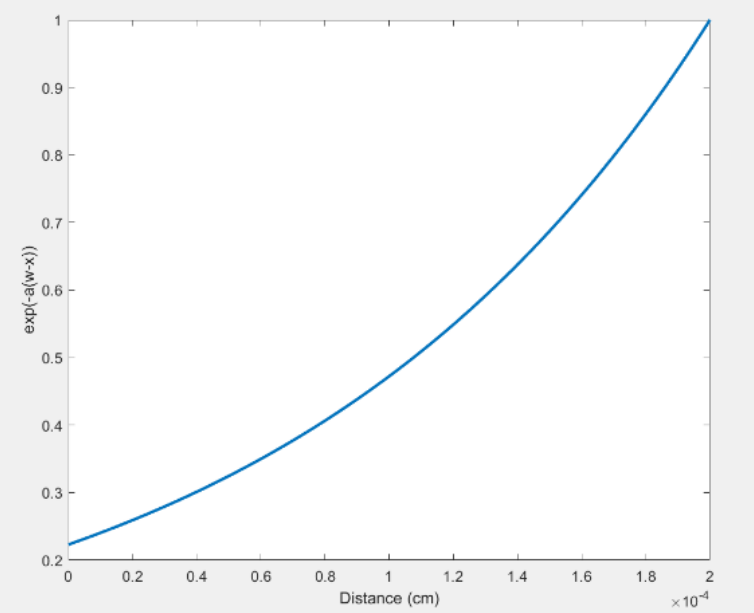

Figure AI- 2. The absorption factor exp $(-\alpha(w-x))$ for the case of backside illumination

The boundary conditions for SS solution must agree with those for transient response, using $p(x)|_{x=0}$= 0 to represent the front contact sinking all the carriers and $\frac{dp(x)}{dx}\Big|_{x=w} = 0$ for the backside. The solution for SS is as follows,

$$p(x) = Aexp\ (\alpha x) + Bexp\left(\frac{x}{L}\right) + Cexp\left(-\frac{x}{L}\right) \tag{2}$$

$$\begin{cases} A = \dfrac{F_0(1-R)\alpha L^2 exp\ (-\alpha w)}{D(\alpha^2 L^2 - 1)} \\ B = \dfrac{-F_0(1-R)\alpha L^2 exp\ (-\alpha w)}{D(\alpha^2 L^2 - 1)}\left(\dfrac{exp\left(-\frac{w}{L}\right) + \alpha L exp(\alpha w)}{2cosh\left(\frac{w}{L}\right)}\right) \\ C = \dfrac{F_0(1-R)\alpha L^2 exp\ (-\alpha w)}{D(\alpha^2 L^2 - 1)}\left(\dfrac{\alpha L exp(\alpha w) - exp\left(\frac{w}{L}\right)}{2cosh\left(\frac{w}{L}\right)}\right) \end{cases}$$

The distribution of hole concentration is shown in Figure AI-3, where the concentration quickly drops to zero near the frontside contact and exhibits greater magnitude but less than the electron concentration (low-injection limitation) near the rear window.

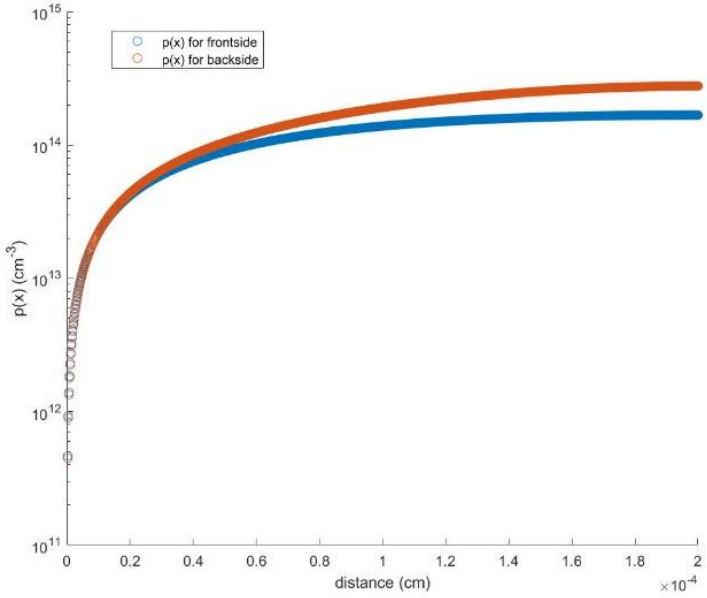

Figure AI- 3. Examples of p(x) in steady-state solution for frontside (blue) and backside (red) illumination.

Next step is to solve Green's function with approriate boundary conditions and initial condition. The initial condition is p(x,0) as shown in the below equation sets. The recombination term written as $\gamma p(x,t)$ can be separated from the standard form of 1D diffusion equation therefore we get the term $e^{-\gamma t}$ in the analytical solution. γ is reciprocal of lifetime.

$$\begin{cases} \dfrac{\partial p(x,t)}{\partial t} = D\nabla^2 p(x,t) - \gamma p(x,t) \\ p(x,0) = Aexp(\alpha x) + Bexp\left(\dfrac{x}{L}\right) + Cexp\left(-\dfrac{x}{L}\right) \end{cases} \tag{3}$$

$$p(x,t) = u(x,t)e^{-\gamma t} \tag{4}$$

The diffusion equation can be further simplified as,

$$\frac{\partial u(x,t)}{\partial t} = D\nabla^2 u(x,t) \tag{5}$$

On the interval $x \in [0, w]$, the boundary conditions are,

$$u(0,t) = 0 \tag{6}$$

$$\frac{\partial u(w,t)}{\partial x} = 0 \tag{7}$$

The initial condition $f(x)$ also could be simplified as,

$$u(x,0) = f(x) = Aexp(\alpha x) + Bexp\left(\frac{x}{L}\right) + Cexp\left(-\frac{x}{L}\right) \tag{8}$$

irrelevant to t. Then separation of variables,

$$u(x,t) = X(x)T(t) \tag{9}$$

All the following procedures [129], substituting u back to Equation 5,

$$\frac{1}{D}\frac{T'(t)}{T(t)} = \frac{X''(x)}{X(x)} = -\lambda \tag{10}$$

$$X''(x) + \lambda X(x) = 0 \tag{11}$$

$$T'(t) + D\lambda T(t) = 0 \tag{12}$$

Boundary condition from Equation 6-7 can be written as

$$u(0,t) = X(0)T(t) = 0 \rightarrow X(0) = 0 \quad (13)$$

$$\frac{du(w,t)}{dx} = X'(w)T(t) = 0 \rightarrow X'(w) = 0 \quad (14)$$

Solving linear ODE and the case for $\lambda > 0$:

$$X(x) = K1\cos\left(\sqrt{\lambda}x\right) + K2sin\left(\sqrt{\lambda}x\right) \quad (15)$$

Substitute boundary Equation 13,

$$X(0) = K1 = 0$$

Boundary Equation 14,

$$X'(w) = K2\sqrt{\lambda}\cos\left(\sqrt{\lambda}w\right) = 0 \ \rightarrow \ \lambda = \left(\frac{n\pi}{2w}\right)^2 \quad n = 1,3,5, \ldots \ldots$$

Hence,

$$X(x) = K2sin\left(\frac{n\pi}{2w}x\right)$$

From Equation 12,

$$T'(t) + D\left(\frac{n\pi}{2w}\right)^2 T(t) = 0 \ \rightarrow \ T(t) = Mexp\left(-D\left(\frac{n\pi}{2w}\right)^2 t\right)$$

The general solution of 1D diffusion Equation 5 can be written as,

$$u(x,t) = \sum_{n=1}^{\infty} A_n sin\left(\frac{n\pi}{2w}x\right)\ exp\left(-D\left(\frac{n\pi}{2w}\right)^2 t\right) \qquad n = 1,3,5, \ldots$$

If the initial condition is not a delta function but rather a distribution described as a SS solution, the convolution of distribution function $f(x)$ and the above equation u(x,t) are needed,

$$f(x) = \sum_{n=1}^{\infty} F_n sin\left(\frac{n\pi}{2w}x\right) = \sum_{n=1}^{\infty} A_n sin\left(\frac{n\pi}{2w}x\right),$$

Apart from the regular case [129], the series only contains odd number terms with n = 1,3,5,…..

$$A_n = F_n = \frac{1}{w}\int_0^{2w} f(\xi)sin\left(\frac{n\pi}{2w}\xi\right)d\xi \quad n = 1,3,5 \ldots.$$

$$\boxed{u(x,t) = \sum_{n=1}^{\infty}\frac{1}{w}\int_0^{2w} f(\xi)sin\left(\frac{n\pi}{2w}\xi\right)d\xi\ sin\left(\frac{n\pi}{2w}x\right)exp\left(-D\left(\frac{n\pi}{2w}\right)^2 t\right) \qquad n = 1,3,5 \ldots}$$

Later we need to take the derivative over x, and the whole integral is not with respect to x, so it can be treated as a constant and depends on n. The integrals are solved as three parts:

$$\int_0^{2w} f(\xi)sin\left(\frac{n\pi}{2w}\xi\right)d\xi = \int_0^{2w}\left[Aexp(\alpha\xi) + Bexp\left(\frac{\xi}{L}\right) + Cexp\left(-\frac{\xi}{L}\right)\right]sin\left(\frac{n\pi}{2w}\xi\right)d\xi$$
$$= I_{1n} + I_{2n} + I_{3n}$$

Part1 I_{1n}:

$$\int_0^{2w} Aexp(\alpha\xi)sin\left(\frac{n\pi}{2w}\xi\right)d\xi = \frac{2Aw(e^{2aw}(2aw\ sin(n\pi) - n\pi\cos(n\pi)) + n\pi)}{4a^2w^2 + n^2\pi^2}$$

Part2 I_{2n}:

$$\int_0^{2w} Bexp\left(\frac{\xi}{L}\right)sin\left(\frac{n\pi}{2w}\xi\right)d\xi = \frac{2BLw(e^{2w/L}(2\mathrm{w}\sin(n\pi) - n\pi L\cos(n\pi)) + n\pi L)}{n^2\pi^2L^2 + 4w^2}$$

Part3 I_{3n}:

$$\int_0^{2w} Cexp\left(-\frac{\xi}{L}\right)sin\left(\frac{n\pi}{2w}\xi\right)d\xi = \frac{2CLwe^{-2w/L}(n\pi Le^{2w/L} - n\pi L\cos(n\pi) - 2w\sin(n\pi))}{n^2\pi^2L^2 + 4w^2}$$

Finally, the diffusion current is calculated by the first derivative,

$$J_{diff} = qD\frac{\partial p(x,t)}{\partial x}\Big|_{x=0} = qD\frac{\pi}{2w^2}exp\left(-\frac{t}{\tau}\right)\sum_{n=1}^{\infty} n(I_{1n} + I_{2n} + I_{3n})\ exp\left(-D\left(\frac{n\pi}{2w}\right)^2 t\right)$$

$$n = 1,3,5 \ldots$$

The drift current component in the absorber is negligible due to the suppressed depletion region in the two narrow bandgap regions of the barrier heterostructure. The derived diffusion current equation was scripted in MATLAB and used for the analysis of the minority hole lifetimes. The transient decays with single slopes were plotted in Figure AI-5.

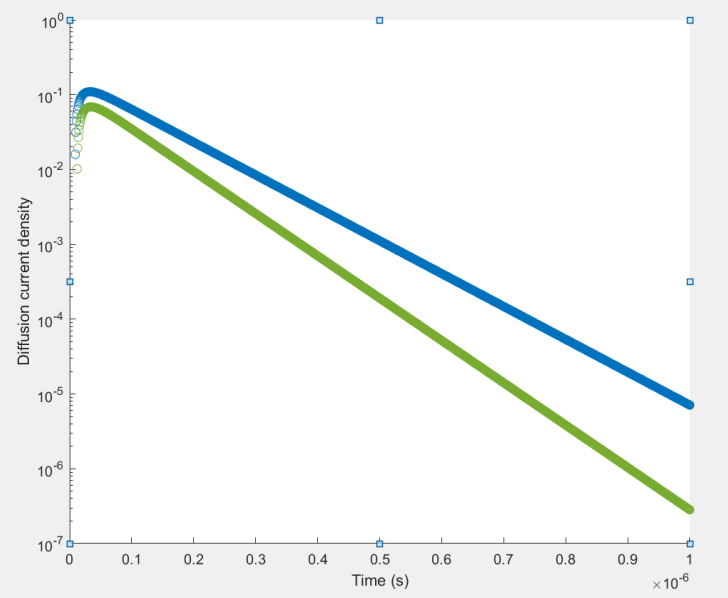

Figure AI- 4. Examples of the transient response as a function of time, where the identified single slope represents the reciprocal of the minority hole lifetime. This slope was used for the analysis of experimentally determined transient response.

Appendix II Kramers-Kronig relations

Kramers-Kronig (KK) relations is a formula that shows the relationship between the real and imaginary part of one physical parameter. It is mostly used in calculating optical or electromagnetic parameters, e.g. real and imaginary part of the dielectric constant ε, susceptibility χ; Refractive index n with extinction coefficient κ. By taking the integral of one of the parameters, typically the one that can be easily obtained from experiment, people can estimate the other parameter of the pair. If there are no singularities on the upper half plane (UHP), the integral should bypass all the singularities along the axis to form a closed loop on UHP. Thus, how to deal with those singularities becomes important for obtaining the accurate integration results in the numerical calculation of KK relations.

In Chapter 3, the change of refractive index was derived based on the experimentally determined absorption spectrum. Firstly, determine the integral for refractive index n as a function of absorption coefficient alpha,

$$n(\omega) = 1 + \frac{2}{\pi} P \int_0^{+\infty} \frac{\omega' \kappa(\omega')}{\omega'^2 - \omega^2} d\omega' \quad (1)$$

where $n(\omega) - 1$ and the extinction coefficient $\kappa(\omega)$ have KK relations, and $a = 2\omega\kappa/c$. P denotes Cauchy Principal Value (CPV), and sometimes people also use a dash across the integral symbol for the same intent. By applying the parameters into the integral in Equation 1, it is easy to derive Equation 2, where Ω and ω are angular frequencies of photons.

$$n(\omega) = 1 + \frac{c}{\pi} P \int_0^{+\infty} \frac{\alpha(\Omega)}{\Omega^2 - \omega^2} d\Omega \quad (2)$$

The overall integral is easy to compute except for the value near the singularity. Next, we need to evaluate how to solve the integral in the range of the singularity point $\Omega = \omega$. A variable $\delta \to 0$ is defined since we are only interested in the integral in the range of $\omega - \delta$ to $\omega + \delta$. One possible solution is Taylor series as indicated in Ref. [86]. The resultant integral near the singularity $\Omega = \omega$ is,

$$n'(\omega) = \frac{c}{\pi}\left[P \int_{\omega-\delta}^{\omega+\delta} \frac{\alpha(\Omega)}{\Omega^2 - \omega^2} d\Omega\right] = \frac{c}{2\pi\omega}\left[-\int_{\omega-\delta}^{\omega+\delta} \frac{\alpha(\Omega)}{\Omega + \omega} d\Omega + 2\,\delta\alpha'(\omega) + \frac{1}{9}\delta^3\alpha'''(\omega)\right] \quad (3)$$

The details of the derivation of Kramers-Kronig relations are recorded as following.

Interpolation and Extrapolation: Interpolation was applied to the experimental absorption spectrum within the photon energy range. In this way, a smaller interval of δ was created, resulting in higher accuracy of the numerical estimation near ω. The other attempt was done in the extrapolation of the data to a high photon energy range. A constant absorption coefficient was assumed for the extrapolation. The result of the extrapolation indicated less than 5% change of the refractive index n by taking the integral of the absorption over angular frequency square in Equation 2.

Moreover, the chosen interpolation is always a multiple of 2. This can be referred to Ref. [86] as a way of converting integral (continuous) to series (discrete) by taking the value of middle point $\alpha(\omega_k + h/2)$ in each interval of $\omega_k \sim \omega_{k+1}$.

The derivation can start from the denominator,

$$\frac{1}{\Omega^2 - \omega^2} = \frac{1}{(\Omega + \omega)(\Omega - \omega)} = \frac{1}{2\omega}\left(\frac{1}{\Omega - \omega} - \frac{1}{\Omega + \omega}\right)$$

Take the Cauchy Principal Value term from Equation 2, ignore the factor $\frac{c}{\pi}$,

$$P\int_a^b \frac{\alpha(\Omega)}{\Omega^2-\omega^2}d\Omega = \frac{1}{2\omega}\left[\int_a^{\omega-\delta}\frac{\alpha(\Omega)}{\Omega-\omega}d\Omega + P\int_{\omega-\delta}^{\omega+\delta}\frac{\alpha(\Omega)}{\Omega-\omega}d\Omega + \int_{\omega+\delta}^{b}\frac{\alpha(\Omega)}{\Omega-\omega}d\Omega\right] - \frac{1}{2\omega}\int_a^b \frac{\alpha(\Omega)}{\Omega+\omega}d\Omega \tag{4}$$

Let $\Omega-\omega=t$,

$$P\int_{\omega-\delta}^{\omega+\delta}\frac{\alpha(\Omega)}{\Omega-\omega}d\Omega = P\int_{-\delta}^{+\delta}\frac{\alpha(\omega+t)}{t}dt = \lim_{\varepsilon\to 0}\left[\int_{-\delta}^{-\varepsilon}\frac{\alpha(\omega+t)}{t}dt + \int_{+\varepsilon}^{+\delta}\frac{\alpha(\omega+t)}{t}dt\right]$$

Derive the Tayler series expansion of $\alpha(\omega+t)$,

$$\alpha(\omega+t) = \alpha(\omega) + \frac{\alpha'(\omega)}{1!}t + \frac{\alpha''(\omega)}{2!}t^2 + \frac{\alpha'''(\omega)}{3!}t^3 + \cdots$$

Calculate the first term from the Tayler series, where $\alpha(\omega)$ is a constant and the integral is also a CPV:

$$P\int_{-\delta}^{+\delta}\frac{\alpha(\omega)}{t}dt = 0$$

Second + Third term:

$$P\int_{-\delta}^{+\delta}\left(\alpha'(\omega)\frac{t}{t} + \frac{1}{2}\alpha''(\omega)\frac{t^2}{t}\right)dt = 2\delta\alpha'(\omega)$$

Fourth term:

$$P\int_{-\delta}^{+\delta}\frac{1}{6}\alpha'''(\omega)\frac{t^3}{t}dt = \frac{1}{9}\delta^3\alpha'''(\omega)$$

Finally, the derived four terms are applied in the integral term in Equation 4,

$$P\int_a^b \frac{\alpha(\Omega)}{\Omega^2-\omega^2}d\Omega = -\frac{1}{2\omega}\int_a^b\frac{\alpha(\Omega)}{\Omega+\omega}d\Omega + \frac{1}{2\omega}\left[\int_a^{\omega-\delta}\frac{\alpha(\Omega)}{\Omega-\omega}d\Omega + \int_{\omega+\delta}^{b}\frac{\alpha(\Omega)}{\Omega-\omega}d\Omega + 2\delta\alpha'(\omega) + \frac{1}{9}\delta^3\alpha'''(\omega)\right]$$

The next step is to convert the integral into a series to facilitate the scripting in MATLAB. The angular frequency ω was evenly separated into N intervals. Each interval has a size of $(\omega_n-\omega_1)/N$, and in practice N is ~1,000. The ω_n is corresponding to the highest photon energy (e.g. 550 meV), while ω_1 is corresponding to the lowest photon energy of the measured absorption spectrum (e.g. 52 meV for $InAsSb_{0.4}$).

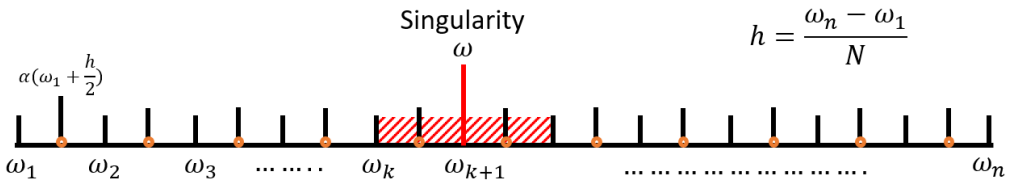

In each interval, the absorption coefficient is taken at the midpoint of the interval noted as $\alpha(\omega_k + \frac{h}{2})$, where h is the length of the interval. The series were categorized as ① the intervals excluding the singularity ω; ② the intervals including the singularity ω (Two intervals marked red). Again, from Equation 4,

$$P\int_a^b \frac{\alpha(\Omega)}{\Omega^2-\omega^2}d\Omega = \underbrace{\int_a^{\omega-\delta}\frac{\alpha(\Omega)}{\Omega^2-\omega^2}d\Omega + \int_{\omega+\delta}^{b}\frac{\alpha(\Omega)}{\Omega^2-\omega^2}d\Omega}_{①} + \underbrace{\frac{1}{2\omega}\left[-\int_{\omega-\delta}^{\omega+\delta}\frac{\alpha(\Omega)}{\Omega+\omega}d\Omega + 2\delta\alpha'(\omega) + \frac{1}{9}\delta^3\alpha'''(\omega)\right]}_{②}$$

$$① = \sum_{i=1}^{n-1}\frac{\alpha(\omega_i+\frac{h}{2})}{(\omega_i+\frac{h}{2})^2-\omega^2}(\omega_{i+1}-\omega_i) \qquad i \neq k, k+1$$

$$② = \frac{1}{2\omega}\left[-\frac{\alpha(\omega_k+\frac{h}{2})}{\omega_k+\frac{h}{2}+\omega}(\omega_{k+1}-\omega_k) - \frac{\alpha\left(\omega_{k+1}+\frac{h}{2}\right)}{\omega_{k+1}+\frac{h}{2}+\omega}(\omega_{k+2}-\omega_{k+1}) + 2\delta\alpha'(\omega) + \frac{1}{9}\delta^3\alpha'''(\omega)\right]$$

$$\delta = \omega_{k+1} - \omega_k$$

To summarize, Kramers-Kronig relations are derived for the parameter pair of the real refractive index and the absorption coefficient. The value near the singularity is a Cauchy Principal Value. This value can be estimated by Taylor series expansion. The resultant CPV is minimized if the interpolation of the absorption spectrum is applied. In the numerical integration, if the step size for ω is chosen small enough to obtain the integral value from $\omega - \delta$ to $\omega + \delta$, the integration $n'(\omega)$ near the singularity can be less than 0.1 % of $n(\omega)$ in the rest of the absorption spectrum.

Appendix III A brief guide to PADRE simulation tool

PADRE is a user-friendly framework for one-dimensional to three-dimensional device simulation. It was created for the simulation of the semiconductor devices, including PN diode, BJT and other field-effect transistors. It is capable of simulating the device electrical behaviors under equilibrium, steady state and transient conditions and AC analysis. The fundamental model of PADRE is drift-diffusion model, which is one of the most popular semi-classical models. An online free browser-based version and a Linux-based version are available. Appendix III is initiated from my experience of using Linux-based PADRE and the techniques are summarized as a brief guide to PADRE simulation. The manual can be found at Refs. [103,130–132]. The command library can be found at Ref. [133].

Like many other software, the syntax of PADRE can be edited as an ASCII text file using text editors. The syntax format is as following,

<Statement> <Parameter> = <Value>

There are a full-length version and an abbreviated version of a single Statement. Details can be referred to the command library. The input text starts from the definition of mesh, geometrical region, electrode and doping. In a 2D simulation (x-y plane), the definition of z-direction is in *mesh* line. The gradient of mesh is supported by the tuning parameter *r*. The mesh is defined in a unit of micron.

The material database is very limited, but most of the materials can be customized based on the reference materials, such as Si and GaAs. Once a parameter of the new material is defined (e.g. mobility), the tool will overwrite the corresponding value of the reference material in the user-defined material. In other words, all the parameters of the new material are inherited from the reference material unless specified. In *mater* section, the reference material is defined using "*def* = ". In most cases, a new material should specify energy band gap (*eg300*), relative conduction band position (*ec*), permittivity (*perm*), effective band density of states (*nc300, nv300*), mobility (*mun, mup*), intrinsic lifetime (*taun0, taup0*), and recombination related parameters (*augn, augp, b0dir*). Generation rate should be defined after solving equilibrium condition in *solve* section.

```
$
mater name=GaSb def=gaas
+     eg300=0.8
+     perm=14
+     nc300=2.51e16 nv300=7.59e17
+     mun=100000
+     mup=1000
+     augn=1e-29 augp=1e-28
+     taun0=1e-6 taup0=1e-6
+     b0dir=1e-14
$
```

Figure AIII- 1. An example of material definition of GaSb using GaAs as the reference material.

In *models* section, the recombination, lifetime, tunneling and laser can be assigned as true or false. Statistics and temperature should be specified. In *method* section, the parameters are associated with miscellaneous numerical methods. The number of iterations and the converge condition are defined. The default set should be applicable for most of the simulations.

In *solve* section, *solve init* gives the solution under equilibrium. If the solution of the device under bias is required, additional lines with the specified voltage step size and number of steps are introduced, as well as those with a generation rate. The *plot* syntax right after the *solve*

syntax will generate a set of output ASCII text files under the given solve condition. If one need to export the output files for multiple voltages, a set of *solve* followed by the *plot* syntax is required. The I-V characteristics are recorded in *log* file. The output format of *log* is very hard to interpret in the beginning, and it varies with the transient condition and number of electrodes. The tactics here is to compare each value with the log printed during the simulation, and then one can clarify the electron/hole current for a given electrode under a given bias.

Finally, in *plot* section, plots from 1D to 3D can be specified upon users' need. Band profile (*band.v, band.c*), quasi Fermi level (*qfn, qfp*), concentration (*Electrons, Holes*), and current density (*J.electr, J.hole*) are recommended.

In my opinion, PADRE is a power tool of solving the classical heterostructure problems if the quantum effect is not involved. By using a coupled set of partial differential equations, the calculated band profile, concentration and current in a PN diode agree with the ones calculated by the equations in Physics of Semiconductor Devices book, which makes it a convincing simulation tool. To my best knowledge, only Linux version of PADRE supports heterostructure simulation. The online nanoHUB version supports the graphical view of the simulation results, and it also provides several examples of input files for users to start from.

References

1. A. M. White, *Infra red detectors* (Google Patents, 1987).

2. P. Klipstein, *Depletion-less photodiode with suppressed dark current and method for producing the same* (Google Patents, 2010).

3. S. Maimon and G. W. Wicks, Applied Physics Letters **89**, 151109 (2006).

4. P. Klipstein, “"XB n " barrier photodetectors for high sensitivity and high operating temperature infrared sensors,” in *Infrared Technology and Applications XXXIV*, edited by B. F. Andresen, G. F. Fulop, and P. R. Norton (SPIE, 2008), 69402U.

5. D. Donetsky, J. Liu, G. Kipshidze, L. Shterengas, G. Belenky, W. L. Sarney, and S. P. Svensson, Appl. Phys. Lett. **115**, 81102 (2019).

6. Y. Lin, D. Donetsky, D. Wang, D. Westerfeld, G. Kipshidze, L. Shterengas, W. L. Sarney, S. P. Svensson, and G. Belenky, J. Electron. Mater. **44**, 3360 (2015).

7. D. Wang, Y. Lin, D. Donetsky, G. Kipshidze, L. Shterengas, G. Belenky, S. P. Svensson, W. L. Sarney, H. Hier, Proc SPIE **8704**, 870410 (2013).

8. D. Donetsky, S. P. Svensson, L. E. Vorobjev, and G. Belenky, Appl. Phys. Lett. **95**, 212104 (2009).

9. M. Walther, J. Schmitz, R. Rehm, S. Kopta, F. Fuchs, J. Fleißner, W. Cabanski, and J. Ziegler, Journal of Crystal growth **278**, 156 (2005).

10. A. Rogalski, P. Martyniuk, and M. Kopytko, Applied physics reviews **4**, 31304 (2017).

11. P. C. Klipstein, Y. Livneh, A. Glozman, S. Grossman, O. Klin, N. Snapi, and E. Weiss, Journal of electronic materials **43**, 2984 (2014).

12. Y. Aytac, B. V. Olson, J. K. Kim, E. A. Shaner, S. D. Hawkins, J. F. Klem, M. E. Flatté, and T. F. Boggess, J. Appl. Phys. **118**, 125701 (2015).

13. Y. Aytac, B. V. Olson, J. K. Kim, E. A. Shaner, S. D. Hawkins, J. F. Klem, J. Olesberg, M. E. Flatté, and T. F. Boggess, J. Appl. Phys. **119**, 215705 (2016).

14. P. T. Webster, N. A. Riordan, S. Liu, E. H. Steenbergen, R. A. Synowicki, Y.-H. Zhang, and S. R. Johnson, Appl. Phys. Lett. **106**, 61907 (2015).

15. D. H. Wu, A. Dehzangi, Y. Y. Zhang, and M. Razeghi, Appl. Phys. Lett. **112**, 241103 (2018).

16. D. Z. Ting, A. Soibel, A. Khoshakhlagh, S. A. Keo, B. Rafol, L. Höglund, E. M. Luong, A. M. Fisher, C. J. Hill, and S. D. Gunapala, J. Electron. Mater. **48**, 6145 (2019).

17. I. Vurgaftman, J. R. Meyer, and L. R. Ram-Mohan, J. Appl. Phys. **89**, 5815 (2001).

18. P. Martyniuk, M. Kopytko, and A. Rogalski, Opto-Electronics Review **22**, 127 (2014).

19. W. E. Tennant, D. Lee, M. Zandian, E. Piquette, and M. Carmody, J. Electron. Mater. **37**, 1406 (2008).

20. W. E. Tennant, J. Electron. Mater. **39**, 1030 (2010).

21. L. K. Casias, C. P. Morath, E. H. Steenbergen, G. A. Umana-Membreno, P. T. Webster, J. V. Logan, J. K. Kim, G. Balakrishnan, L. Faraone, and S. Krishna, Appl. Phys. Lett. **116**, 182109 (2020).

22. B. V. Olson, J. F. Klem, E. A. Kadlec, J. K. Kim, M. D. Goldflam, S. D. Hawkins, A. Tauke-Pedretti, W. T. Coon, T. R. Fortune, E. A. Shaner, and M. E. Flatté, Phys. Rev. Appl. **7**, 24016 (2017).

23. C.-Y. Tsai, Y. Zhang, Z. Ju, and Y.-H. Zhang, Appl. Phys. Lett. **116**, 201108 (2020).

24. J. A. Nolde, E. M. Jackson, M. V. Warren, C. L. Canedy, S. Tomasulo, M. F. Bennett, M. Kim, E. R. Cleveland, C. S. Kim, C. A. Affouda, C. T. Ellis, I. Vurgaftman, J. R. Meyer, and E. H. Aifer, IEEE J. Quantum Electron. **55**, 1 (2019).

25. G. Belenky, D. Donetsky, G. Kipshidze, D. Wang, L. Shterengas, W. L. Sarney, and S. P. Svensson, Appl. Phys. Lett. **99**, 141116 (2011).

26. Y. Lin, D. Wang, D. Donetsky, L. Shterengas, G. Kipshidze, G. Belenky, S. P. Svensson, W. L. Sarney, and H. S. Hier, J. Electron. Mater. **42**, 918 (2013).

27. A. Rogalski, Progress in Quantum Electronics **27**, 59 (2003).

28. *InSb electron mobility*, <http://www.ioffe.ru/SVA/NSM/Semicond/InSb/bandstr.html#Basic>.

29. *Nextnano-software for semiconductor nanodevices*, <https://www.nextnano.de/customer/tutorials.php>.

30. D. Z. Ting, A. Khoshakhlagh, A. Soibel, and S. D. Gunapala, J. Electron. Mater. **49**, 6936 (2020).

31. Z.-Y. Lin, S. Liu, E. H. Steenbergen, and Y.-H. Zhang, Appl. Phys. Lett. **107**, 201107 (2015).

32. T. D. Nguyen, J. O. Kim, Y. H. Kim, E. T. Kim, Q. L. Nguyen, and S. J. Lee, AIP Advances **8**, 25015 (2018).

33. A. Haddadi, A. Dehzangi, R. Chevallier, S. Adhikary, and M. Razeghi, Scientific reports **7**, 1 (2017).

34. B. M. Nguyen, M. Razeghi, V. Nathan, and G. J. Brown, “Type-II M structure photodiodes: an alternative material design for mid-wave to long wavelength infrared regimes,” in *Quantum Sensing and Nanophotonic Devices IV* (2007), Vol. 6479, 64790S.

35. O. Salihoglu, A. Muti, K. Kutluer, T. Tansel, R. Turan, Y. Ergun, and A. Aydinli, Applied Physics Letters **101**, 73505 (2012).

36. E. H. Aifer, J. G. Tischler, J. H. Warner, I. Vurgaftman, W. W. Bewley, Meyer, JR, J. C. Kim, L. J. Whitman, C. L. Canedy, and E. M. Jackson, Applied Physics Letters **89**, 53519 (2006).

37. J. Liu, D. Donetsky, H. Jiang, G. Kipshidze, L. Shterengas, G. Belenky, W. L. Sarney, and S. P. Svensson, J. Appl. Phys. **128**, 83101 (2020).

38. I. Shtrichman, D. Aronov, M. ben Ezra, I. Barkai, E. Berkowicz, M. Brumer, R. Fraenkel, A. Glozman, S. Grossman, E. Jacobsohn, O. Klin, P. Klipstein, I. Lukomsky, L. Shkedy, N. Snapi, M. Yassen, and E. Weiss, “High operating temperature epi-InSb and XBn-InAsSb photodetectors,” in *High operating temperature epi-InSb and XBn-InAsSb photodetectors*, edited by B. F. Andresen, G. F. Fulop, and P. R. Norton (SPIE, 2012), 83532Y-83532Y-13.

39. T. Ashley, C. Elliott, N. Gordon, T. Phillips, and R. Hall, Infrared phys. technol. **38**, 145 (1997).

40. C. H. Grein, J. Garland, and M. E. Flatté, J. Electron. Mater. **38**, 1800 (2009).

41. F. Bertazzi, A. Tibaldi, M. Goano, J. A. G. Montoya, and E. Bellotti, Phys. Rev. Applied **14** (2020).

42. D. Z. Ting, A. Soibel, A. Khoshakhlagh, S. A. Keo, S. B. Rafol, A. Fisher, B. J. Pepper, E. M. Luong, C. J. Hill, and S. D. Gunapala, “Antimonide e-SWIR, MWIR, and LWIR barrier infrared detector and focal plane array development,” in *Infrared Technology and Applications XLIV*, edited by G. F. Fulop, C. M. Hanson, P. R. Norton, B. F. Andresen, and J. L. Miller (SPIE, 2018 - 2018), p. 37.

43. A. Haddadi, G. Chen, R. Chevallier, A. M. Hoang, and M. Razeghi, Appl. Phys. Lett. **105**, 121104 (2014).

44. S. P. Svensson, W. A. Beck, W. L. Sarney, D. Donetsky, S. Suchalkin, and G. Belenky, Appl. Phys. Lett. **114**, 122102 (2019).

45. Philip Klipstein, Olga Klin, Steve Grossman, Noam Snapi, Inna Lukomsky, Daniel Aronov, Michael Yassen, Alexander Glozman, Tal Fishman, Eyal Berkowicz, Osnat Magen, Itay Shtrichman, Eliezer Weiss, Opt. Eng **50**, 61002 (2011).

46. Y. Lin, D. Wang, D. Donetsky, G. Kipshidze, L. Shterengas, L. E. Vorobjev, and G. Belenky, Semicond. Sci. Technol. **29**, 112002 (2014).

47. *GaInSb optical property*, <http://www.ioffe.ru/SVA/NSM/Semicond/GaInSb/optic.html>.

48. A. Cheknane and T. Benouaz, J. Semicond. **30**, 72001 (2009).

49. Z. Djuric, B. Livada, V. Jovic, M. Smiljanic, M. Matic, and Z. Lazic, Infrared Phys. **29**, 1-7 (1989).

50. G. Blaj, C. J. Kenney, J. Segal, and G. Haller, Analytical Solutions of Transient Drift-Diffusion in P-N Junction Pixel Sensors (2017).

51. I. Vurgaftman, G. Belenky, Y. Lin, D. Donetsky, L. Shterengas, G. Kipshidze, W. L. Sarney, and S. P. Svensson, Appl. Phys. Lett. **108**, 222101 (2016).

52. A. Rogalski, R. Ciupa, and W. Larkowski, Solid-State Electronics **39**, 1593 (1996).

53. W. C. Mitchel, S. Elhamri, H. J. Haugan, G. J. Brown, S. Mou, and F. Szmulowicz, J. Appl. Phys. **120**, 175701 (2016).

54. F. Szmulowicz, S. Elhamri, H. J. Haugan, G. J. Brown, and W. C. Mitchel, J. Appl. Phys. **105**, 74303 (2009).

55. D. R. Rhiger and E. P. Smith, J. Electron. Mater. **48**, 6053 (2019).

56. D. Z. Ting, A. Soibel, L. Höglund, C. J. Hill, S. A. Keo, A. Fisher, and S. D. Gunapala, J. Electron. Mater. **45**, 4680 (2016).

57. D. Wang, D. Donetsky, G. Kipshidze, Y. Lin, L. Shterengas, G. Belenky, W. Sarney, and S. Svensson, Appl. Phys. Lett. **103**, 51120 (2013).

58. S. Suchalkin, J. Ludwig, G. Belenky, B. Laikhtman, G. Kipshidze, Y. Lin, L. Shterengas, D. Smirnov, S. Luryi, W. L. Sarney, and S. P. Svensson, J. Phys. D: Appl. Phys. **49**, 105101 (2016).

59. J. I. Cisneros, Appl. Opt. **37**, 5262 (1998).

60. G. Bishop, E. Plis, J. B. Rodriguez, Y. D. Sharma, H. S. Kim, L. R. Dawson, and S. Krishna, J. Vac. Sci. Technol. B **26**, 1145 (2008).

61. S. Maimon and G. W. Wicks, Appl. Phys. Lett. **89**, 151109 (2006).

62. J. Midkiff, K. M. Yoo, J.-D. Shin, H. Dalir, M. Teimourpour, and R. T. Chen, Optica **7**, 1544 (2020).

63. I. Thorlabs, *Free-Space Electro-Optic Modulators*, <https://www.thorlabs.com/newgrouppage9.cfm?objectgroup_id=2729>.

64. M. T. Valentine, N. R. Guydosh, B. Gutiérrez-Medina, A. N. Fehr, J. O. Andreasson, and S. M. Block, Opt. Lett. **33**, 599 (2008).

65. C. Wang, M. Zhang, X. Chen, M. Bertrand, A. Shams-Ansari, S. Chandrasekhar, P. Winzer, and M. Lončar, Nature **562**, 101 (2018).

66. *iXblue - Intensity Modulators*, <https://photonics.ixblue.com/store/lithium-niobate-electro-optic-modulator/intensity-modulators>.

67. P. J. Duthie and M. J. Wale, Electron. Lett. **27** (1991).

68. J. Chiles and S. Fathpour, Optica **1**, 350 (2014).

69. *G&H - Pockels Cells*, <https://gandh.com/product-categories/pockels-cells/>.

70. *Eksma Optics - Pockels Cells*, <https://eksmaoptics.com/electro-optics/pockels-cells/>.

71. A. Yariv and P. Yeh, *Photonics*. *Optical electronics in modern communications*, 6th ed. (Oxford University Press, Oxford, 2007).

72. S. L. Chuang, *Physics of photonic devices* (John Wiley & Sons, 2012).

73. D. B. Chenault, R. A. Chipman, and S.-Y. Lu, Applied optics **33** (1994).

74. M. Paturzo, P. De Natale, S. De Nicola, P. Ferraro, S. Mailis, R. W. Eason, G. Coppola, M. Iodice, and M. Gioffré, Opt. Lett. **31**, 3164 (2006).

75. D. Wei, C. Wang, X. Xu, H. Wang, Y. Hu, P. Chen, J. Li, Y. Zhu, C. Xin, X. Hu, Y. Zhang, D. Wu, J. Chu, S. Zhu, and M. Xiao, Nature communications **10**, 4193 (2019).

76. K. C. Burr, C. L. Tang, M A Arbore, M. M. Fejer, Opt. Lett. **22**, 1458 (1997).

77. C. K. N. Patel, Phys. Rev. **136**, 1187 (1964).

78. P. K. Cheo, Appl. Phys. Lett. **23**, 439 (1973).

79. J. E. Kiefer and A. Yariv, Appl. Phys. Lett. **15**, 26 (1969).

80. S. Anders, W. Schrenk, E. Gornik, and G. Strasser, Appl. Phys. Lett. **80**, 1864 (2002).

81. K. Fujita, M. Yamanishi, T. Edamura, A. Sugiyama, and S. Furuta, Appl. Phys. Lett. **97**, 201109 (2010).

82. J. H. McFee, R. E. Nahory, M. A. Pollack, and R. A. Logan, Appl. Phys. Lett. **23**, 571 (1973).

83. B. R. Bennett, R.A. Soref, J. A. Del Alamo, IEEE J. Quant. Electron. **26**, 113 (1990).

84. J. Manning, R. Olshansky, and C. Su, IEEE J. Quant. Electron. **19**, 1525 (1983).

85. C. H. Henry, R. A. Logan, and K. A. Bertness, J. Appl. Phys. **52**, 4457 (1981).

86. C. A. Emeis, L. J. Oosterhoff, Proc. of the Royal Society of London. Series A, Math. and Phys. Sci. **54**, 297 (1967).

87. V. Lucarini, J. J. Saarinen, K. E. Peiponen, *Kramers-Kronig relations in optical materials research* (Springer Science & Business Media, 2005).

88. M. Born and E. Wolf, *Principles of optics: electromagnetic theory of propagation, interference and diffraction of light* (Elsevier, 2013).

89. W. L. Sarney, S. P. Svensson, H. Hier, G. Kipshidze, D. Donetsky, D. Wang, L. Shterengas, and G. Belenky, J. of Vacuum Science & Technology B, Nanotechnology and Microelectronics: Materials, Processing, Measurement, and Phenomena **30**, 02B105 (2012).

90. S. P. Svensson, W. L. Sarney, H. Hier, Y. Lin, D. Wang, D. Donetsky, L. Shterengas, G. Kipshidze, and G. Belenky, Phys. Rev. B **86** (2012).

91. G. Belenky, Y. Lin, G. Kipshidze, S. Suchalkin, L. Shterengas, and D. Donetsky, Electron. Lett. **51**, 1521 (2015).

92. S. P. Svensson, W. L. Sarney, D. Donetsky, G. Kipshidze, Y. Lin, L. Shterengas, Y. Xu, and G. Belenky, Appl. Opt. **56**, B58-B63 (2017).

93. Y. Lin, D. Wang, D. Donetsky, G. Kipshidze, L. Shterengas, G. Belenky, W. L. Sarney, and S. P. Svensson, Int. J. Hi. Spe. Ele. Syst. **23**, 1450021 (2014).

94. B. V. Olson, C. H. Grein, J. K. Kim, E. A. Kadlec, J. F. Klem, S. D. Hawkins, and E. A. Shaner, Appl. Phys. Lett. **107**, 261104 (2015).

95. J. S. Blakemore, *Semiconductor statistics* (Pergamon, Oxford, 1962).

96. R. Dornhaus and G. Nimtz, *The properties and applications of the Hg1-xCdxTe alloy system* (Springer-Verlag, NY, 1976).

97. Y. Li and J. Ibanez-Guzman, IEEE Signal Process. Mag. **37**, 50 (2020).

98. R. L. Olmon, B. Slovick, T. W. Johnson, D. Shelton, S.-H. Oh, G. D. Boreman, and M. B. Raschke, Phys. Rev. B **86** (2012).

99. *Nanophotonic FDTD Simulation Software - Lumerical FDTD*, <https://www.lumerical.com/products/fdtd/>.

100. D. T. Norton, J. T. Olesberg, R. T. McGee, N. A. Waite, J. Dickason, K. W. Goossen, J. Lawler, G. Sullivan, A. Ikhlassi, F. Kiamilev, E. J. Koerperick, L. M. Murray, J. P. Prineas, and T. F. Boggess, IEEE J. Quantum Electron. **49**, 753 (2013).

101. X. Fu, J. Cheng, Q. Huang, Y. Hu, W. Xie, M. Tassaert, J. Verbist, K. Ma, J. Zhang, K. Chen, C. Zhang, Y. Shi, J. Bauwelinck, G. Roelkens, L. Liu, and S. He, Optics express **23**, 18686 (2015).

102. P. Martyniuk, M. Kopytko, and A. Rogalski, Opto-Electronics Review **22**, 127 (2014).

103. *PADRE nanoHUB*, <https://nanohub.org/resources/padre>.

104. B. V. Olson, E. A. Shaner, J. K. Kim, J. F. Klem, S. D. Hawkins, M. E. Flatté, and T. F. Boggess, Appl. Phys. Lett. **103**, 52106 (2013).

105. M. Ren, S. J. Maddox, M. E. Woodson, Y. Chen, S. R. Bank, and J. C. Campbell, Appl. Phys. Lett. **108**, 191108 (2016).

106. B. V. Olson, E. A. Shaner, J. K. Kim, J. F. Klem, S. D. Hawkins, L. M. Murray, J. P. Prineas, M. E. Flatté, and T. F. Boggess, Appl. Phys. Lett. **101**, 92109 (2012).

107. R. J. Ricker, S. R. Provence, D. T. Norton, T. F. Boggess, and J. P. Prineas, J. Appl. Phys. **121**, 185701 (2017).

108. *NSLS-II - Sort Xpray Scattering & Spectroscopy*, <https://www.bnl.gov/nsls2/programs/soft-xray-scattering.php>.

109. J. Liu, K. Kucharczyk, R. Lutchman, D. Donetski, C. Eng, S. Hulbert, C. Mazzoli, and B. Podobedov, eds., *Progress towards soft X-ray beam position monitor development* (MOPAB121, 2021).

110. G. Decker and O. Singh, PRAB **2** (1999).

111. E. Johnson and T. Oversluizen, Rev. Sci. Instrum. **60**, 1947 (1989).

112. D. Shu, B. Rodricks, J. Barraza, T. Sanchez, and T. Kuzay, Nucl. Instrum. Methods Phys. Res. A **319**, 56 (1992).

113. A. M. Barnett, D. J. Bassford, J. E. Lees, J. S. Ng, C. H. Tan, and J.P.R. David, Nuclear Instruments and Methods in Physics Research Section A: Accelerators, Spectrometers, Detectors and Associated Equipment **621**, 453 (2010).

114. A. M. Barnett, J. E. Lees, D. J. Bassford, J. S. Ng, C. H. Tan, N. Babazadeh, and R. B. Gomes, Nuclear Instruments and Methods in Physics Research Section A: Accelerators, Spectrometers, Detectors and Associated Equipment **654**, 336 (2011).

115. G. Lioliou and A. M. Barnett, Nuclear Instruments and Methods in Physics Research Section A: Accelerators, Spectrometers, Detectors and Associated Equipment **836**, 37 (2016).

116. M. C. Veale, S. J. Bell, D. D. Duarte, M. J. French, A. Schneider, P. Seller, M. D. Wilson, A. D. Lozinskaya, V. A. Novikov, O. P. Tolbanov, A. Tyazhev, and A. N. Zarubin, Nuclear Instruments and Methods in Physics Research Section A: Accelerators, Spectrometers, Detectors and Associated Equipment **752**, 6 (2014).

117. D. C. Look, D. C. Walters, G. D. Robinson, J. R. Sizelove, M. G. Mier, and C. E. Stutz, Journal of Applied Physics **74**, 306 (1993).

118. I. S. Gregory, C. Baker, W. R. Tribe, M. J. Evans, H. E. Beere, E. H. Linfield, A. G. Davies, and M. Missous, Appl. Phys. Lett. **83**, 4199 (2003).

119. D. E. Bliss, W. Walukiewicz, J. W. Ager, E. E. Haller, K. T. Chan, and S. Tanigawa, Journal of Applied Physics **71**, 1699 (1992).

120. L. Jastrzebski, J. Lagowski, and H. C. Gatos, Appl. Phys. Lett. **27**, 537 (1975).

121. P. Forck, P. Kowina, and D. Liakin.

122. R. A. Caruana, R. B. Searle, T. Heller, and S. I. Shupack, Analytical chemistry **58**, 1162 (1986).

123. H. Guo, IEEE Signal Process. Mag. **28**, 134 (2011).

124. I. Al-Nahhal, O. A. Dobre, E. Basar, C. Moloney, and S. Ikki, IEEE Signal Process. Mag. **36**, 157 (2019).

125. S. C. Leemann, S. Liu, A. Hexemer, M. A. Marcus, C. N. Melton, H. Nishimura, and C. Sun, Physical review letters **123**, 194801 (2019).

126. T. Tanaka and H. Kitamura, J. Synchrotron Radiat. **8**, 1221 (2001).

127. *SRW by sirepo - cloud-based workspace for synchrotron radiation simulation*, <https://www.sirepo.com/en/landing.html>.

128. *X-ray interactions with matter*, <https://henke.lbl.gov/optical_constants/>.

129. *Chapter 7 - The Diffusion Equation*, <https://www.uni-muenster.de/imperia/md/content/physik_tp/lectures/ws2016-2017/num_methods_i/heat.pdf>.

130. D. Vasileska and G. Klimeck, *Tutorial for PADRE-Based Simulation Modules*, <https://nanohub.org/resources/7224/download/Tutorial_PADRE_Simulation_Tools.pdf>.

131. *PADRE Simulator*, <https://nanohub.org/resources/1581/download/intro_dd_padre_word.pdf>.

132. *Padre 2.4E Users Manual*, <https://nanohub.org/resources/3943/download/padre_manual.pdf>.

133. *PADRE Command Library - TCAD stanford*, <http://www-tcad.stanford.edu/local/DOC/PADRE/padre-ref/intro.html>.